MECHANICAL BEHAVIOR OF CERAMIC COMPOSITE HOT-GAS FILTERS AFTER EXPOSURE TO SEVERE ENVIRONMENTS

D. J. Pysher, B. L. Weaver, R. G. Smith, J. H. Eaton, and J. L. Kahnke

Ceramic Technology Center
3M Company
St. Paul, MN 55144-1000

ABSTRACT

A novel type of hot-gas filter based on a ceramic fiber reinforced ceramic matrix has been developed, as reported at previous Fossil Energy Materials Conferences, through research activities at Oak Ridge National Laboratory (ORNL) and at the 3M Company. Simulated testing has been done at the Westinghouse Science and Technology Center. This filter technology has been extended to full size, 60 mm OD by 1.5 meter long candle filters and a commercially viable process for producing the filters has been developed. Filters are undergoing testing and demonstration use throughout the world for applications in pressurized fluidized-bed combustion (PFBC) and integrated gasification combined cycle (IGCC) plants. Demonstration tests of this ceramic composite filter along with other filters are in progress at the Tidd PFBC plant.

Mechanical tests were performed on the 3M brand Ceramic Composite Candle Filter after exposure to various corrosive environments in order to assess its ability to function as a hot gas filter in coal-fired applications. Due to the different construction of ceramic composite filters and the thin composite wall versus the typical thick-walled monolithic filter, standard mechanical property tests had to be refined or modified to accurately determine the filter's properties. These tests and filter property results will be described.

Longitudinal tensile and diametral O-ring compression tests were performed on as-produced candle filters as well as on filters which had been exposed to various environments. The exposures were for 1000 hrs at 850°C in wet air, in wet air containing Na_2CO_3, and in wet air containing NaCl. In addition, a filter which had been coated with ash (Old Grimethorpe) was exposed to wet air at 850°C for 1000 hours.

INTRODUCTION

A novel type of hot-gas filter based on a ceramic fiber reinforced ceramic matrix has been developed through research activities at Oak Ridge National Laboratory (ORNL) and at the 3M Company under a contract with the U.S. DOE Office of Fossil Energy's Advanced Research and Technology Development (AR & TD) Materials Program. This filter development has been extended from a laboratory sample stage to the fabrication of full size, 60 mm OD by 1.5 meter long candle filters with a commercially viable process for producing the filters.[1,2]

As reported at previous Fossil Energy Materials Conferences, simulated pressurized fluidized-bed combustion (PFBC) testing of two sets of the ceramic composite filters has been completed at the Westinghouse Science and Technology Center.[3,4] Filters are currently undergoing testing and

demonstration use in various university test laboratories and industrial facilities throughout the world for applications in pressurized fluidized-bed combustion (PFBC) and integrated gasification combined cycle (IGCC) plants.

Demonstration tests of the 3M Ceramic Composite Candle Filters along with other filters are in progress at the Tidd PFBC plant under the sponsorship of Morgantown Energy Technology Center (METC), American Electric Power (AEP), and Westinghouse (WSTC). One 3M filter removed during 4th Quarter 1994 from the Tidd Power Plant test has been divided between 3M and Westinghouse for analysis. An additional ten filters were installed and tested during the 1st Quarter of 1995. These ten filters are waiting to be removed from the system for analysis. At this point the details of the Tidd test cannot be discussed until METC, AEP, and Westinghouse release the test information.

Traditional (monolithic) mechanical property tests which utilize bend bars or tensile coupons cannot be adapted to tubular, low-density composite geometries without undue complications. Therefore, test methodologies were developed which subject candle filters to conditions they are expected to experience in service in order to assess their ability to function as a hot gas filter in coal-fired PFBC and IGCC applications. Sections of composite were tested in longitudinal tension and in diametral compression in both the as-produced state as well as after exposure to oxidative/corrosive environments which simulated those encountered in service. The results of the mechanical property testing of the 3M Ceramic Composite Candle Filter used at Tidd are presented along with retained baseline samples and samples exposed to various corrosive environments in the laboratory.

EXPERIMENTAL PROCEDURE

A 60" candle filter was sectioned as shown in Figure 1. Tensile, O-ring diametral compression, and filtration tests were performed on both exposed and unexposed portions to allow comparisons to be made.

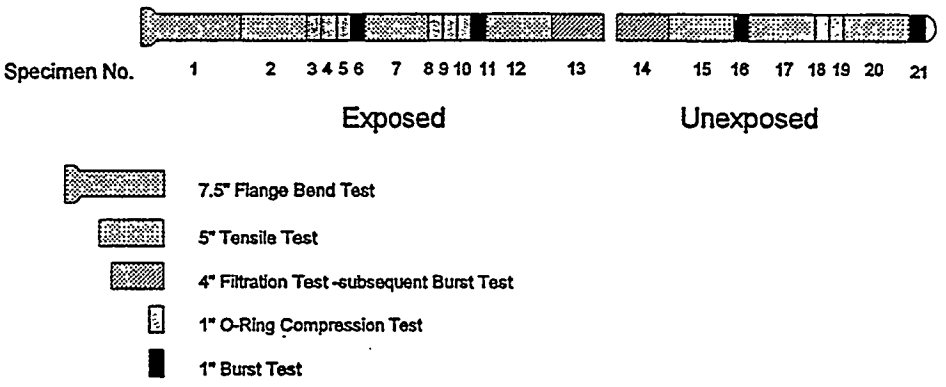

Figure 1. Sectioning of 60" candle filter.

For oxidation experiments, 36" of the flange end of an as-fabricated candle filter was placed into a preheated tube furnace. The rate of air flow through a bubbler containing water into the furnace was 1 l/min. Exposures were performed at 850°C for 1000 hours. Weights of the entire section were recorded before and after exposure and each test specimen was weighed after exposure as well. For corrosion/oxidation experiments, the candle filters were dipped in a solution of either Na_2CO_3 or NaCl prior to oxidation. The solutions were prepared so as to give a uniform concentration of about $1x10^{17}$ Na ions/cm^2.[5]

Filtration testing was performed using a commercial filter tester.[a] The filtration test utilized NaCl particles with a mean diameter of 0.1 μ at a concentration of 100 mg/m3. The filtration test was performed at a given flow rate of 30 liters/min, corresponding to a face velocity of 3.0 cm/sec for a 4" filter tube section. Face velocity equals flow rate divided by surface area. Efficiency is calculated by dividing the concentration of particles exiting the filter by the input concentration.

Maximum pore diameter and permeability were determined by standard methods[6]. The maximum pore diameter was determined by submerging the filter in a liquid medium (water) and measuring the pressure at which bubbling first occurs. Permeability was determined by measuring the pressure drop across the filter at various air flow rates.

Tensile specimens were fabricated by epoxying standard iron pipe reducer fittings into the ends of a 5" section of tube using epoxy[b]. Fixtures were then screwed into the fittings and attached to the test frame and load cell using orthogonally-oriented pins to minimize non-axial loading. A crosshead speed of 2.0 mm/min was used.

Although it does not directly simulate stresses encountered in service, the O-ring compression test is a simple and effective test for monitoring process variables or service conditions which affect composite failure behavior. Tests were performed by diametrically compressing a 1" section of filter tube. A crosshead speed of 4.0 mm/min was used and tests were halted after a crosshead displacement of 5 mm.

RESULTS & DISCUSSION

Filter sections subjected to the wet oxidation and the Na_2CO_3/NaCl dip + oxidation treatments developed a uniform golden hue and experienced a minimal weight gain, consistent with passive oxidation of the SiC matrix.

a TSI Automated Filter Tester, model 8110.

b 3M Scotch-Weld™ 1838-L B/A

Filtration Test Results

Filtration results for filter samples subjected to wet oxidation are presented in Figure 2. Results for samples coated with ash prior to oxidation are presented in Figure 3. For both exposures, filtration efficiency reached 99.9% within 10 minutes of the test, which is typical of the 3M filter. Pressure drop for the wet oxidized sample was slightly lower after exposure. The filtration results for samples coated with Na_2CO_3 and NaCl fall between these two extremes.

Mechanical Test Results

The tensile strengths were calculated using

$$\sigma_{tensile} = \frac{F}{\pi(r_o^2 - r_i^2)} \qquad (1)$$

where F is the fracture load (in Newtons), and r_0 and r_i are the outer and inner tube radii, respectively. Tensile stiffness values were determined from the maximum slope of the load-displacement curves.

For stress analyses, the composite filter is treated as a thin-wall cylinder (i.e. the assumption of constant stress across the wall results in negligible error) since its internal diameter-to-thickness ratio is greater than 10 (≈ 30)[7]. The equation used to calculate the maximum stress in an O-ring is that for a thin-walled cylinder and is given by[8]

$$\sigma_{O-Ring} = \frac{2Fr_a}{\pi dt^2}\frac{(6r_a - t)}{(2r_a - t)} \qquad (2)$$

where r_a is the average radius ($r_a = [r_0 + r_i] / 2$), t is the wall thickness, and d is the specimen width.

A critical parameter in determining accurate stresses is a wall thickness (see Equation 1 and 2 above), which describes the true cross-sectional area. For the 3M Ceramic Composite Candle Filter, the thin-walled, high-porosity construction makes it difficult to decide on a representative wall thickness. Work has begun on determining an "effective" wall thickness from the true density (based on submerged weight measurements). This effective wall thickness would be the thickness of a 100% dense tube having the same average radius and length.

Mechanical testing at this point has focused on the substrate layer of the 3M Ceramic Composite Candle Filter as this is the principal load supporting layer of the filter. The other layers are not intended

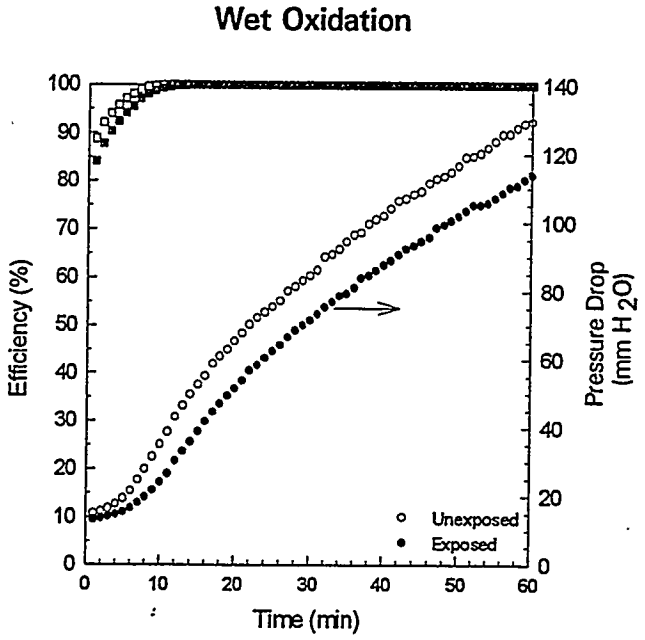

Figure 2. Filtration efficiency and pressure drop for ceramic composite candle filter oxidized at 850° C for 1000 hours.

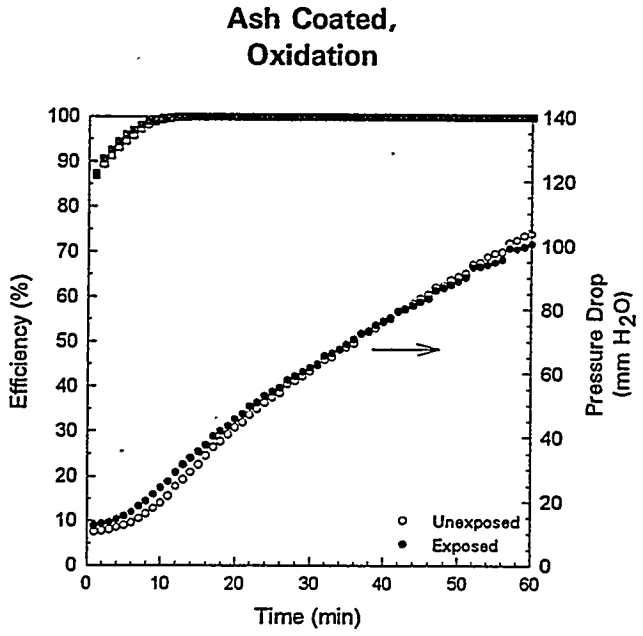

Figure 3. Filtration efficiency and pressure drop for ceramic composite candle filter coated with ash and oxidized at 850° C for 1000 hours.

to be structural, but may or may not contribute to the overall strength of the filter. Work has begun on determining what affect, if any, these outer layers have on mechanical properties.

OBSERVATIONS

A summary of the mechanical test results is given in Table 1. In the laboratory exposure tests the samples retained approximately 50% of the as-produced peak tensile stress. The Tidd PFBC exposed sample retained 69% of the as-produced peak tensile stress. Representative tensile load-displacement curves are shown in Figure 4.

Table 1. Results from tensile and O-ring compression tests of as-produced and exposed filters.

		Oxidized	Na_2CO_3 dipped, oxidized	NaCl dipped, oxidized	Ash coated, oxidized	Tidd PFBC
Peak Tensile Stress (MPa)	As-Produced	50	51	47	46	(48)
	After Exposure	27	24	28	23	34
	Retained	**54%**	**46%**	**59%**	**50%**	**69%**
Tensile Stiffness (Kg/mm)	As-Produced	2236	2426	2552	2501	(2446)
	After Exposure	2099	2236	2353	1793	2158
	Retained	**94%**	**92%**	**92%**	**72%**	**88%**
Peak O-Ring Stress (MPa)	As-Produced	10.8	9.8	7.8	6.1	(8.7)
	After Exposure	6.8	5.0	4.6	4.8	9.3
	Retained	**63%**	**51%**	**59%**	**79%**	**107%**
O-Ring Stiffness (Kg/mm)	As-Produced	12.7	11.2	8.2	10.4	(10.6)
	After Exposure	5.3	4.4	5.1	4.2	11.5
	Retained	**42%**	**39%**	**62%**	**40%**	**109%**

Numbers in parentheses are retained baseline samples.

The laboratory exposure O-ring test specimens retained slightly more than 50% of the as-produced stress values. Again, the Tidd PFBC exposed samples retained more of the as-produced stress than the laboratory exposed samples. Representative O-ring load-displacement curves are shown in Figure 5.

The values for percent of retained tensile stiffness do not indicate a clear trend. The O-ring stiffness retention does indicate that there was very little effect on this value in the Tidd PFBC exposure test.

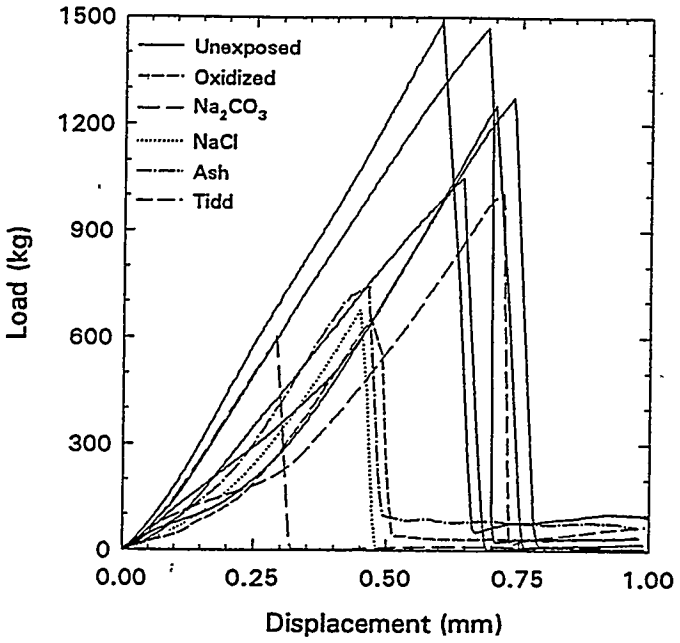

Figure 4. Load-displacement curves from tensile tests on unexposed and exposed filters.

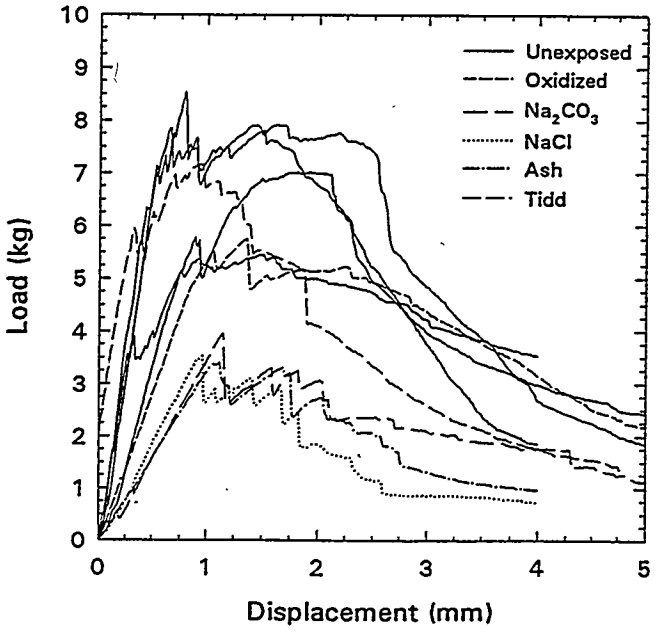

Figure 5. Load-displacement curves from O-ring tests on unexposed and exposed filters.

The similarity in stress retention between the oxidized samples, and the Na_2CO_3, NaCl, and ash coated samples, seems to indicate a similar mechanism at work in these samples. All of these samples were exposed to wet air at high temperatures, this indicates that oxidation is the primary factor in the reduction of strength in these samples. From 3M studies on other ceramic composite parts the initial strength decrease which occurs in the first hours of oxidation exposure is felt to be due to oxidation of the interface materials.

The Tidd PFBC exposed samples did not degrade as much as the laboratory exposed samples. This indicates that the conditions in the PFBC exposure are not as harsh as the conditions used in these laboratory exposures.

FUTURE PLANS

Future testing plans include both exposure and analysis of laboratory samples, and placement and analysis of filters in real industrial environments. Specific plans include the following:

1. A mechanical burst test has been developed as part of the set of composite filter mechanical property tests. Several one inch wide sections have been retained from each of the exposed and baseline filter samples for burst testing in the immediate future.

2. Additional shorter and longer duration laboratory exposure tests will be run to better understand mechanical and filtration durability.

3. A range of exposure specimens will be examined microscopically to determine microstructure changes that correspond to decrease of mechanical properties.

4. Interactions will continue with various outside laboratories and industrial groups to place and test filters in additional real environment PFBC and IGCC applications.

ACKNOWLEDGMENTS

This research was sponsored by U. S. Department of Energy, Office of Fossil Energy, Martin Marietta Energy Systems, Inc., Oak Ridge National Laboratory, and 3M Company. The assistance of D. P. Stinton and R. R. Judkins of Oak Ridge National Laboratory, and T. E. Lippert, M. A. Alvin, E. E. Smeltzer, all of Westinghouse is gratefully acknowledged.

REFERENCES

1. R.G. Smith and J.H. Eaton, "Fabrication of Commercial-Scale Fiber-Reinforced Hot Gas Filters by Chemical Vapor Deposition," Final Technical Report on subcontract No. 93X-SB482C with Martin Marietta Energy Systems, Inc. April, 1994.

2. R.G. Smith and J.H. Eaton, "Fabrication of Commercial-Scale Fiber-Reinforced Hot Gas Filters by Chemical Vapor Deposition," Addendum to Final Technical Report on subcontract No. 93X-SB482C with Martin Marietta Energy Systems, Inc. September, 1994.

3. J.P. Oberst and E.E. Smeltzer, "3M CVI Hot Gas Candle Filter Test Program," Test under General Order No. MP-12775-CE for 3M Company, May 20, 1993.

4. E.E. Smeltzer, "3M CVI Hot Gas Candle Filter Test Program," Test under General Order No. MP-12775-CE for 3M Company, Jan. 27, 1994.

5. Z. Zheng, R.E. Tressler, and K.E. Spear, Fundamental Studies of Corrosion of Nonoxide Structural Ceramics, Vol. 1, Single Crystal Silicon Carbide, Center for Advanced Materials, The Pennsylvania State University, October 1988.

6. ASTM E128-94, "Standard Test Method for Maximum Pore Diameter and Permeability of Rigid Porous Filters for Laboratory Use", 1994 Annual Book of ASTM Standards, vol.14.02, pp. 53-55.

7. p. 5-49 in Marks Standard Handbook for Mechanical Engineers, 9th edition.

8. G. DeWith, "Note on the Use of the Diametral Compression Test for the Strength Measurement of Ceramics," J. Mater. Sci. Lett., 3 [11] 1000-1002 (1984).

FRACTURE BEHAVIOR OF ADVANCED CERAMIC HOT-GAS FILTERS

J.P. Singh, D. Singh, J. Smith, and H. Volz

Energy Technology Division
Argonne National Laboratory
Argonne, IL 60439

ABSTRACT

Microstructural, mechanical, and thermal-shock behavior of hot-gas candle filters obtained from different manufacturers have been evaluated. These filters include both monolithic ceramic and composite materials. Based on the results obtained so far, composite filters perform better than monolithic ceramic filters in a thermal-shock environment. During thermal-shock testing, the monolithic ceramic filters failed in a brittle (catastrophic) mode, while composite filters showed a non-catastrophic mode of failure and very little degradation in ultimate strength. Fractographic evaluations were performed to identify and characterize critical flaws in Nextel fibers for the determination of in-situ fiber strength in Nextel/SiC filters. Average in-situ fiber strength was determined to be 1.7 GPa.

INTRODUCTION

Hot dirty gas exiting from a gasifier or an advanced combustor contains sufficient particulates to warrant it undesirable for direct utilization in gas turbines and heat engines. Today's hot dirty gas cleanup systems, such as cyclones, can remove only the fraction containing the larger particulates. Smaller particulates can be removed only by cooling and filtering the gas. The resulting enthalpy loss causes a significant decrease in overall system efficiency. Because of the enthalpy loss and decrease in overall efficiency, there is a critical need for cleaning hot dirty gas with little or no cooling. The U.S. Department of Energy and others are currently supporting the

development of ceramic/composite filter technology for combined-cycle power generation with coal gasification. Ceramic filters should essentially remove all of the fines from a hot dirty gas stream and be stable in hot dirty gas environments.

This project supports the development of candle ceramic/composite filters for cleanup of hot dirty gases. Effort has been directed toward developing materials qualification technology in order to ensure satisfactory performance of filters in a hot dirty gas stream. To predict long-term performance of such filters, it is important to understand and evaluate the fracture behavior of filters in service environments. Mechanical properties should be evaluated to establish baseline data. Thermal-shock resistance should be measured to predict filter performance in a service environment.[1] Failure modes must be identified and failure mechanisms must be established.

In this paper, results are presented on the evaluation of strength and thermal-shock resistance for the first set of filters obtained from 3M, Du Pont Lanxide, and Industrial Filter and Pump (IFP).

SPECIMENS FOR FRACTURE STUDIES

Initial effort concentrated on filters obtained from the three industrial sources: Nextel/SiC composite filters from 3M, PRD-66 filters from Du Pont Lanxide, and monolithic SiC filters from IFP. The 3M filters consist of layered composite structures, with a tubular filter element sandwiched between two Nextel/SiC composite tubes. Bonding between the Nextel/SiC composite tubes and the filter layer is achieved by chemical vapor infiltration (CVI) of SiC. The inner and outer diameters of these filters are ≈2.54 and ≈2.86 cm, respectively. The PRD-66 is an all–oxide ceramic consisting of a layered microstructure of alumina, mullite, cordierite, and some amorphous material. Inner and outer diameters of the filters are ≈2.26 and ≈2.98 cm, respectively. The monolithic SiC filters consist primarily of SiC grains; inner and outer diameters are ≈2.05 and ≈2.96 cm, respectively.

EVALUATION OF STRENGTH AND THERMAL–SHOCK RESISTANCE

Strength of the candle filters was evaluated on 1–in.–long O-ring specimens machined from each of the three filters. These specimens were loaded to failure in a

diametrical compression mode at a crosshead speed of 0.13 cm/min. Maximum stress is at the inner diameter across the load points, which simulates the thermal-shock stresses developed during pulse-cleaning cycles. The fracture stress, σ_f, is given by the following equation:[2]

$$\sigma_f = PK/\pi bl, \quad (1)$$

where P is the fracture load, K is a function of the ratio of inner and outer diameters,[2] and l is the length of the ring. As shown in Fig. 1, load-deflection plots for the filter specimens in as-fabricated condition indicated a nonbrittle mode of failure for the Nextel/SiC composites and PRD-66 filters, while the IFP monolithic SiC filters showed brittle failure.

Thermal-shock testing of these filters was performed on 1-in.-long ring specimens machined from the filters and insulated on the outer surfaces to simulate heat transfer conditions in service. The specimens were heated to preselected temperatures (25-1100°C) in an electric furnace, as shown in Fig. 2. Subsequently, they were quenched in silicone oil at room temperature (≈25°C). Thermal-shock damage was estimated by measuring the strength of each ring specimen before and after thermal quenching.

Results of the thermal-shock experiments are given in Fig. 3, which shows the retained strength of specimens when subjected to varying degrees of thermal quenching (ΔT). Vertical bars represent standard deviation when three to four specimens were tested. Other data points represent values for single specimens.

Limited results obtained so far indicate that the 3M Nextel/SiC composite filters and Du Pont Lanxide PRD-66 filters show little or no strength degradation when quenched from temperatures up to ≈1000°C. On the other hand, the monolithic SiC filters from IFP showed strength degradation when quenched from temperatures >800°C. Further experiments are currently in progress to confirm the statistical reliability of these results. Microstructural evaluations are also underway to evaluate failure modes and mechanisms for improved prediction of filter performance.

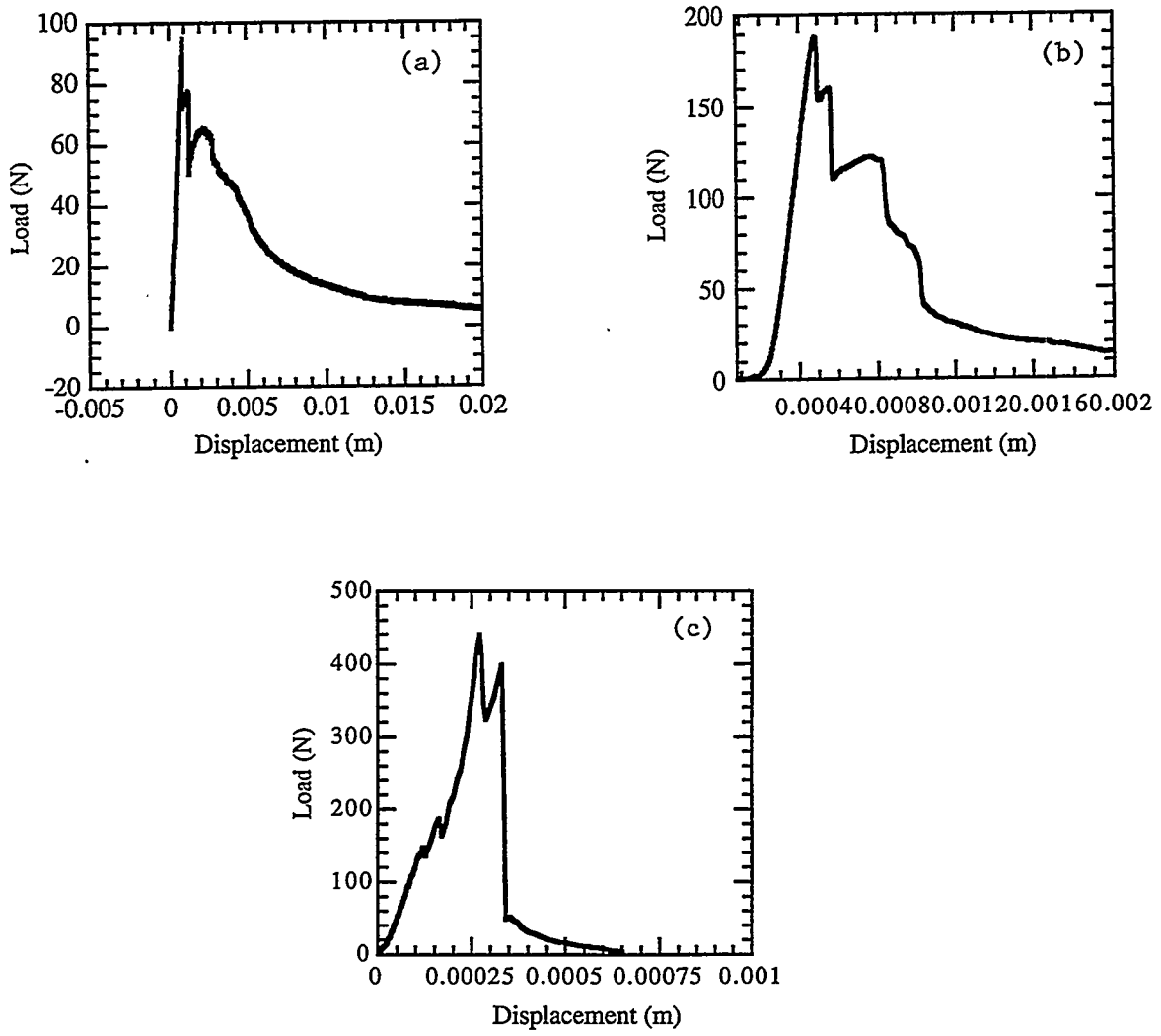

Fig. 1. Load-displacement plots for (a) Nextel/SiC, (b) PRD-66, and (c) IFP SiC filters, showing nonbrittle and brittle fractures.

As noted in other studies,[3,4] a substantial degradation of in-situ strength of Nicalon fibers in Nicalon-fiber-reinforced SiC matrix composites was observed during composite processing and in elevated-temperature service environments. Therefore, a study has been initiated to evaluate the nature of flaw generation and resulting strength degradation of Nextel fibers in the Nextel/SiC composite filters during filter processing and in service. Strength of in-situ Nextel fibers in the Nextel/SiC composites after filter processing has been determined by evaluating critical flaw sizes using fractographic techniques, as described below.

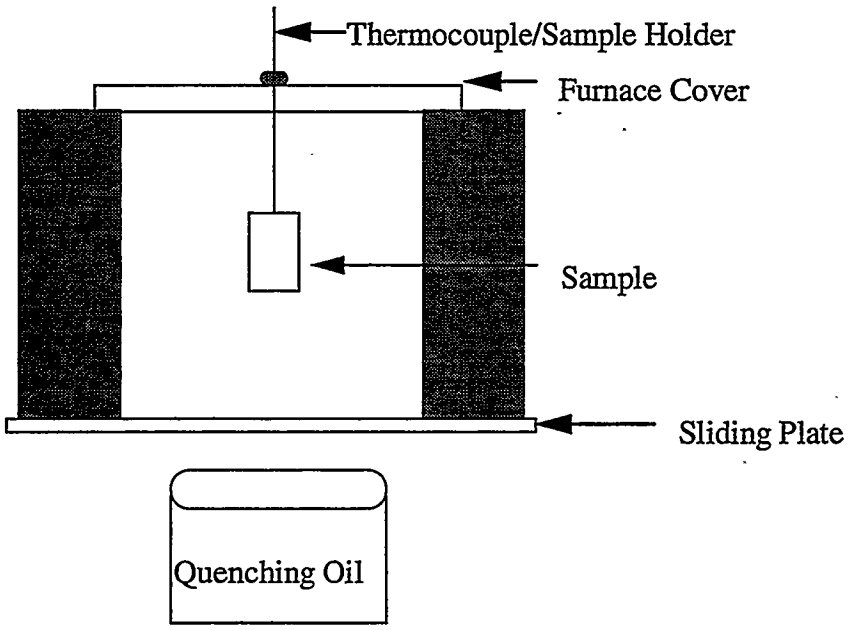

Fig. 2. Schematic diagram of thermal–quench test apparatus.

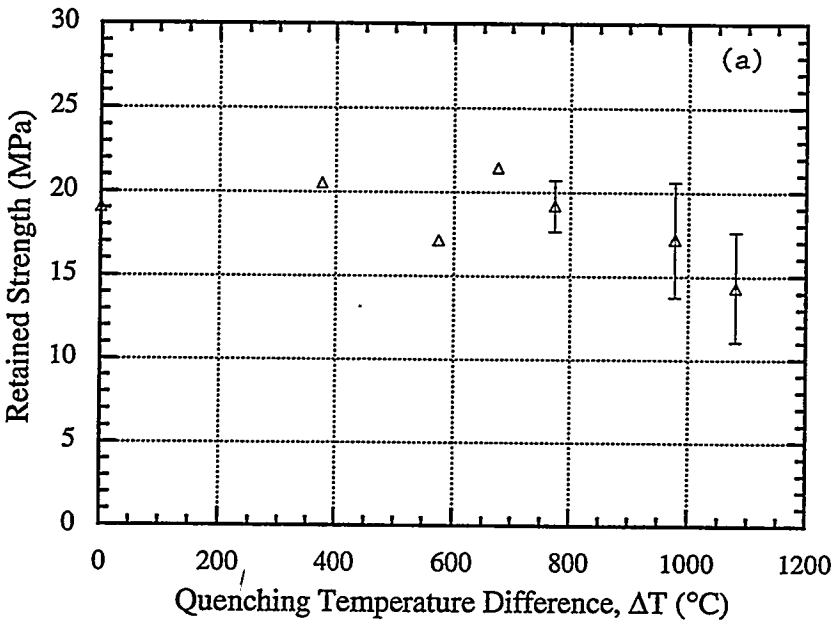

Fig. 3. Dependence of retained strength of ring specimens on quenching temperature difference (ΔT): (a) Nextel/SiC composite filters, (b) PRD-66 filters, and (c) monolithic IFP SiC filters.

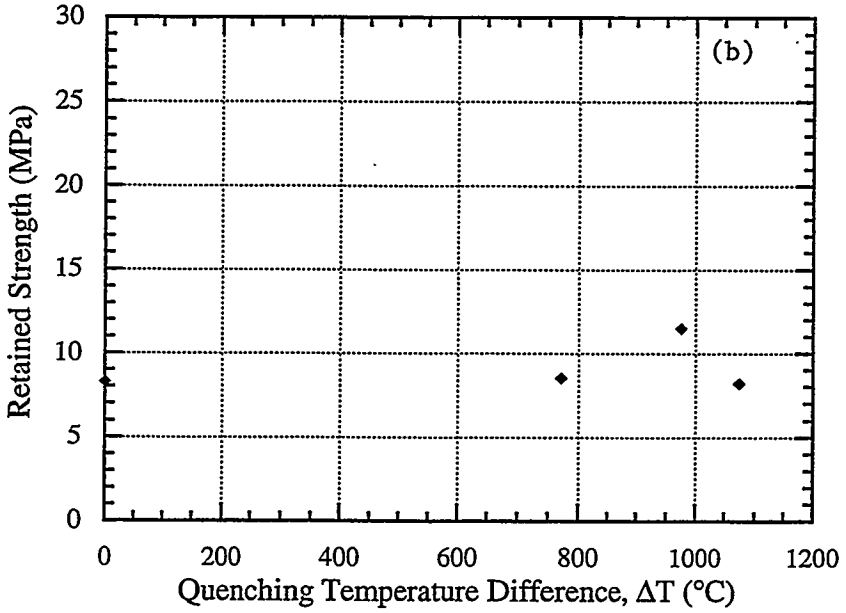
(b)
Retained Strength (MPa)
0
5
10
15
20
25
30
0
200
400
600
800
1000
1200
Quenching Temperature Difference, ΔT (°C)

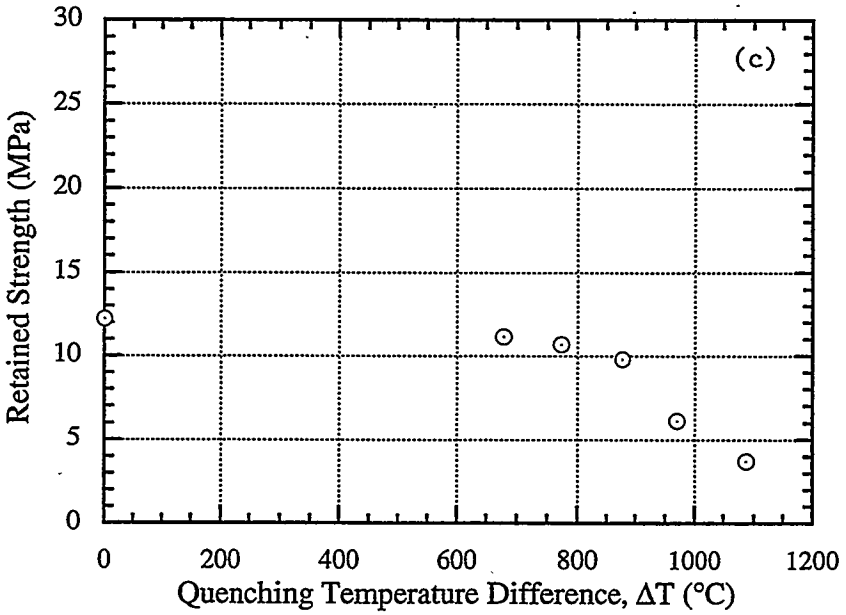
(c)
Retained Strength (MPa)
0
5
10
15
20
25
30
0
200
400
600
800
1000
1200
Quenching Temperature Difference, ΔT (°C)

Fig. 3. (Contd.)

IN–SITU FIBER STRENGTH BEHAVIOR

In-situ strength of fibers in the Nextel/SiC composite filters tested at room temperature was evaluated from characteristic fracture features of the fibers. Strength of fractured fibers was determined from the measured values of fracture mirror radii, as discussed in regard to use of the empirical relationship proposed by Kirchner and Gruver[5] and as given in

$$\sigma_f \sqrt{r_m} = A_m, \tag{2}$$

where σ_f is the fiber fracture strength, r_m is the measured fiber mirror radius, and A_m is the mirror constant and is taken to be 3.5 MPa$\sqrt{m}$.

The measured values of in-situ fiber strengths were described by the Weibull strength distribution function, as shown in

$$F(\sigma) = 1 - \exp\left[-\left(\frac{\sigma}{\sigma_o}\right)^m\right], \tag{3}$$

where $F(\sigma)$ is the cumulative failure probability at an applied stress σ, σ_o is the scale parameter signifying a characteristic strength of the distribution, and m is the Weibull modulus that characterizes the flaw distribution in the material.

Figure 4 shows the distribution of in-situ Nextel fibers in Nextel/SiC composite filters. Average fiber strength is approximately 1.7 GPa. An effort was also made to evaluate the strength of as-fabricated fibers by fiber bundle testing.[6] Average strength of as–fabricated Nextel fibers, obtained from preliminary fiber bundle tests, was 2.1 GPa. This suggests that there is an approximately 20% degradation in the strength of as–fabricated Nextel fibers during filter processing. Further experiments are being conducted to validate the results obtained from bundle tests.

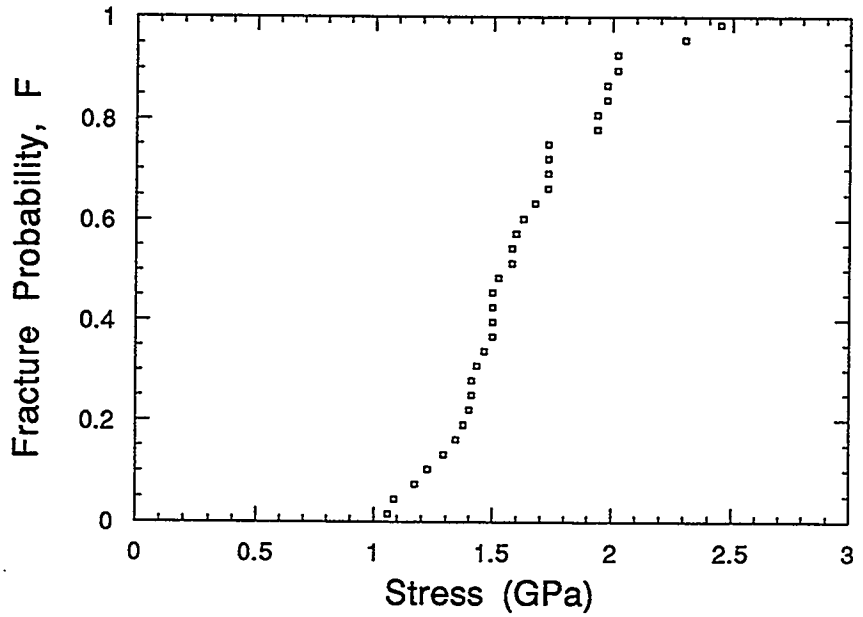

Fig. 4. Weibull strength distribution of Nextel fibers in Nextel/SiC composite filters.

ACKNOWLEDGMENT

The work was supported by the U.S. Department of Energy, Office of Fossil Energy, Advanced Research and Technology Materials Program, under Contract W-31-109-Eng-38. The authors thank D. J. Pysher, B. L. Weaver, and R. G. Smith of the 3M Company, J. A. Chambers of Dupont Lanxide Composites Inc., and P. Eggerstedt and J. Zievers of the Industrial Filter & Pump Manufacturing Company for providing filter specimens and for their helpful discussions.

REFERENCES

1. J. P. Singh, S. Majumdar, A. S. Wagh, T. Wenzel, and R. B. Poeppel, "Materials Qualification Technology for Ceramic Cross-Flow Filters," Argonne National Laboratory Report ANL/FE-91/1, July 1991.

2. E. A. Ripperger and N. Davis, "Critical Stress in Circular Ring," Trans. Amer. Soc. Civ. Engr., Paper No. 2308, pp. 619-35 (1948).

3. J. P. Singh, D. Singh, and R. A. Lowden, "Effect of Fiber Coating on Mechanical Properties of Nicalon Fibers and Nicalon-Fiber/SiC Matrix Composites," Ceram. Eng. Sci. Proc., **15**, [4] 456-464 (1994).

4. D. Singh and J. P. Singh, "Effect of Processing on Strength of Nicalon Fibers in Nicalon Fiber-SiC Matrix Composites," Ceram. Eng. Sci. Proc., **13** [7-8] 257-266 (1992).

5. H. P. Kirchner and R. M. Gruver, "Fracture Mirror in Alumina Ceramics," Phil. Mag. ,**27** 1433–1446 (1973).

6. Z. Chi, T. W. Chou, and G. Shen, "Determination of Single Fiber Strength Distribution from Fiber Bundle Testings," J. Mater. Sci. ,**19** [10], 3319–3324 (1984).

HIGH TEMPERATURE CORROSION OF ADVANCED CERAMIC MATERIALS FOR HOT-GAS FILTERS AND HEAT EXCHANGERS

E. R. Kupp, M. F. Trubelja, K. E. Spear and R. E. Tressler

Materials Science and Engineering
The Pennsylvania State University
University Park, PA 16802

ABSTRACT

Experimental corrosion studies of hot gas filter materials and heat exchanger materials in oxidizing combustion environments have been initiated. Filter materials from 3M Co. and DuPont Lanxide Composites Inc. are being tested over a range of temperatures, times and gas flows. It has been demonstrated that morphological and phase changes due to corrosive effects occur after exposure of the 3M material to a combustion environment for as little as 25 hours at 800°C. The study of heat exchanger materials has focused on enhancing the corrosion resistance of DuPont Lanxide Dimox™ composite tubes by adding chromium to its surfaces by (1) heat treatments in a Cr_2O_3 powder bed, or (2) infiltrating surface porosity with molten chromium nitrate. Each process is followed by a surface homogenization at 1500°C. The powder bed method has been most successful, producing continuous Cr-rich layers with thicknesses ranging from 20 to 250 μm. As-received and Cr-modified DuPont Lanxide Dimox™ samples will be reacted with commonly encountered coal-ash slags to determine the Cr effects on corrosion resistance.

INTRODUCTION

The objectives of this work are to: (a) study the corrosion and resulting changes in mechanical properties of candidate hot gas filter materials exposed to a combustion environment, and (b) compare the corrosion rates of the as-received and Cr-infiltrated $Al/Al_2O_3/SiC_p$ DuPont Lanxide Dimox™ heat exchanger materials in contact with the two commonly encountered coal-ash slags of a typical Illinois #6 composition, and a CaO-enriched Illinois #6. Our progress toward achieving these objectives is summarized below.

SCREENING ANALYSIS OF CANDIDATE CERAMIC HOT GAS FILTER MATERIALS

The corrosion testing of ceramic hot gas filters currently involves 3M's Type 203 filters (a SiC matrix-Nextel fiber composite) and DuPont Lanxide's SiC-SiC composite tubes with Nicalon fibers. In both cases the SiC matrix is produced by a chemical vapor

infiltration process. The initial tests involve flow-over exposures to a combustion atmosphere of ash-coated rings cut from tubes of these materials. The ash used to coat the rings was collected at the Tidd plant and is a product of the combustion of Pittsburgh #8 coal. A parametric study of time, temperature and total gas flow has been initiated to study corrosion effects and to generate systematic corrosion data. Time permitting, a study of the effect of gas composition on corrosion rates will also be undertaken. These data will provide a baseline for corrosion testing of mini-candles in a flow-through configuration.

Experimental Conditions

The experimental conditions involved in the parametric study of time, temperature and gas flow are presented in Table 1. The baseline gas composition is the same as that used at the University of North Dakota Energy and Environmental Research Center (UNDEERC), where it was determined to be representative of the combustion environment experienced by hot gas filters in a pressurized fluidized bed combustor (PFBC). The range of temperatures was chosen because it is also representative of the conditions to which candle filters are exposed during use. Flow rates and exposure times were chosen to be practical for running laboratory tests and generating systematic corrosion data in a reasonable time frame. Short duration exposures have not been reported previously and a

Table 1: Experimental conditions used in a flow-over configuration to study corrosion effects on filter materials in simulated coal combustion environments.

Parameter	Values
Temperature (°C)	800, 870, 950
Time (hr)	10, 25, 50
Flow rate (slm)	1, 2.5, 5
Baseline gas composition: N_2 (%)	66.5
CO_2 (%)	15
O_2 (%)	3
H_2O (%)	15
SO_2 (%)	0.5
NaCl (ppm)	10

significant amount of corrosion may occur in the early exposure of filter materials to combustion environments.

Results and Discussion

Corrosion effects were observable for test conditions of 800°C, 25 hours and a flow rate of 2.5 slm. Figure 1 contains scanning electron micrographs of SiC-coated fibers in the middle layer of a 3M filter as-received (Fig. 1a) and after exposure to these conditions (Fig. 1b). This layer is the part of the material which actually filters the ash from the combustion gases. The morphology of the coating is significantly altered by this exposure. In the as-received sample, the SiC grains are observed to have a typical CVD film structure sometimes referred to as a "cauliflower" morphology. After only 25 hours in a combustion environment, the surface of the SiC coating has a glazed or glassy appearance and is less uniform. The surface appears to have been coated with reaction products of the gas phase species or to have reacted with the combustion gases. It has not yet been determined whether the thicknesses of the fibers are increasing or decreasing as a result of this interaction. No changes were observed on the surface of the inner, or support, layer of the exposed filter ring.

Pieces of the middle layers of the samples shown in the micrographs in Fig. 1 were crushed in a mortar and pestle and mounted on glass slides for x-ray diffraction (XRD) analysis. The resulting spectra are shown in Fig. 2. SiC was the only phase positively identified on both patterns. The SiC is probably a mixture of polytypes, but it most closely matches the powder diffraction pattern for the 15R polytype of SiC (JCPDS file number 39-1196). A trace amount of mullite (JCPDS file number 15-776) may also be present. The only discernible difference between the spectra is a broad hump between 20 and 30 degrees 2-theta, indicating an amorphous component, on the pattern for the sample which was exposed to the combustion environment (scan b in Fig. 2). No discernible differences were observed on the XRD patterns for the inner layer of the filter before and after exposure. In addition to SiC, mullite was identified as a minor phase on these spectra.

Summary and Future Research on Hot Gas Filter Materials

Initial exposure testing of 3M's fiber composite hot gas filter material has confirmed that corrosive effects are observable after short term exposure times to PFBC conditions.

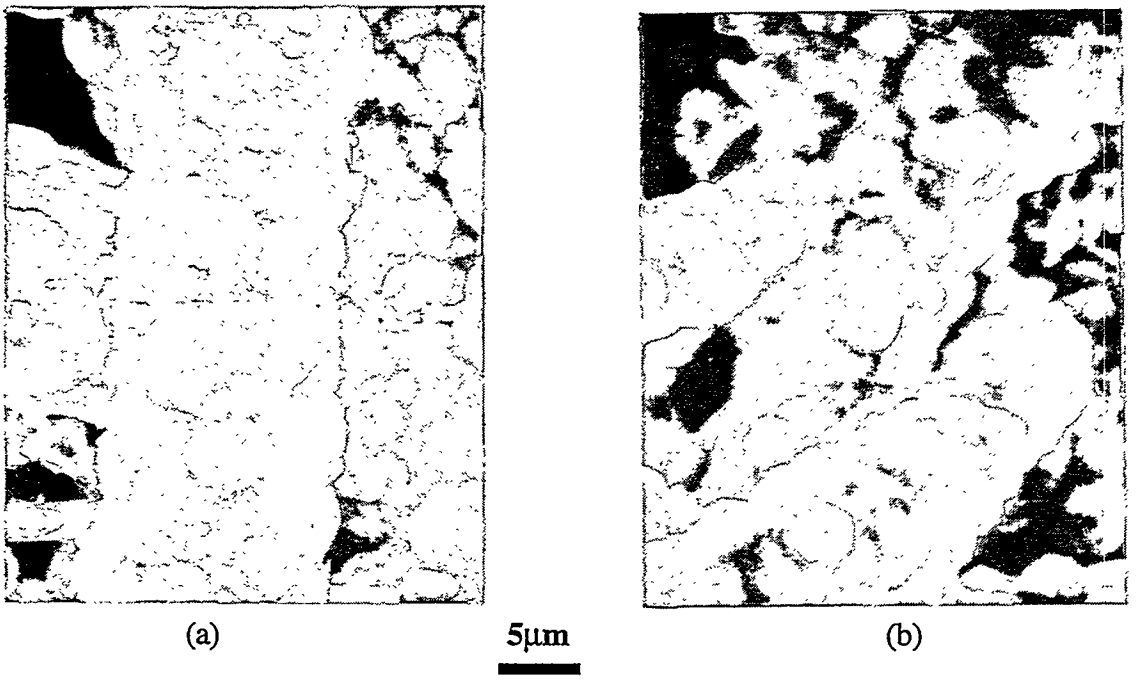

Fig. 1. Scanning electron micrographs of fibers from a 3M hot gas filter (a) as-received and (b) exposed to a combustion environment at 800°C for 25 hours at a flow rate of 2.5 slm.

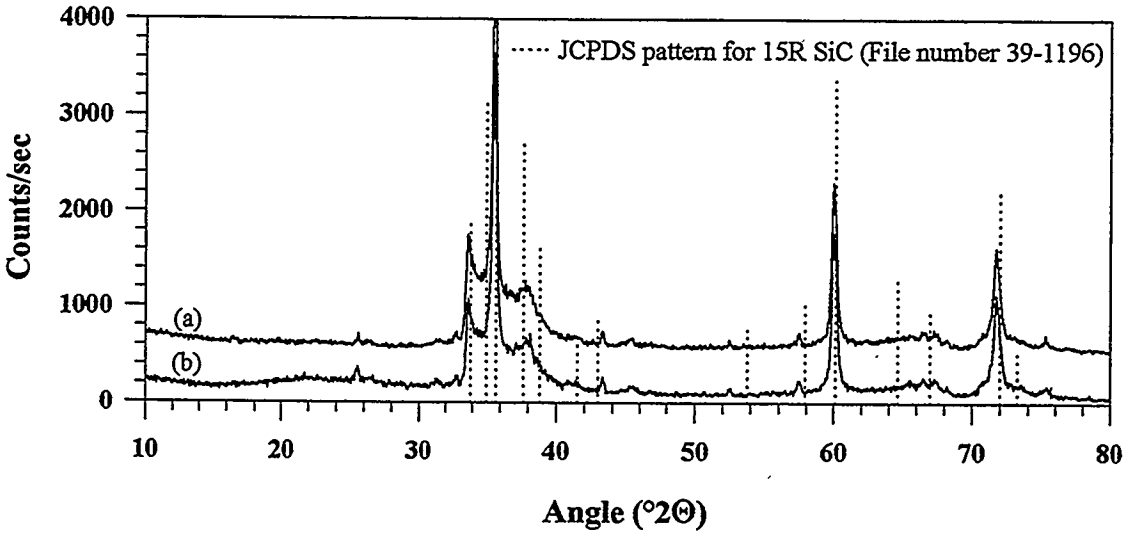

Fig. 2. X-ray diffraction spectra for the middle (filtering) layer of a 3M hot gas filter (a) as-received and (b) exposed to a combustion environment at 800°C for 25 hours at a flow rate of 2.5 slm.

Morphological changes were seen on the surfaces of the coated fibers in the filtering layer of the filter material. XRD analysis showed the presence of an amorphous component in this layer as well. This result correlates with the glassy or glazed appearance of the fiber surfaces observed using scanning electron microscopy. The matrix of experiments presented in Table 1 is currently being run on the 3M material to develop systematic corrosion data at these combustion conditions. The same set of experiments will be run on the DuPont Lanxide material when it is received.

Longer term, 200 hour, exposures of mini-candles will be initiated when the baseline corrosion data has been determined using rings of candles exposed in the flow-over tests. The experimental parameters for these tests will be chosen based on results from the flow-over tests in conjunction with thermochemical calculation results. The exposed candles will be analyzed in the same way as the rings in the flow-over tests as well as being cut into rings for mechanical property testing. The expected result will be correlations of exposure conditions with corrosion effects and mechanical properties.

CERAMIC HEAT EXCHANGER MATERIALS WITH CHROMIUM SURFACE TREATMENTS FOR CORROSION RESISTANCE

Ceramic heat exchangers in coal-fired power plants are exposed to extremely harsh environments, with the temperatures reaching up to 1600°C and a variety of coal combustion products causing both corrosive and erosive damage to the material.[1] Candidate DuPont Lanxide Dimox™ Al/Al_2O_3/SiC_p composites have shown a favorable combination of thermal conductivity, mechanical properties (creep resistance and hot strength), oxidation/corrosion resistance in fossil fuel environments, and thermal shock resistance.[2] However, when in contact with the alkali and alkaline-earth rich slags, accelerated corrosion of the composite is likely because of the formation of the low-melting silicate phases on the surface. Since chromium oxide has a very low solubility in silica and molten silicates, and the corrosion rate of alumina–chromia solution phases in CaO–MgO–Al_2O_3–SiO_2 melts decreases with an increase in Cr_2O_3 concentration,[3] it is expected that a DuPont Lanxide Dimox™ composite surface modified with Cr_2O_3 will resist liquid formation and provide improved corrosion resistance as compared to the Cr_2O_3-free composite. The following sections describe two methods of infiltrating Cr_2O_3 into the DuPont Lanxide Dimox™ composite, and present the results of the SEM and EDX analyses of the infiltrated material.

Experimental Procedure

The chromium infiltration of the $Al/Al_2O_3/SiC_p$ DuPont Lanxide Dimox™ heat exchanger material was accomplished by one of two methods: (1) heating the composite in a Cr_2O_3 powder bed, and (2) heating the composite in molten $Cr(NO_3)_3 \cdot 9\ H_2O$. Both types of infiltrated samples were subjected to a heat treatment at 1500°C prior to corrosion testing. This heat treatment was performed to ensure the Cr in-diffusion, as well as to reoxidize and homogenize the specimen surfaces. The experimental conditions employed in methods (1) and (2) are summarized in Tables 2 and 3, respectively.

Table 2. Experimental conditions for DuPont Lanxide Dimox™ composite surface modification in Cr_2O_3 powder bed.

Sample #	Infiltration Temperature/Time	Equilibration Temperature/Time
1	1000°C/2 h	1500°C/2 h
2	1100°C/2 h	1500°C/2 h
3	1100°C/12 h	1500°C/2 h
4	1100°C/12 h	1500°C/6 h

Table 3. Experimental conditions for DuPont Lanxide Dimox™ composite surface modification in molten $Cr(NO_3)_3 \cdot 9H_2O$.

Sample #	Surface Pre-treatment	Cr-Nitrate Infiltration*	Cr-Nitrate Decomposition	Surface Equilibration
5	1100°C/12 h	80°C/24 h	600°C/1 h	1500°C/2 h
6	1100°C/12 h	80°C/24 h	600°C/1 h	1500°C/6 h
7	conc HCl / 12 h	80°C/24 h	600°C/1 h	1500°C/2 h
8	conc HCl / 12 h	80°C/24 h	600°C/1 h	1500°C/6 h

* Subsequent drying at room temperature for 48 h.

In method (1), the purpose of the low-temperature heat treatment at 1000° or 1100°C was to recreate the conditions for the Dimox™ process which causes the simultaneous melting, growth and oxidation of the residual Al from the composite. Consequently, the Cr_2O_3 from the powder bed could be trapped within the molten Al on the composite surfaces. In method (2), the heat treatment at 1100°C (equivalent to the

Dimox™ process) or, alternatively, the chemical treatment in concentrated HCl (by etching the residual Al) allowed for the formation of residual porosity on the specimen surfaces. The molten chromium (III) nitrate subsequently penetrated the surface pores by capillary action. Prior to surface equilibration at 1500°C, the Cr-nitrate was decomposed into an oxide at 600°C. SEM and EDX analyses of the polished cross sections of the specimens heat treated at 1500°C were performed to determine the extent of Cr penetration.

The as-received and selected Cr-infiltrated composite materials are being reacted with typical slags for various times and temperatures, and will be characterized to determine the effects of the chromium surface treatments on corrosion resistance. The slags are commonly encountered coal-ash slags of an Illinois #6 composition, and a CaO-enriched Illinois #6.

Results and Discussion

The results of the SEM and EDX analyses performed on the specimens heated in Cr_2O_3 powder bed are summarized in Table 4, indicating the dramatic effects of heat treatment time and temperature on the thickness and continuity of the Cr-rich layer, and the roughness of the resulting specimen surfaces. It appears that a satisfactory compromise among the surface characteristics to warrant further corrosion studies was achieved in Specimens #1 and #4.

Table 4. SEM and EDX results for specimens infiltrated in a Cr_2O_3 powder bed.

Sample #	Average Cr-Layer Thickness (μm)	Cr-Layer Continuity	Surface Roughness
1	20 ±2	Yes	Minimal
2	outer surf. 100 ±10 inner surf. 200 ±60	No	Substantial
3	200 ±25	No	Substantial
4	250 ±40	Yes	Acceptable

An SEM micrograph of the near-surface layer of Specimen #4 is shown in Fig. 3. It was found by the EDX analysis that the Cr-rich layer observed in the upper portion of the photograph consisted of the Cr_2O_3 grains (brighter phase) embedded in a chromia–alumina–silicate matrix (darker phase). The appearance and distribution of the darker phase suggested that it had been formed from a liquid and was probably glassy. Minor amounts

of Ca were found within the darker phase, suggesting that the Ca was present in the as-received composite material.

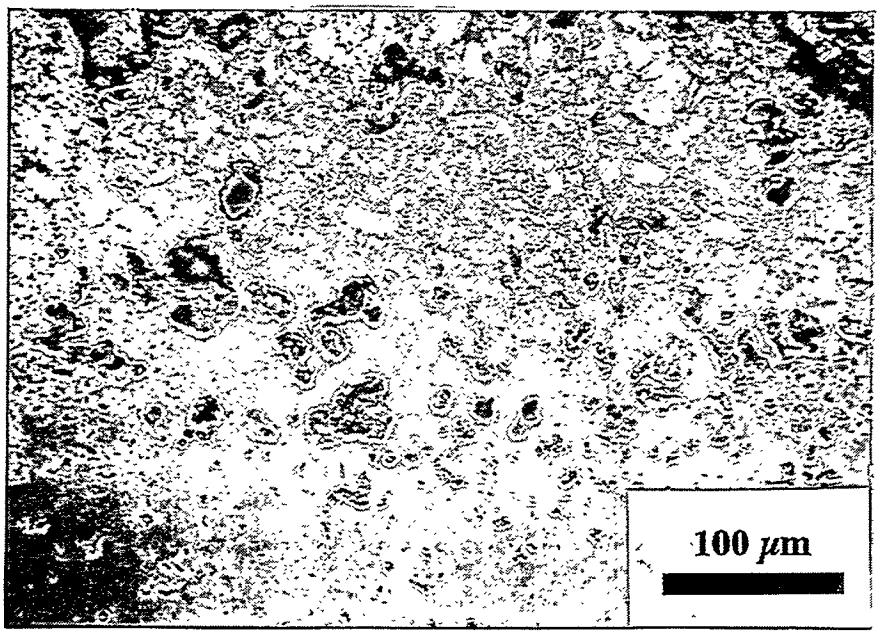

Fig. 3. SEM photograph of the near surface layer of a DuPont Lanxide Dimox™ Al/Al_2O_3/SiC_p composite infiltrated in a Cr_2O_3 powder bed for 12 h at 1100°C and equilibrated for 6 h at 1500°C.

Similar morphologies and compositions were observed in the other specimens. However, extensive regions of discontinuity in Cr distribution were found in the near-surface layers of Specimens #2 and #3. In addition, the average thickness of the Cr-rich layer in Specimen #2 was found to be substantially higher (approximately by a factor of 2) on the inner wall of the specimen as compared to the outer wall. This unexpected effect was not observed in any of the other specimens infiltrated in the Cr_2O_3 powder bed. It is also believed that the substantial amount of damage and porosity observed in the Cr-rich layers were in part caused by the sample preparation procedure, which involved high-speed cutting and diamond-wheel grinding of the cross sections.

Among the specimens infiltrated with Cr-nitrate, minor amounts of chromium were detected only in the outer surface of Specimen #8 (leached for 12 h in HCl and equilibrated for 6 h at 1500°C). The SEM photograph of this specimen is presented in Fig. 4, and shows the formation of a 50 ± 8 μm thick modified surface layer only slightly enriched

with Cr. Apparently, surface porosity created in Specimens #5 through #8 was insufficient to allow any substantial penetration of molten Cr-nitrate by capillary action at 80°C. It is possible, however, that an additional heat treatment step at 1100°C, after the decomposition of the nitrate had been completed, might have improved the infiltration and yielded higher surface concentration of chromium in Specimen #8. At this stage, however, it was concluded that the Cr-nitrate treatment did not yield the surface characteristics required to improve the corrosion resistance.

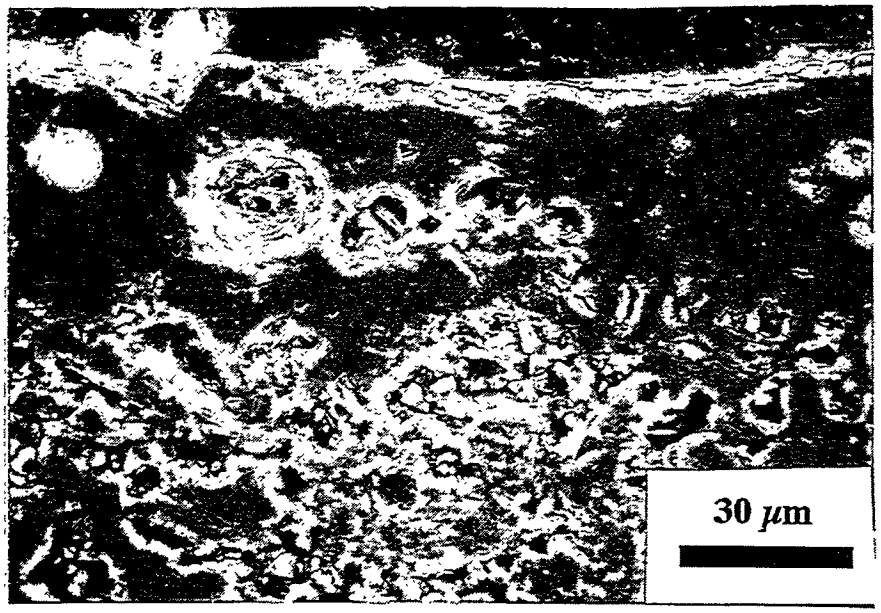

Fig. 4. SEM photograph of a near surface layer of the outer wall of a DuPont Lanxide Dimox™ $Al/Al_2O_3/SiC_p$ composite etched for 12 h in concentrated HCl, infiltrated with $Cr(NO_3)_3 \cdot 9\ H_2O$ for 24 h at 80°C, and equilibrated for 6 h at 1500°C.

Summary and Future Research on Heat Exchanger Materials

(1) The Cr-infiltration of the DuPont Lanxide Dimox™ $Al/Al_2O_3/SiC_p$ composites in a Cr_2O_3 powder bed generated continuous Cr-rich layers with the thicknesses ranging from 20 to 250 μm.

(2) The Cr-infiltration in molten $Cr(NO_3)_3 \cdot 9\ H_2O$ was found to be insufficient to produce any substantial penetration of Cr into the composite surfaces.

The composite specimens heat treated in Cr_2O_3 powder bed under two different sets of conditions were selected for further corrosion studies in contact with Illinois #6 and

CaO-enriched Illinois #6 slags. The corrosion tests are currently under way and will be followed by a detailed examination of the morphologies and compositions of the surface reaction layers formed at the composite/slag interfaces.

ACKNOWLEDGMENTS

We would like to thank D. Pysher (3M Co.), P. Gray (DuPont Lanxide Composites Inc.), and D. Landini (DuPont Lanxide Composites Inc.) for providing the samples for this work, and J.P. Hurley (UND EERC) for helping us obtain the ash and slags for corrosion testing. This research was sponsored by the United States Department of Energy, Office of Fossil Energy, Advanced Research and Technology Development Materials Program (DOE/SE AA 15 10 10 0), Subcontract 38X-SS111C, WBS Element PSU-4 administered by Martin Marietta Energy Systems, Oak Ridge, TN 37831.

REFERENCES

1. K. Breder and V. J. Tennery, "Materials Support for the Development of High Temperature Advanced Furnaces (HITAF)—A Comparison of Selected Mechanical Properties for Three SiC-Based Ceramics"; A Discussion of DOE-Sponsored Fossil Energy Research Projects. The Pennsylvania State University, University Park, PA (1994).

2. C. R. Kennedy, "Reinforced Ceramics Via Oxidation of Molten Metals," *Ceram. Ind.*, 26–29, December 1994.

3. K. H. Sandhage and G. J. Yurek, Indirect Dissolution of $(Al,Cr)_2O_3$ in CaO–MgO–Al_2O_3–SiO_2 (CMAS) Melts," *J. Am. Ceram. Soc.*, **74** [8] 1941–54 (1991).

THERMAL AND STRUCTURAL ANALYSIS OF A FILTER VESSEL CERAMIC TUBESHEET

R.H. Mallett

Mallett Technology, Inc.
PO Box 14407
Research Triangle Park, NC 27709-4407

R.W. Swindeman

Oak Ridge National Laboratory
PO Box 2008
Oak Ridge, TN 37831-6084

J.F. Zievers

Industrial Filter & Pump Mfg. Co.
5900 Ogden Avenue
Cicero, IL 60650-3888

ABSTRACT

A ceramic tubesheet assembly for a hot gas filter vessel is analyzed using the finite element method to determine stresses under differential pressure loading. The stresses include local concentration effects. Selection of the stress measures for evaluation of structural integrity is discussed. Specification of stress limits based upon limited data is considered. Stress results from this ongoing design analysis technology project are shown for one design concept.

INTRODUCTION

A transport combustor is being commissioned at the Southern Services facility in Wilsonville, Alabama to provide a gaseous product for the assessment of hot-gas filtering systems. Foster-Wheeler will install a Pressurized Fluidized Bed Combustor (PFBC) to burn carbonizer product and a hot gas filter will be installed in the PFBC gas stream. One of the barrier filters incorporates a ceramic tubesheet to support the candle filters. The ceramic tubesheet system, designed and built by Industrial Filter and Pump Manufacturing Company (IF&PM), is somewhat unique and offers distinct advantages over metallic systems. This design analysis project is applying a design methodology applicable to the thermal-mechanical analysis of an all-ceramic system.

TECHNICAL APPROACH

A design analysis problem is defined by its geometry, material properties and applied loading. This step has been formalized into creation of a Design Analysis Specification [1].

Tubesheet Geometry

The geometry of the tubesheet is defined in design drawings. The tubesheet is circular with an outside diameter of approximately 55 inches and an inside diameter of 11 inches. The tubesheet is supported at the outside diameter by a ledge attached to the filter vessel. The inside diameter of the tubesheet is attached to an inlet downcomer pipe through which dirty gas enters the filter vessel.

The tubesheet contains many penetrations into which filter candles are inserted. The hot gas is filtered as it passes from the lower dirty gas plenum through the filter candles into the upper clean gas plenum. The penetration pattern repeats at 60° intervals around the circle formed by the tubesheet.

The thickness of the illustrative tubesheet design analyzed herein is a composite construction. Upper and lower layers of 3-inch thickness are separated by a 5-inch layer. This sandwich construction relies on the outer layers to resist bending while shear resistance is provided by the core layer.

Tubesheet Materials

The upper and lower layers of the tubesheet are aluminosilicate composite materials. Further details are beyond the scope of this design analysis project and test data are very limited.

The shear core in this design concept is specified as a Fibrosics™ material constructed from a blend of aluminosilicate fibers and binders of silica and alumina. This shear core is a low density material.

Tubesheet Loading

The design analysis specification of Reference 1 defines the service which the tubesheet must withstand. This includes thermal and mechanical loadings from various operating conditions and transients including backflow pulses to dislodge the dustcake from the filter candles.

The differential pressure across the tubesheet rises to 4 psi as dustcake accumulates. At 4 psi, backflow pulses dislodge the dustcake and the differential pressure returns to a nominal 1.5 psi. Nevertheless, a differential design pressure of 15 psi is specified for the tubesheet. This is a dominant load case and is the loading used for preliminary evaluation of tubesheet design concepts.

ANALYSIS RESULTS

Figure 1 shows the finite element analysis model used for the tubesheet. This is a 30° sector of the tubesheet. This model is sufficient for determining stresses throughout the 360° tubesheet because of the repetitive pattern of the candle filter penetrations [2]. Figure 2 is a close-up view of the region near the inside diameter of the tubesheet.

The thickness of the analysis model includes separate sections for the upper and lower layers and for the shear core. Thin bond layers are also provided between the major material layers.

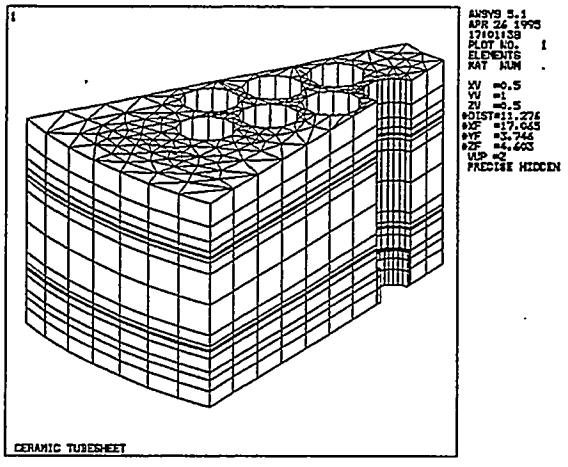

Figure 1. Overall Analysis Model

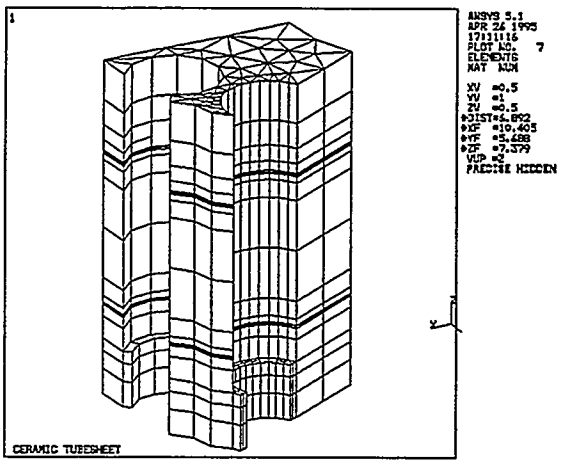

Figure 2. Local Analysis Model

Figure 3 shows a contour plot of the stress intensity distribution caused by a differential pressure of 15 psi. The maximum stress intensity occurs in the ligaments between the penetrations and at the support ledge.

Figure 4 focuses on the high stress region near the inside diameter of the tubesheet. Figure 5 shows a profile of the hoop stress up the edge of the hole.

The maximum stress intensity value in the upper and lower layers is 490 psi. The maximum stress intensity in the shear core is 97 psi. The maximum stress intensity in the bond layer is 129 psi.

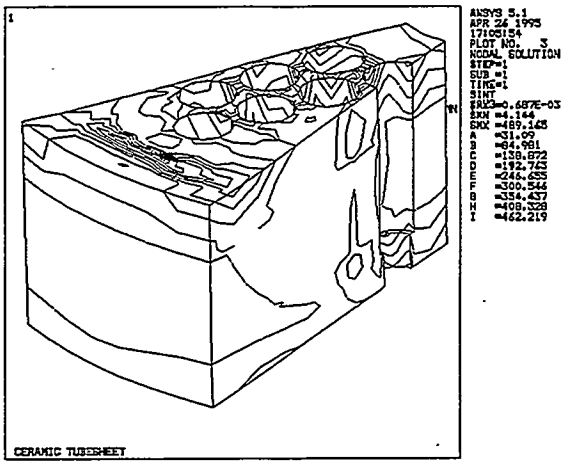

Figure 3. Stress Distribution

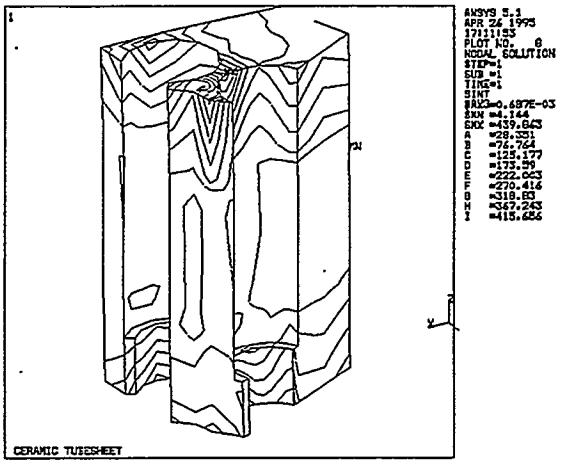

Figure 4. Local Stress Distribution

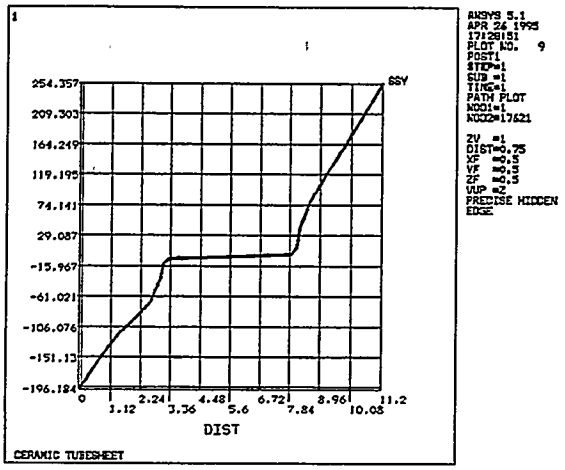

Figure 5. Hoop Stress Through Thickness

DESIGN EVALUATION

If a material has sufficient ductility, local peak stresses are attenuated by local strains without causing failure of the component although repeated applications may cause fatigue crack initiation. The determination of sufficient ductility is complex. Low ductility materials are often excluded from consideration because of material property variations and uncertainty in local stress concentration conditions and applied loadings.

Herein, we judge that the stress quantity which should be limited in the tubesheet bending case is the total (peak) stress. This judgement is based upon observation that the stress peaks in Figure 5 are not highly localized. This judgement also is made on the assumption that the material strength data will be determined using bend tests. Such tests are considered to represent conditions similar to the in-situ conditions in the tubesheet under differential pressure.

In summary, the materials are considered to have low ductility; not zero ductility. The stress distribution in the tubesheet is bending somewhat similar to a bend test. We will use the maximum bending stress from the bend test to limit the total (peak) stress in the tubesheet.

It remains to determine the design stress limit such that there is sufficient margin to the failure stress. Very few data are available. There is no statistical characterization of the failure stress.

We proceed on judgement. The failure distribution is judged to lie largely with a range of +/- 33% about the average test failure stress. On this basis, the design stress limit is taken as 1/3 of the average failure stress. For example, if the average failure stress is 2,700 psi, the range of data is taken to be from 1,800 psi to 3,600 psi and the design stress limit is specified as 900 psi.

CONCLUSIONS

The design analysis rationale for the ceramic tubesheet includes encouragement to develop a mechanical design concept with inherent ductility. The use of a relatively soft shear core is an example of this.

The design analysis rationale is also encouraging the use of a mechanical design concept with inherently low stress. The key to low stress in the tubesheet is to use a large thickness value.

Finally, the design evaluation is encouraging the use of feature tests for determination of mechanical and strength properties. Using tests which are representative of conditions in-situ can compensate for the limited data and understanding regarding the material properties.

REFERENCES

1, R.H. Mallett, "Design Analysis Specification for Filter Vessel Ceramic Tubesheet (Draft)", Mallett Technology Report MTI-TR-825, February 3, 1995.

2. R.H. Mallett, "Preliminary Design Analysis for a Filter Vessel Ceramic Tubesheet", Mallett Technology Report MTI-TR-845, February 6, 1995

PROCESSING OF SILICON NITRIDE AND ALUMINA NANOSIZE POWDERS

Eduardo J. Gonzalez, Gasper Piermarini, Bernard Hockey and
Subhas G. Malghan

Ceramics Division
National Institute of Standards and Technology
Gaithersburg, MD 20899

ABSTRACT

The effects of pressure on the compaction and subsequent processing of nanosize γ alumina powders were studied. A 3 mm diameter piston/cylinder die was used to compact the nanosize powders to pressures of 1 and 2.5 GPa. The green bodies were sintered at temperatures up to 1600 °C. Results show that green body density can be increased by higher compaction pressures. It appears that as a result of the γ-to-α transformation in alumina, higher green density does not necessarily produce a higher density sintered alumina body. The microstructures of the sintered bodies are described in terms of porosity and phase content.

INTRODUCTION

The primary objective of this project is to develop a novel compaction process to produce a dense green-state compact from nanosize powders that subsequently can be sintered to form a dense ceramic, possibly with nanoscale microstructure. Earlier work involved efforts to compact nanosize (average particle size, 17 nm) amorphous silicon nitride powders into dense green body compacts followed by sintering to produce a dense ceramic with nanoscale microstructure. The results of those efforts led to the following conclusions: (1) a random packing green body density of about 57% of theoretical can be achieved by dry compaction of the nanosize powder to 2.5 GPa. Green body density can be increased to 64% by using liquid nitrogen as a lubricant during the compaction process. The transparent green compacts were pressureless sintered at 1400 °C and yielded a sintered piece with a Vickers hardness of about 6 GPa. Not a very promising result. Hot pressing the transparent green body followed by pressureless sintering improved the hardness to 11 GPa, but still not anywhere near the 25-30 GPa values characteristic of conventional silicon

nitride ceramic. Sintering at temperatures higher than 1400 °C produced a phase transformation to α silicon nitride with a loss of transparency and no improvement in hardness. The interpretation of these compaction and sintering results is difficult because the amorphous nanosize silicon nitride powder experiences a crystallization to α phase and an additional transformation to β phase at higher temperatures.

To better understand the effects of phase transformation on the densification process occurring during sintering, nanosize γ alumina powder was studied. The existence of a variety of transitional alumina phases already has attracted considerable attention because of their importance in affecting the processing parameters for alumina ceramics [1]. One of the main interests in the transitional alumina phases is their possible effects on densification which occurs in the sintering process during which the α Al_2O_3 ceramic is formed. Some authors have reported that the transformation process enhances the densification kinetics and lowers the sintering temperature required to produce dense samples of α Al_2O_3 [2]. It is well known that the phase transformation in alumina occurs by a nucleation and growth process, but the mechanisms by which the transformation enhances densification are not well understood. Nevertheless, polycrystalline, dense α Al_2O_3 ceramics have been made by sintering transitional γ phase green bodies at temperatures as low as 1150 °C, while maintaining almost the original grain size of the starting powder in the sintered body. Kumagai and Messing [2], for example, studied the effects of seeding sol-gel derived transitional oxides of aluminum with submicrometer size α Al_2O_3 crystals. These authors showed that the θ-to-α transformation temperature was reduced to 1200 °C by seeding, and that the transformed α alumina sinters to full density with a submicrometer grain size. Yeh and Sacks [3] used a somewhat different approach and made slurries of fine grain α Al_2O_3 (0.2 - 0.3 μm) using conventional suspension techniques. The slurries were slip-casted into pellets of relatively high densities (69%). These pellets were sintered at 1150 °C to almost full density with very little increase in grain size. They demonstrated that the transformation was not necessary to achieve high densities at low sintering temperatures.

Another method of increasing the rate and lowering the temperature of the transformation in alumina was reported by Ishitobi *et al*, [4] and later by Dynys and Halloran [1]. Ishitobi *et al*, [4] demonstrated that sintering η Al_2O_3 or θ Al_2O_3 under pressures of several gigapascals decreases the transformation temperature significantly. Dynys and Halloran, on the other hand, showed that cold compaction at different pressures changes the transformation kinetics under pressureless sintering in a similar fashion. The residual stresses in the green body produced by compaction of the starting powder is thought to increase the number of nuclei at which the transformation initiates.

In the present work, we describe the microstructure and densification that develops as a result of the γ-to-α transformation in nanosize γ Al_2O_3 powder, and show how it is affected by the magnitude of the initial compaction pressure used to fabricate the green body. The results have implications concerning the difficulties experienced in the processing of nanosize silicon nitride powders where transformations from the amorphous state to α and β Si_3N_4 crystalline forms occur.

EXPERIMENTAL PROCEDURES

The starting nanosize γ Al_2O_3 powder used in this work is a commercially available material, Aluminum Oxide C, supplied by Dugussa*, AG, Geschäftsbereich Anorganische Chemieprodukt, Frankfurt, Germany. The powder, consisting of equiaxed particles with an average diameter of 20 nm, is primarily γ phase with some δ phase, estimated from diffraction intensities to be <10% by volume, as determined by transmission electron microscopy (TEM) and x-ray powder diffraction (XRPD) techniques. The powder is strongly agglomerated with no evidence of partial sintering. Green body samples of 3 mm diameter were pressed to 1 and 2.5 GPa in an Instron Press described in detail elsewhere [5]. Sintering experiments were conducted in an alumina tube-furnace under the rough vacuum of a

*Certain commercial names are identified in this paper to foster understanding. Such identification does not imply recommendation or endorsement by the National Institute of Standards and Technology.

mechanical pump. Samples were sintered at 1000, 1100, 1200, 1300, 1500, and 1600 °C for 5 h, employing heating and cooling rates of 300 °C/h. After the heat treatments, the weight and volume of the samples were remeasured to determine the extent of densification. To further understand the densification process, optical microscopy, x-ray diffraction, TEM and surface area analysis were used to characterize the microstructure of the samples. The details of the green body preparation, sintering procedure and microstructural determination are described in a recent report [6].

RESULTS AND DISCUSSION

Densification Results

To summarize our results the average density at each sintering temperature and compaction pressure is illustrated in Figure 1. The density increases monotonically for both compaction pressures.

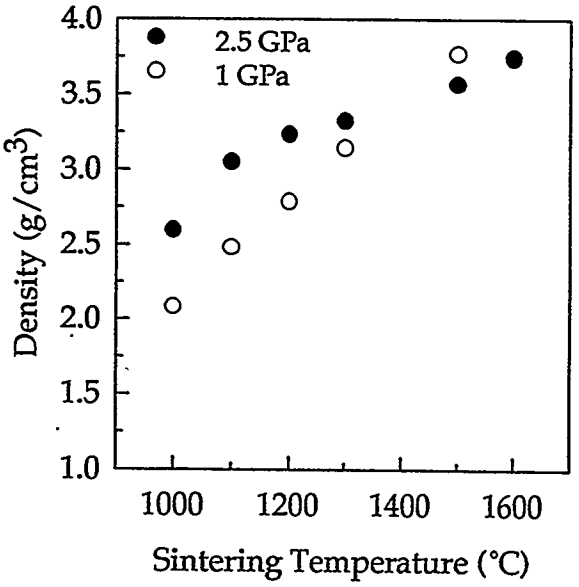

Figure 1. Plot shows monotonic increase in density with sintering temperature for γ-alumina samples compacted at 1 and 2.5 GPa.

However, it is of interest that the average density of the samples pressed to 1 GPa and sintered at 1500 °C was higher than the average density of the samples pressed to 2.5 GPa and also sintered at 1500 °C. The measured densities of the 1 GPa and 2.5 GPa pressed samples are 3.80 and 3.58 g cm^{-3}, or 96% and 90% relative density, respectively (theoretical density of α Al_2O_3, 3.98 g cm^{-3}). However, after sintering at 1600 °C, the difference in relative density is more subtle.

Microstructure

Figure 2 shows a TEM micrograph of a green body compacted at 2.5 GPa. Both XRPD and electron diffraction results on these samples confirmed that they are predominantly γ Al_2O_3. The γ particles are equiaxed with an average size of $\approx$ 20 nm.

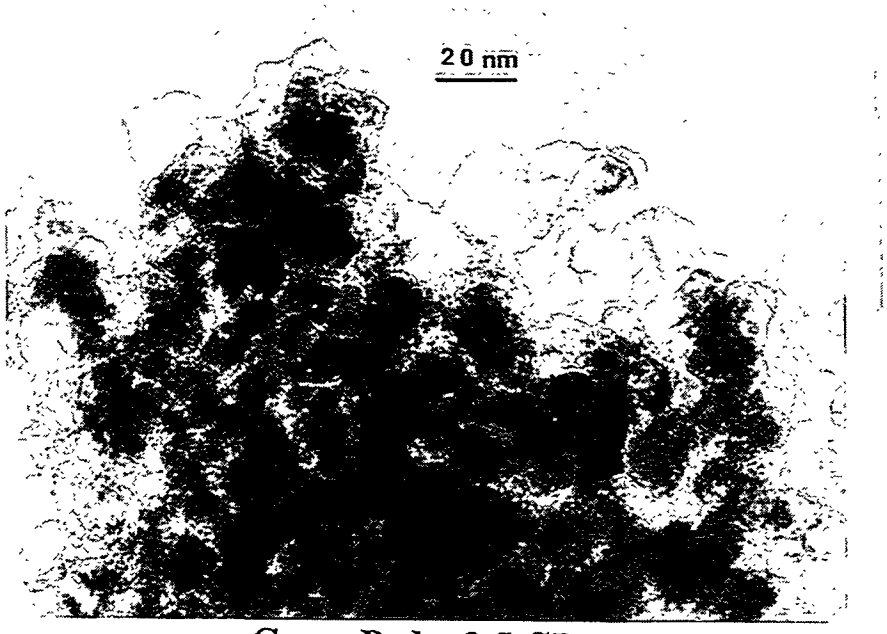

Figure 2. TEM brightfield image shows the microstructure of a green body of γ-Al_2O_3 compacted at 2.5 GPa.

More generally, observations on samples compacted to 1.0 and 2.5 GPa indicate a random dense packed particle structure with uniform interconnected porosity. For both compaction pressures, the pore dimensions were less than the particle size. As a consequence, the 16% difference in packing density between the samples compacted at 1 and 2.5 GPa was not resolved by TEM.

Figures 3 (a and b) show, in comparison, TEM micrographs of the samples sintered at 1000 °C for the 1 and 2.5 GPa compaction pressures.

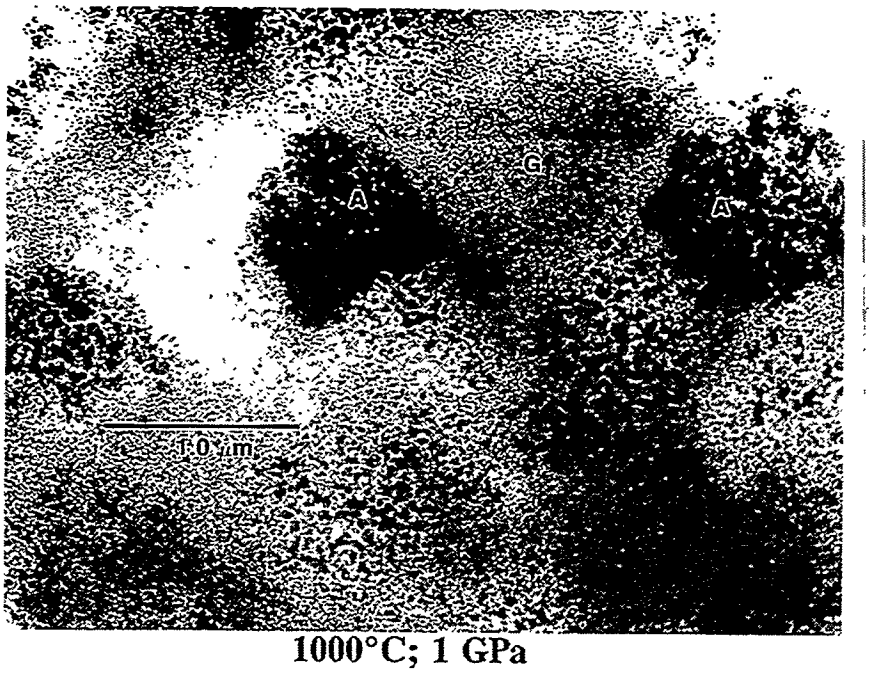

Figure 3a. Brightfield image in TEM shows the typical microstructure of γ-alumina samples sintered at 1000 °C for a) 1 GPa.

The sample compacted at 1 GPa is made of a mixture of equiaxed particles of γ phase and isolated clusters of predominantly α phase. Even at this temperature, necking between γ particles, indicative of partial sintering, was not observed by TEM. The isolated α clusters grow in a spongy structure with continuous porosity. XRPD results confirmed that both α and γ phases were present in the samples pressed to 1.0 GPa.

In contrast, the samples pressed to 2.5 GPa consisted of all α phase, with spongy microstructure morphology and continuous porosity similar to the isolated α clusters in the 1 GPa pressed samples. Again, XRPD confirmed that the 2.5 GPa pressed samples are exclusively α Al_2O_3.

It should be noted that the spongy α phase microstructure consists of interconnected individual grains, ranging in size from about 100 nm to nearly 1 μm. As illustrated in Figure 3b, regions of dark contrast define areas of common orientation, the grains have a complex morphology, and the boundaries connecting adjacent grains are typically 50 to 100 nm long.

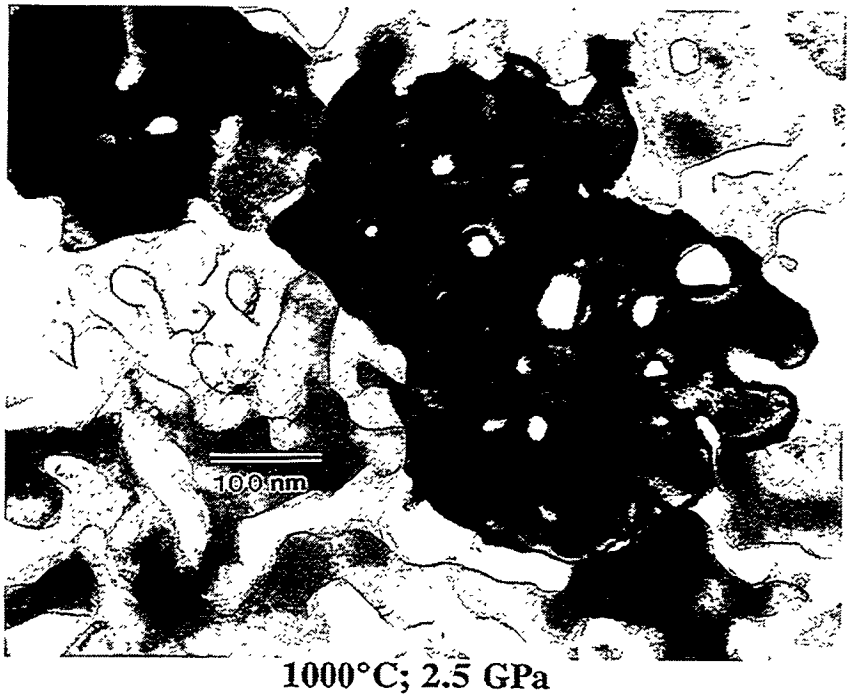

Figure 3b. Brightfield image in TEM shows the typical microstructure of γ-alumina samples sintered at 1000 °C for b) 2.5 GPa.

Surface area and pore size distribution analysis was done on selected green and sintered bodies. The results indicate that for fully transformed samples (all α phase), the average pore radius increases by a factor of 4 to 5 and the surface area decreases by a factor of 3 to 5, in agreement with the TEM observations.

The samples pressed at 2.5 GPa, which already transformed to α Al_2O_3, experienced some shrinkage during transformation to the α phase for the

same mass of material, and, as a result, these samples have a higher bulk density. Likewise, because the transformed volume in the 1 GPa samples is small compared to the 2.5 GPa material, the measurements cannot resolve this volume change. We have also done careful microstructural studies on samples sintered at 1300 °C. The density of these samples did not exceed 83% of theoretical. It was determined by XRPD that the samples are all α Al_2O_3 for both 1 and 2.5 GPa compacted samples. The 1 GPa samples are made up of a combination of the spongy grain structure and equiaxed micrometer size grains. Significant porosity and necking between grains is evident. In contrast, the 2.5 GPa compacted sample exhibited only an equiaxed grain morphology, and no evidence of spongy α phase structure.

The microstructures of the samples sintered at 1600 °C, shown in Figures 4(a and b), clearly illustrate the difference in volume fraction porosity and grain morphology. The sample compacted to 1 GPa has attained almost full density with some trapped porosity inside grains. Porosity in the 2.5 GPa compacted sample, on the other hand, is mostly intergranular with very little trapped porosity within grains.

In connection with the work of Dynys and Halloran [1], pressure does have an effect in the transformation kinetics. The 1 GPa compacted samples are partially transformed at 1000 °C, whereas the 2.5 GPa compacted samples have completely transformed to α Al_2O_3 under the same heat-treatment conditions. However, it is difficult to determine if the increase in pressure during compaction reduces the time and temperature for densification. Moreover, the nanoscale grain size is already lost when sintered at 1300 °C. It is unclear if the individual grains that form are the α Al_2O_3 clusters with reduced internal porosity. If this is the case, the starting size of the clusters determines the initial size of the grains. Therefore, it is necessary to control the cluster size or to start with α Al_2O_3 nanosize powders to avoid the transformation which appears to be responsible for cluster formation. This would have the effect of decreasing the final grain size after sintering.

The microstructures created at low temperatures in these studies are interesting for a number of reasons, however. The spongy structure of α Al_2O_3, for example, can be used as high temperature submicron ceramic

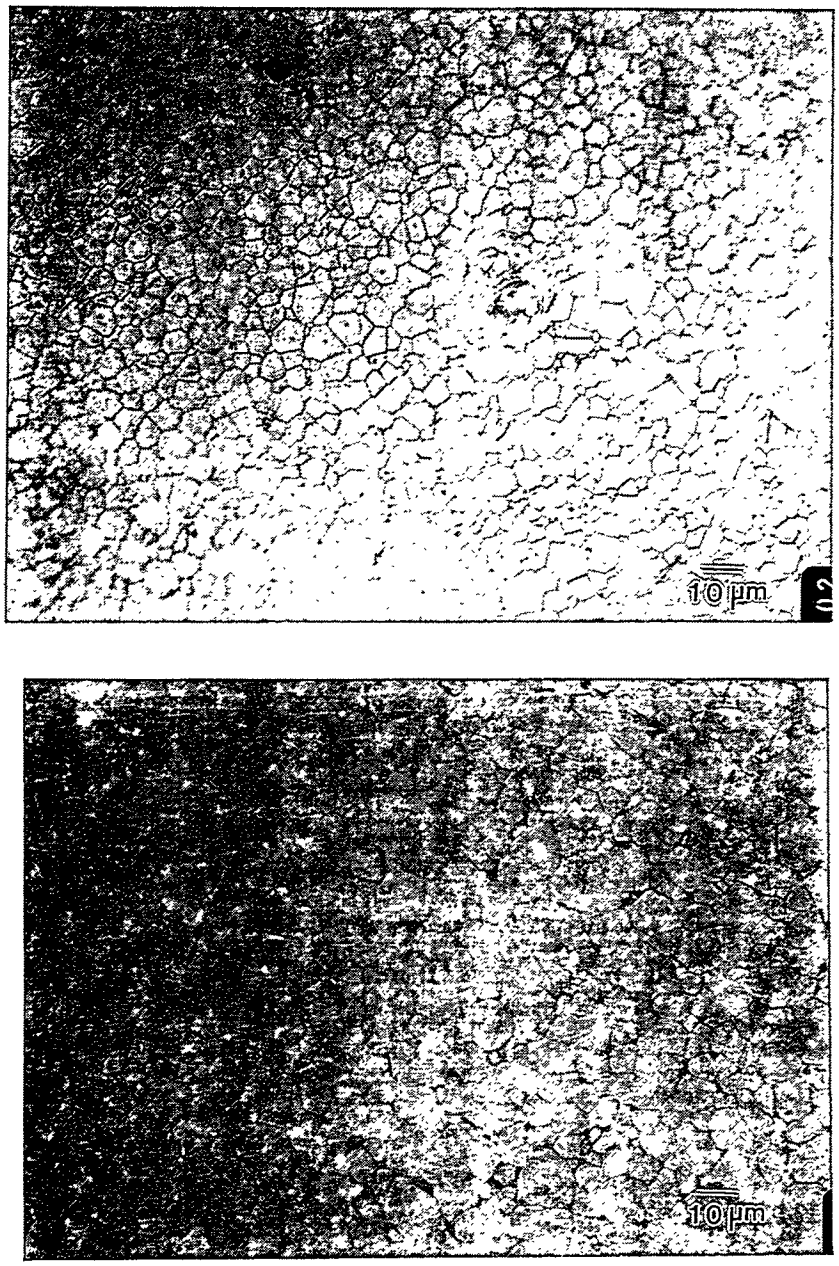

(a)

(b)

Figure 4. Microstructures of samples sintered at 1600 °C of (a) 1 GPa and (b) 2.5 GPa green compact.

filter, assuming that size distribution can be controlled over narrow ranges. Furthermore, some of these materials can be infiltrated with liquid metals to form composites with interesting properties.

CONCLUSIONS

The compaction pressure has an enhancing effect on (1) the green body density, (2) the γ-to-α transformation rate, and (3) the γ-to-α transformation temperature. In general, samples compacted to 1 GPa and sintered at temperatures below 1300 °C yielded consistently lower densities than the samples pressed to 2.5 GPa and sintered at the same temperatures. However, the densities of both samples approached the same value ($\approx$ 3.2 g cm^{-3}) for sintering at temperatures near 1300 °C. At higher sintering temperatures, the 1 GPa samples sintered at 1500 °C attained a higher density than the 2.5 GPa samples sintered at the same temperature, and for sintering at 1600 °C, the densities for the two samples appear to be nearly the same ($\approx$3.8 g cm^{-1}) at 96% of theoretical. In the case of silicon nitride processing, the mechanisms described here for alumina such as pressure effects on green body density, pressure effects on crystallization and on phase transformation, may also be relevant.

REFERENCES

1. F. W. Dynys and J. W. Halloran, "Alpha Alumina Formation in Alum-Derived γ Alumina", J. Am. Ceram. Soc., **65**, 442-448 (1982).

2. M. Kumagai and G. L. Messing, "Controlled Transformation and Sintering of a Boehmite Sol-Gel by α-Alumina Seeding", J. Am. Ceram. Soc., **68** [9] 500-505 (1985).

3. T. Yeh and M. D. Sacks, "Low-Temperature Sintering of Aluminum Oxide", J. Am. Ceram. Soc., **71** [10] 841-844 (1988).

4. Y. Ishitobi, M. Shimada and M. Koizumi, "Reactive Pressure Sintering of Alumina", Ceramic Bulletin, **59**, [12] 1208-1211 (1980).

5. W. Chen, A. Pechenik, S. J. Dapkunas, G. J. Piermarini and S. G. Malghan, "Novel Equipment for the Study of the Compaction of Fine Powders", J. Am. Ceram. Soc., **77**, [4] 1005-1010 (1994).

6. Eduardo J. Gonzalez, Gasper Piermarini, Bernard Hockey and Subhas G. Malghan, "Low Temperature Fabrication From Nanosize Ceramic Powders", Final Report to DOE, ORNL/Sub/92-22041/02, April 28, 1995.

SESSION II - CERAMICS AND NEW ALLOYS

DEVELOPMENT OF NONDESTRUCTIVE EVALUATION METHODS AND PREDICTION OF EFFECTS OF FLAWS ON THE FRACTURE BEHAVIOR OF STRUCTURAL CERAMICS

W. A. Ellingson, J. P. Singh, E. A. Sivers, J. B. Stuckey,
D. Christopher, S. L. Dieckman, and D. Singh

Energy Technology Division
ARGONNE NATIONAL LABORATORY
Argonne, Illinois 60439

ABSTRACT

Continuous fiber ceramic matrix composites are being developed for turbine engine components, heat exchangers, and hot-gas filters in fossil energy systems. Reliable application requires nondestructive evaluation (NDE) methods that provide data for quality assurance and inputs to life time prediction models and that aid in process development. NDE developments at Argonne have focused on methods to assess density distribution, fiber orientation (for mechanical properties), and defect detection in both SiC/SiC and Al_2O_3/Al_2O_3 materials, and that also assess the chemical state at fiber/matrix interfaces. 2-D cloth lay-up and 3-D weave CVI-infiltrated SiC/SiC specimens were studied by X-ray imaging methods now under development. Microfocus X-ray computerized tomography (MXCT) methods are being developed to provide these data. Multinuclear Nuclear Magnetic Resonance spectroscopy (13C, 29Si, and 11B) is under development for quantifying B content at fiber/matrix interfaces. Magic angle spinning techniques on SiC/SiC specimens with different coating thicknesses showed that quantification of B at the interface is achievable.

NDE data are being coupled to room- and elevated-temperature fracture studies to evaluate effects of fiber orientation and fiber coating thickness on resulting flaw morphology and mechanical properties of Nicalon-fiber–reinforced SiC matrix composites. Specifically, composites with fiber cloth lay-up sequences of varying coating thicknesses were evaluated. For room-temperature mechanical evaluation, composites with carbon-fiber coating thicknesses of 0 and 0.2 μm were used, while elevated-temperature studies used composites with a coating thickness of 0.4 μm. Composites with uncoated fibers failed in a brittle mode, while composites with 0.2 μm fiber coating showed noncatastrophic failure. Comparison of these results with previously obtained data for composites with coating thickness of 0.4 μm indicate that a coating thickness of 0.2 μm provides optimal mechanical performance.

INTRODUCTION

Nondestructive evaluation (NDE) technology is being developed to advance the reliable application of ceramic materials to fossil energy systems for improved efficiency and better environmental control. NDE technology is evaluating and characterizing continuous fiber ceramic matrix composite (CFCC) materials such as SiC/SiC and Al_2O_2/Al_2O_3, with matrix infiltration by a variety of processes. NDE technology is being developed to provide data for quality assurance, process

development, and component lifetime prediction. CFCC materials are being developed for several applications in fossil energy systems. As an example, the development of improved hot-gas clean-up technology would have a significant impact on combined-cycle coal gasification, combined cycle pressurized fluidized bed combustion (PFBC), direct coal-fired gas turbines and coal gasification/fuel cell technology. Hot-gas filter applications require large numbers of components and thus NDE methods must be cost-effective. In addition the mechanical performance of CFCC materials have been shown to be strongly dependent on reinforcing fiber strength, fiber/matrix interface, and fiber architecture (fiber cloth lay-up sequence). The strength of the fibers and the fiber/matrix interface can become degraded in elevated temperature service environments. Such degradation is related to the generation of flaws and changes in the flaw morphology during processing and in service; if possible, these should be detected by NDE methods. Therefore, this research effort has continued to evaluate effects of fiber cloth lay-up sequence, fiber/matrix interface, and high-temperature environments on flaw generation and the resulting mechanical properties of reinforcing fibers and composites.

NDE CHARACTERIZATION OF AS-PROCESSED CFCC MATERIALS

X-ray computed tomographic imaging technology with high spatial resolution capability has been under development to evaluate CFCC materials for process development and "flaw" data for input to life-time prediction models.[1-4] The spatial resolution, speed of acquisition and part size that can be handled have been significantly improved to the point where many applications are now possible. Examples of results of applying this NDE method to several fiber architectures are given below.

a) 3-D Braided SiC/SiC with CVI Infiltration

As part of process development technology for CVI of 3-D braided SiC/SiC, MXCT has been shown to be capable of detecting delaminations, void distributions and areas of low infiltration density. Figure 1 shows a single transaxial X-ray CT image of a nominally 2 in. (50 μm) diameter tube being studied for process develop-ment. Note that voids < 100 μm can now be easily detected and, with image processing, porosity size distribution can be determined as a function of radial position. Such information is very helpful for process development and can be used to adjust infiltration parameters.

b) 2-D Laminated SiC/SiC and CVI Infiltration

X-ray CT imaging data has also been demonstrated to be capable of detecting delaminations and radially varying infiltration density in 2-D cloth lay-up SiC/SiC components infiltrated by isothermal CVI. Figure 2 shows three X-ray CT sections of a 50 mm diameter SiC/SiC tubular component fabricated by hand cloth layup and subsequently infiltrated by CVI. Note the detection of the cloth overlap region, the low density infiltration region near the inner surface and the detection of delaminated regions or laminar regions of poor infiltration. For heat-exchanger applications, such information may be necessary to predict component behavior.

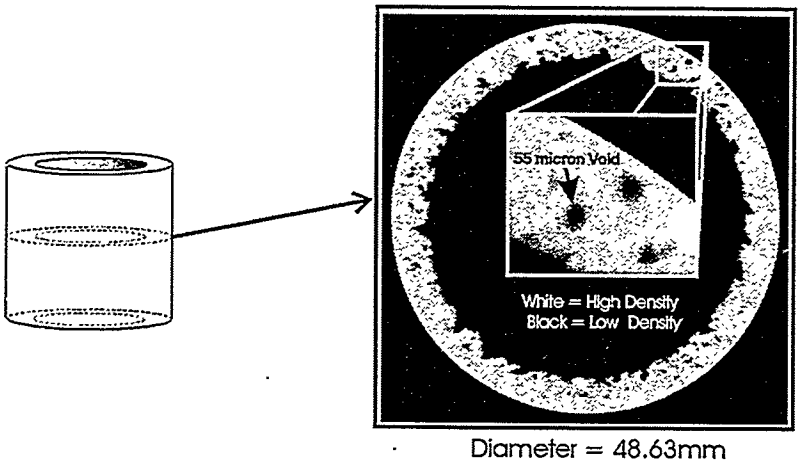

Fig. 1. Microfocus-based X-ray CT image of one section of a 50 mm diameter 3-D weave SiC/SiC infiltrated by CVI as part of infiltration process development.

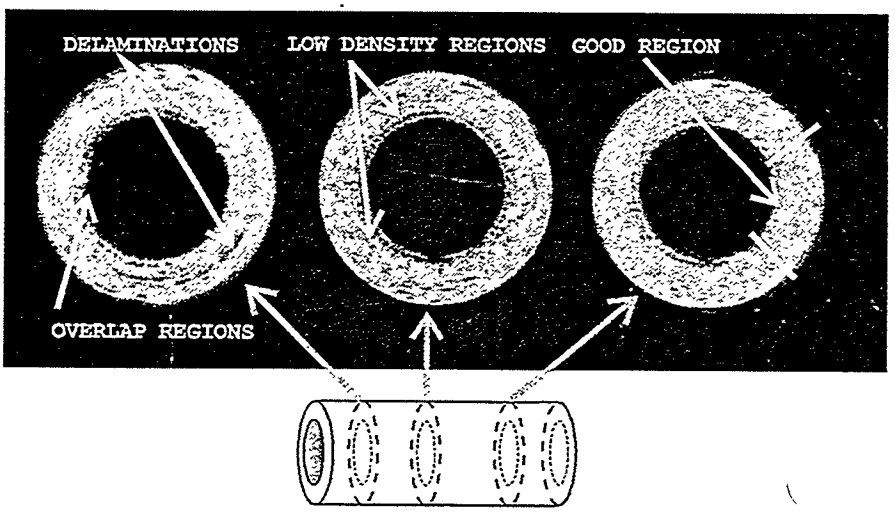

Fig. 2. Micro focused based X-ray CT images of 3 sections of a 50 mm diameter 2-D lay-up SiC/SiC CVI infiltrated tubular component.

c) 3-D Weave Oxide/Oxide Infiltrated by Sol-Gel Methods

X-ray CT imaging data have demonstrated the ability to detect fiber architecture and density variations in 20 cm diameter 3-D weave Sol-Gel infiltrated Al_2O_3/Al_2O_3 turbine engine combustor liners. Figure 3 shows a typical segment of an X-ray CT cross-section of a 3mm thick wall.

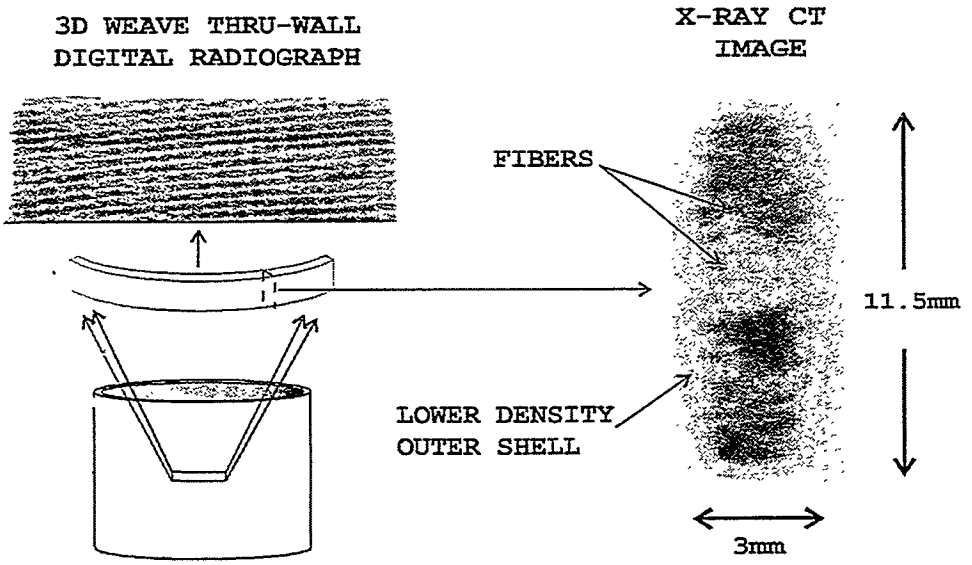

Fig. 3. X-ray computed tomographic images of a segment of a 20 cm diameter 3-D weave Al_2O_3/Al_2O_3 combustor liner infiltrated by Sol-Gel methods. (a) through-wall, X-ray digital radiograph, (b) high-resolution X-ray CT images.

d) Large Scale Component Inspection

The developed X-ray CT scanner technology now allows large components (>20cm) to be accommodated and thus provide high-spatial resolution image data.[2,3] Figure 4 shows a typical CT cross-section of a 20 cm diameter 3-D weave SiC/SiC turbine combustor liner. The image quality detail (spatial resolution) allows fiber architecture detection and large (>1 mm) regions of low infiltration. This information has been demonstrated to correlate with component performance prediction in turbine engine test rig tests.

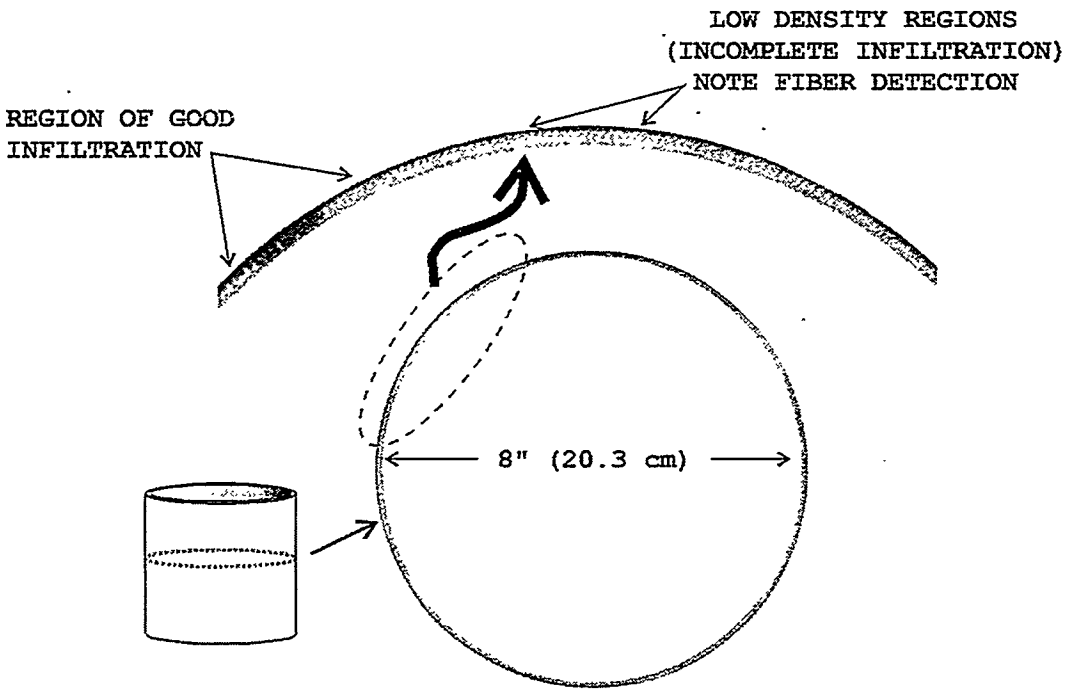

Fig. 4. Microfocus X-ray CT cross-section image of a 20 cm diameter 3-D weave SiC/SiC, CVI infiltrated turbine engine combustor liner showing regions of low-density infiltration and the ability of high resolution CT to detect fiber architecture within the 3 mm combustor liner wall.

FIBER/MATRIX INTERFACES: MEASUREMENT OF CHEMICAL COMPOSITION

Nuclear Magnetic Resonance Spectroscopy of Ceramic Composites

Experimental studies were conducted to examine the applicability of ^{11}B NMR spectroscopy for the determination of boron-doped carbon and BN coating microstructures on Nicalon fiber in SiC matrices. Specifically, experiments were initiated on a series of specimens provided by ORNL. The specimens were produced with 40 vol. % Nicalon plain-weave fabric rotated in the typical 0-30^{o} orientation, and with varying boron-to-carbon ratio and thickness of BN coatings in the doped and BN coated fibers, respectively. Initial experiments were performed to determine the overall sensitivity of the nucleus and various experimental parameters, including appropriate spinning speeds and pulse repetition rates.

To verify the utility of ^{11}B NMR spectroscopy, solid-state magic angle spinning (MAS) NMR experiments were performed on samples containing high concentrations of boron. ^{11}B NMR studies of the samples were performed at a magnetic field strength

of 7.1 T. Figure 5(a) shows NMR spectra of boric acid. It was shown that ^{11}B NMR analysis is capable of providing resolution and sensitivity exceeding the analytical requirements for quantitative measurements of boron in ceramic composites.

Experiments were also performed on a specimens containing BN-coated Nicalon fibers in SiC matrices to examine the applicability of ^{11}B NMR spectroscopy for the determination of boron-doped carbon and BN coating microstructures on Nicalon fibers in SiC matrices, as shown in Fig. 5(b). It was determined that the favorable spectroscopic properties (i.e., an isotopic natural abundance of approximately 80.5 %, a spin of 3/2 that provide efficient spin-lattice relaxation in the solid state, and an overall high relative receptivity approximately 13% of that of ^{1}H) of the ^{11}B nucleus provides significant sensitivity and allows accurate classification of the chemical environment of the boron. A new NMR and imaging system is now completely functional, and automated variable-temperature studies, and MAS 8 KHz will be performed to further understand the application of ^{11}B NMR spectroscopy for the determination of boron-doped carbon and BN coating microstructures on Nicalon fibers in SiC matrices.

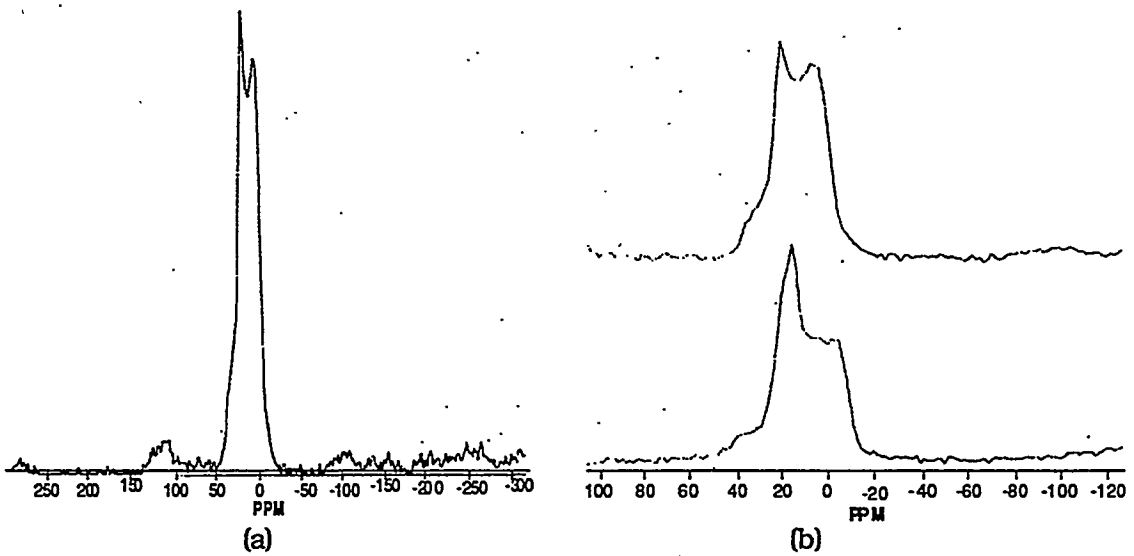

Fig. 5 (a) NMR spectra of boric acid. (b) ^{11}B NMR spectra of specimen containing BN-coated Nicalon fibers in SiC matrices.

EFFECTS OF FLAWS ON FRACTURE BEHAVIOR

To evaluate the effects of fiber cloth lay-up sequence and elevated-temperature service environments on flaw generation and resulting mechanical properties, Nicalon-fiber-reinforced SiC matrix composites (fabricated by CVI) with various cloth lay-up sequence and fiber coating thicknesses were obtained from Ceramic Composites, Inc., of Millerville, MD. To date, composites with fiber lay-up sequences of 0°/45° and 0°/20°/60° and carbon coating thickness of 0-0.4 μm have been evaluated. These composites were received in plate form, from which rectangular bars (≈3 x 4 x 40 mm) were machined. The tensile edges of the test bars were beveled to eliminate stress concentrations and thus avoid edge failures. Density of composites was measured by the Archimedes' principle. Approximately five specimens were tested per condition.

ROOM-TEMPERATURE MECHANICAL PROPERTY EVALUATIONS AND CORRELATIONS WITH FIBER ARCHITECTURE

Mechanical testing of 0°/45°, 0°/20°/60°, and 0°/40°/60° SiC/SiC composites was conducted in a four-point-bending mode on a universal testing machine at a loading rate of 1.27 mm/min. The loading and outer support spans were 20 mm and 40 mm, respectively. Both sets of specimens were observed to fail in a graceful manner, accompanied by extensive fiber pullout. The first matrix cracking stress was determined from the load at the first deviation from linearity on the load-displacement plot, whereas ultimate strength was measured from the peak load. Work-of-fracture was estimated from the area under the load-displacement plots. Room-temperature mechanical properties are shown in Table 1.

Table 1. Room-temperature mechanical-property data for SiC/SiC CFCCs with different fiber cloth lay-up sequences

Fiber Architecture	Coating Thickness (μm)	Composite Density (g/cm^3)	First Matrix Cracking Stress (MPa)	Ultimate Stress (MPa)	Work-of-Fracture (kJ/m^2)
0°/45°	0.0	-	-	105±28	0.16
	0.2	-	95.0	321±131	17.8±6
	0.4	2.25	86±23	153±41	9.8±2
0°/20°/60°	0.4	2.40	115±25	287±48	15.7±4
0°/40°/60°	0.4	2.46	116±28	312±28	14.4±4

As shown in the table, mechanical properties of composites are dependent on both fiber coating thickness and fiber cloth lay-up sequence. For a lay-up sequence of 0°/45°, mechanical properties (first matrix cracking stress, ultimate stress, and work of fracture) initially increase with coating thickness and reach peak values at a coating thickness of 0.2 μm. Further increases in coating thickness do not improve mechanical properties. This is believed to be related to the role of the coating in protecting fibers from damage during processing and in service.[7] These results indicate an optimal coating thickness of 0.2 μm for fibers in these composites. Similar results have been obtained for CVI SiC/SiC composites obtained from Oak Ridge National Laboratory.[7]

For a given fiber coating thickness, mechanical properties of composites with 0°/20°/60° and 0°/40°/60° fiber lay-up sequences were similar in magnitude, whereas composites with a fiber lay-up sequence of 0°/45° had relatively lower values. The decrease in mechanical properties for composites with a fiber lay-up sequence of 0°/45° is believed to have two causes. First, composites with a lay-up sequence of 0°/45° had a lower density (2.25 g/cm^3) than composites with other sequences (Table 1). The second cause could be the lower fiber fraction in the loading direction for composites with a 0°/45° fiber lay-up sequence as compared to composites with other fiber lay-up sequences.

These results provide much-needed information for optimizing composite processing in terms of fiber architecture and fiber coating thickness.

IN-SITU FIBER STRENGTH BEHAVIOR AND ITS CORRELATION WITH CRITICAL FLAWS

For evaluating the effects of fiber architecture and coating thickness on in-situ strength of fibers in composites, the fracture surfaces of composites with different fiber architectures and coating thicknesses (as shown in Table 1) were evaluated by standard fractography. Critical flaws in fibers (as shown in Fig. 6) were located and their sizes were measured. Subsequently, flaw sizes were correlated with fiber strength, as discussed below.

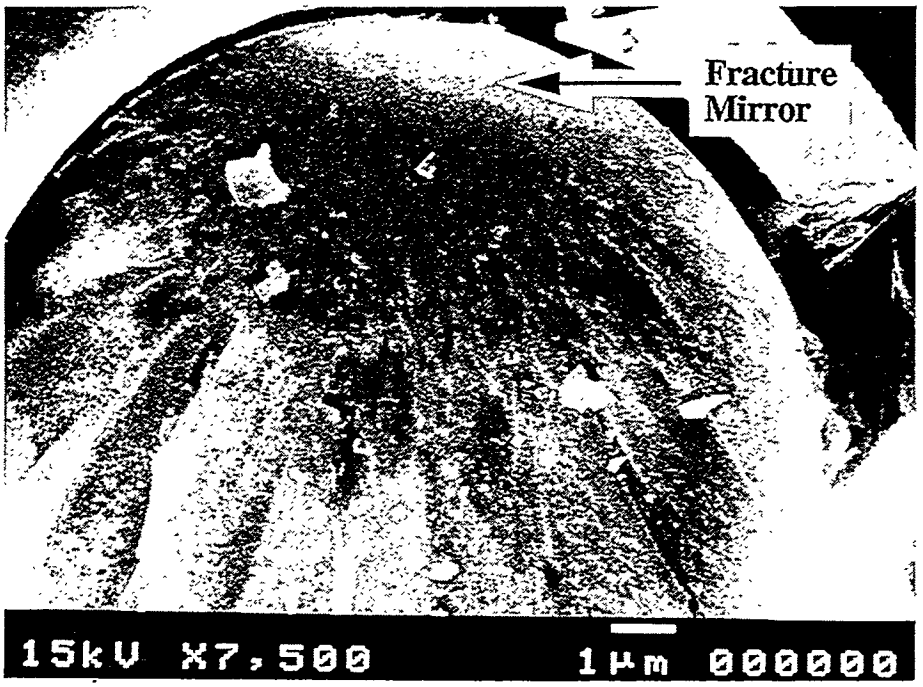

Fig. 6. Photomicrograph of fractured Nicalon fibers in SiC matrix composite, showing characteristic fracture features and fracture originating at fiber surface.

CRITICAL FLAW SIZE EVALUATIONS

In-situ strength of fibers in composites tested at room temperature as a function of fiber cloth lay-up sequence and coating thickness was evaluated from characteristic fracture features of the fibers. Strength of the fractured fibers was determined from the measured values of fracture mirror radii, as discussed by Kirchner and Gruver,[8] who provided the empirical relationship given in Equation 1.

$$\sigma_f \sqrt{r_m} = A_m , \tag{1}$$

where σ_f is the fiber fracture strength, r_m is the measured fiber mirror radius, and A_m is the mirror constant and is taken to be 3.5 MPa$\sqrt{m}$.

The measured values of in-situ fiber strengths were described by the Weibull strength distribution function, as shown in .

$$F(\sigma) = 1 - \exp\left[-\frac{L}{L_o}\left(\frac{\sigma}{\sigma_o}\right)^m\right], \tag{2}$$

where F(s) is the cumulative failure probability at an applied stress s, L_o is the fiber gage length at which Weibull parameters are estimated, L is the standard gage length taken to be 10 mm, s_o is the scale parameter signifying a characteristic strength of the distribution, and m is the Weibull modulus that characterizes the flaw distribution in the material.

Figure 7 compares the room-temperature in-situ fiber strength distributions of Nicalon fibers in composites with fiber lay-up sequences of 0°/45° and 0°/20°/60°. The figure also shows the effect of fiber coating thickness for composites with 0°/45° fiber lay-up. It can be clearly seen that for the same coating thickness of 0.4 μm, composites with a fiber lay-up sequence of 0°/45° have a higher (41%) in-situ fiber strength retained after processing than composites with 0°/20°/60° fiber lay-up sequence. In addition, for composites with 0°/45° fiber lay-up sequence, retained in-situ strength was higher (>100%) with a coating thickness of 0.4 μm. Further studies are in progress to optimize processing parameters for improved in-situ fiber strength.

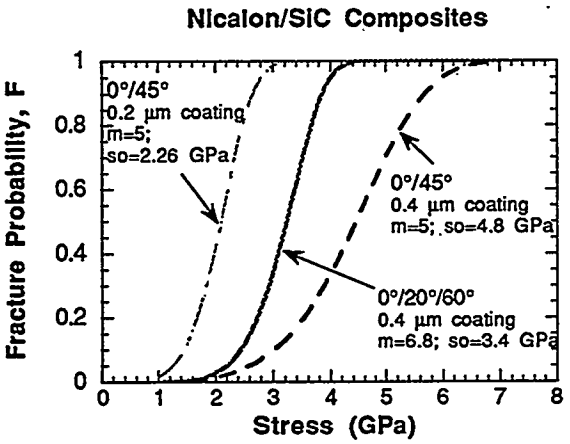

Fig. 7. Weibull strength distribution of Nicalon fibers in composites with different fiber lay-up sequences and coating thicknesses.

SUMMARY

Nondestructive evaluation (NDE) methods which can provide information about uniformity of material processing, e.g., axial and radial density, uniformity of fiber spacing, and the chemical state of the fiber matrix, have been demonstrated for applicability to several material systems. Distribution of void sizes of <100 μm can be

detected by high spatial resolution X-ray computed tomographic imaging on CFCC materials and density distribution can be determined. NMR has demonstrated the capability to measure the chemical state of fiber/matrix interfaces. Fracture behavior as a function of coating characteristics, fiber orientation, and flaw morphology show that coating thickness and fiber orientation are indeed affected by mechanical properties.

In the future, NDE technologies will be evaluated relative to joining applications of CFCC materials and for in-process data acquisition.

REFERENCES

1. E. A. Sivers, D. A. Holloway and W. A. Ellingson, "Predicting the Performance of 3-D X-ray Computerized Tomography Systems," in Nuc. Instr. and Meth. in Physics Research A, **345** (1994) pp. 179-197.

2. E. A. Sivers, D. A. Holloway, and W. A. Ellingson, "Use of Local X-ray Computerized Tomography for High-Resolution Region of Interest Inspection of Large Ceramic Components for Engines," ASME Int. Gas Turbine and Aero Engine Conf. May 1993, paper 93-GT-42, Cincidnnati, OH.

3. E. A. Sivers, W. A. Ellingson, S. A. Snyder, and D. A. Holloway," CT Multi-Scan Using Small Area Detectors to Image Large Dense Ceramic Components," to be presented to the ASME Int. Gas Turbine and Aeroengine Conf., June 1995, Houston, TX

4. P. Rizzo and W. A. Ellingson, "An Initial Comparison between Two 3-D X-ray CT Algorithms for Characterizing Ceramic Materials," in Conf. on NDE of Modern Ceramics, July 1990, Columbus, OH.

5. A. G. Evans and D. B. Marshall, "The Mechanical Behavior of Ceramic Matrix Composites," Overview No. 85, Acta Metall., **37** (10) 2567–2583 (1989).

6. T. Mah, M. G. Mendiratta, A. P. Katz, R. Ruh, and K. S. Mazdiyasni, "Room Temperature Mechanical Behavior of Fiber–Reinforced Ceramic Matrix Composites," J. Am. Ceram. Soc., **68** (1) C–27 – C–30 (1985).

7. J. P. Singh, D. Singh, and R. A. Lowden, "Effect of Fiber Coating on Mechanical Properties of Nicalon Fibers and Nicalon-Fiber/SiC Matrix Composites," Ceram. Eng. Sci. and Proc., **15** (4) 456–464 (1994).

8. H. P. Kirchner and R. M. Gruver, "Fracture Mirror in Alumina Ceramics," Phil. Mag. **27** 1433–1446 (1973).

FABRICATION OF FIBER-REINFORCED COMPOSITES BY CHEMICAL VAPOR INFILTRATION

W.M. Matlin*, D.P. Stinton**, and T. M. Besmann**
*Department of Materials Science and Engineering, University of Tennessee
Knoxville, TN 37996-2200

**Oak Ridge National Laboratory, Oak Ridge, TN 37831

ABSTRACT

A two-step forced chemical vapor infiltration process was developed that reduced infiltration times for 4.45 cm dia. by 1.27 cm thick Nicalon+ fiber preforms by two thirds while maintaining final densities near 90 %. In the first stage of the process, micro-voids within fiber bundles in the cloth were uniformly infiltrated throughout the preform. In the second stage, the deposition rate was increased to more rapidly fill the macro-voids between bundles within the cloth and between layers of cloth. By varying the thermal gradient across the preform uniform infiltration rates were maintained and high final densities achieved.

INTRODUCTION

Due to their high temperature strength and damage tolerant behavior, fiber reinforced ceramic matrix composites produced by chemical vapor infiltration are candidate materials for a number of high temperature applications. However, major obstacles in the commercialization of these materials are posed by the materials' high cost and the difficulty in fabricating thick components. In an attempt to reduce this cost and enable fabrication of thicker components, Oak Ridge National Laboratory has developed forced chemical vapor infiltration (FCVI) [1].

In spite of the significant advantages of FCVI, the composites produced may still be too expensive to be commercially viable. Furnace operation during preform infiltration make up the largest fraction of the composite's cost [2]. Therefore, reducing the time to infiltrate the preforms would have the greatest impact on the economics of the process.

Sheldon [3] has approached optimization of the isothermal, isobaric chemical vapor infiltration (ICVI) process by dividing the process into two steps. In the first step, intrabundle infiltration would be optimized [3]. In the second step, the much larger interbundle voids would be more efficiently filled [4]. Since the

+ Nippon Carbon Company, Tokyo, Japan

transport phenomena for ICVI,diffusion, is different than for FCVI, forced convection, the conclusions from this work could not be directly applied to FCVI optimization. However, the general two-step approach should be applicable.

In previous experimental FCVI optimization efforts, reductions in processing time have always corresponded to reductions in final density [5]. If this trend was to be reversed a better understanding of time dependent relationship between process variables would be required. The Georgia Tech. Chemical Vapor Infiltration Model (GTCVI) [6], a three dimensional finite volume program for modeling chemical vapor infiltration processes, was used to gain a phenomenological understanding of the process and as a guide in identifying the relative importance of each of the involved variables.

Several sets of modeling runs were performed to identify the optimum conditions for a two step process to infiltrate a 4.45 cm dia. by 1.27 cm thick preform, comprised of 52 layers of Nicalon cloth, with SiC deposited from CH_3SiCl_3 in hydrogen. The object of these runs was to develop a first step optimized to fill the micro-voids within the fiber bundles, and a second step optimized to fill the macro-voids between bundles in the cloth and between layers of fabric. This process scheme should result in much shorter infiltration times.

FIRST STAGE MODELING

A set of modeling runs was performed to identify conditions that resulted in uniform bundle infiltration from the hot side to the cool side of the preform. Six modeling runs were preformed by varying the initial cool side temperatures from 750 °C to 1000 °C at 50 °C increments. The hot-side of the control volume was fixed at 1200 °C and 100 kPa. The cool-side of the control volume was set to 750 °C, total flow of 550 cm^3/min, and a CH_3SiCl_3 flow of 45 cm^3/min. A time increment of 30 minutes was used between iterations and the runs were terminated after 8 simulated hours of infiltration. Density, deposition rates, temperature, pressure, CH_3SiCl_3 concentration, product HCl concentration and gas flow values were saved for each of the time increments.

The 750 °C cool side temperature run resulted in rapid deposition on the hot face with little or no deposition on the cool face. After 8 hours the cool-side of the preform has barely started to infiltrate, while the hot side was well past the point where bundles are fully infiltrated. Increasing the cool side temperature increased the deposition rate there. Since more reactant was consumed and HCl etchant produced on the cool side of the preform, the concentration of reactant on the hot-side decreased, resulting in lower deposition rates. At a cool-side temperature of approximately 950 °C the temperature gradient offsets the depletion of the reactant and uniform deposition results. Above 950 °C the density gradient is reversed with higher densities occurring near the cool-side and lower densities occurring near the hot-side.

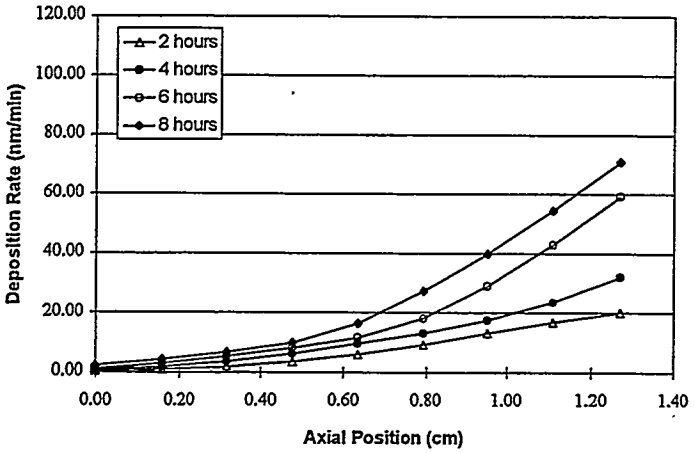

Figure 1. Deposition rate vs. axial position for 750 °C cool-side GTCVI simulation.

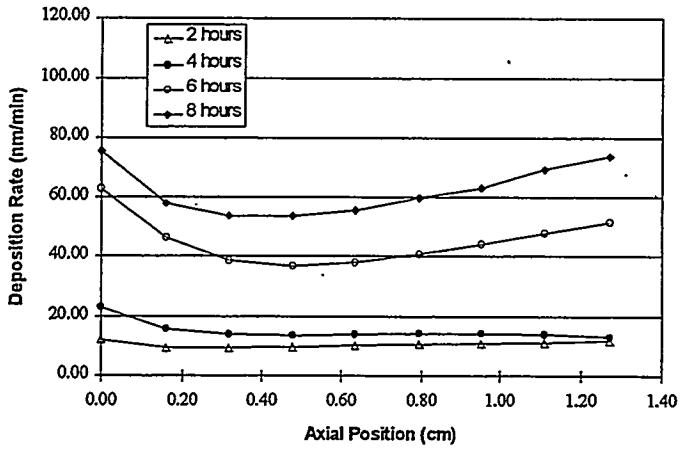

Figure 2. Deposition rate vs. axial position for 950 °C cool-side GTCVI simulation.

SECOND STAGE MODELING

Process conditions to more rapidly fill the macro voids between bundles and layers in the preforms were then investigated by using a response surface experimental design. The goal of this investigation was to optimize the process conditions to rapidly fill the large voids between bundles. In this design the top temperature was fixed at 1200 °C; higher temperatures were not investigated because they would result in damage to the Nicalon fiber. The thermal gradient, H_2 gas flow, CH_3SiCl_3 molar ratio and outlet pressure were varied using a central composite design with 16 cube points and 8 star points. A center point of 1200 °C top temperature, 545 cm^3/min total flow, 0.0827 CH_3SiCl_3 molar ratio (CH_3SiCl_3 moles/total gas moles), and 100 kPa outlet pressure was used. Intervals of 100 °C, 100 cm^3/min total flow, 0.025 CH_3SiCl_3 molar ratio, and 25 kPa

were used to generate the cube and star conditions. Infiltration at each of these conditions was then simulated using GTCVI, as shown in Table 1.

The interrelationship between and relative importance of the process variables on times and density was then determined by fitting first order response surfaces from the data points in Table 1. Density and process time were determined to be much more sensitive to temperature variations than other variables. Pressure was the next variable of importance due to the fact that increasing the inlet pressure while maintaining a shutdown inlet pressure of 200 kPa resulted in lower allowable pressure drops across the preform; thus, lower final densities. Density and process time had similar sensitivities to total gas flow and CH_3SiCl_3 concentration.

Additionally, increases in temperature, pressure, and gas flow rates reduced processing times and lowered final densities. In contrast, increases in concentration tended to both lower processing time and increase final density (Figs. 3 and 4).

Table 1. Response Surface Points used in the GTCVI model for second stage infiltration.

File Name	Response Surface Intervals				Temp. (°C)	Pressure (kPa)	H_2 (cm^3/min)	CH_3SiCl_3 (cm^3/min)	Time (h)	Density (%)
tst401	-1	-1	-1	-1	1100	75	420	25.75	29	88.1
tst402	1	-1	-1	-1	1300	75	420	25.75	9	87
tst403	-1	1	-1	-1	1100	125	420	25.75	24.5	85.7
tst404	1	1	-1	-1	1300	125	420	25.75	7.5	84.2
tst405	-1	-1	1	-1	1100	75	580	35.5	22.5	86.7
tst406	1	-1	1	-1	1300	75	580	35.5	6.5	85.1
tst407	-1	1	1	-1	1100	125	580	35.5	17	82.9
tst408	1	1	1	-1	1300	125	580	35.5	6	82.9
tst409	-1	-1	-1	-1	1100	75	420	25.75	24	88.5
tst410	1	-1	-1	1	1300	75	420	50.7	7	87.9
tst411	-1	1	-1	1	1100	125	420	50.7	11	87.9
tst412	1	1	-1	1	1300	125	420	50.7	5.5	84.4
tst413	-1	-1	1	1	1100	75	580	70	18	86.6
tst414	1	-1	1	1	1300	75	580	70	5.5	87
tst415	-1	1	1	1	1100	125	580	70	14.5	83.8
tst416	1	1	1	1	1300	125	580	70	4	82.3
tst417	0	0	0	0	1200	100	500	45	10.5	85.9
tst418	0	0	0	0	1200	100	500	45	10.5	85.9
tst419	-2	0	0	0	1000	100	500	45	56.5	87
tst420	2	0	0	0	1400	100	500	45	4.5	84.9
tst421	0	-2	0	0	1200	50	500	45	12.5	88.2
tst422	0	2	0	0	1200	150	500	45	8	82.1
tst423	0	0	-2	0	1200	100	340	30.5	15	88
tst424	0	0	2	0	1200	100	660	59.5	8	84
tst425	0	0	0	-2	1200	100	500	17	19	86.4
tst426	0	0	0	2	1200	100	500	76.5	8.5	86.6
tst427	0	0	0	0	1200	100	500	45	10.5	85.9

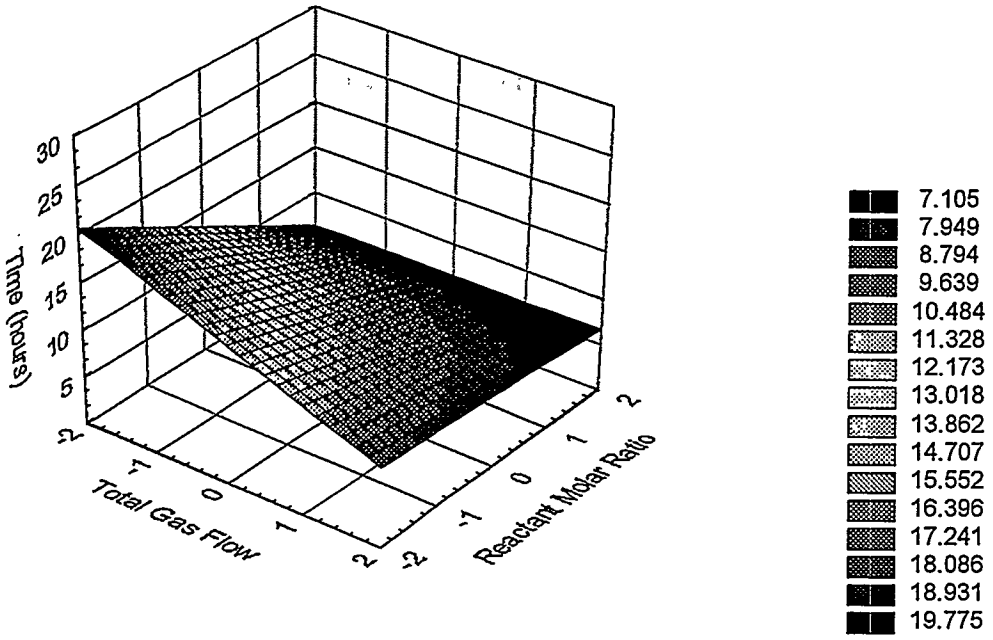

Figure 3. Time, flow, and concentration response surface generated from the GTCVI model data for the second phase of the two-step process.

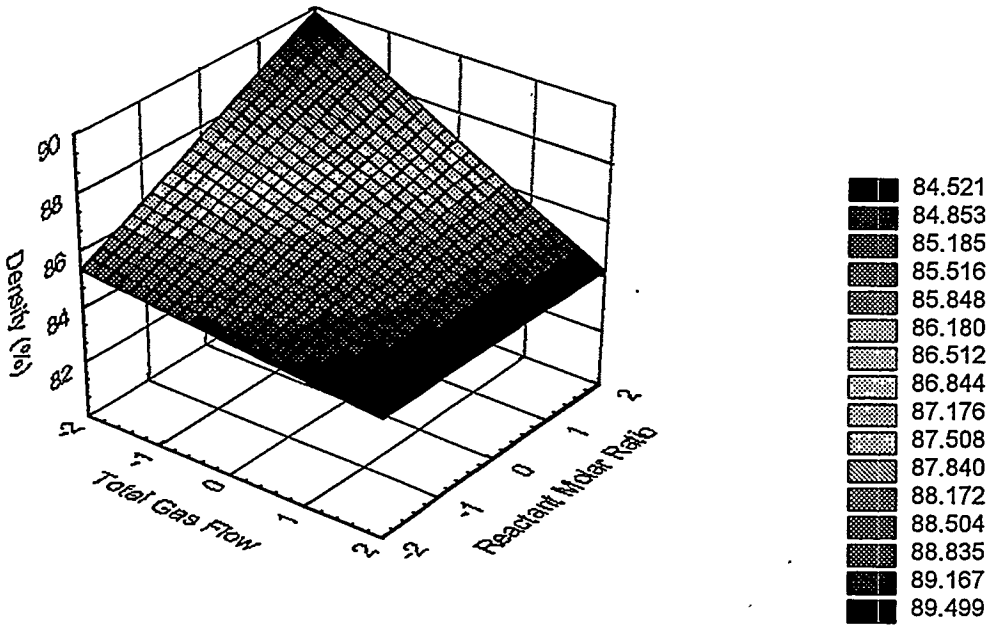

Figure 4. Density, flow, and concentration response surface generated from the GTCVI model data for the second phase of the two-step process.

TWO STEP MODELING

A two-step process, consisting of the optimized conditions from each of the stages previously described, was modeled and compared to the original one-step process. In the first set of computations, one-step conditions were used: 1200 °C hot-side temperature, 750 °C cool-side temperature, 500 cm^3/min H_2, 45 cm^3/min CH_3SiCl_3. The simulation ran until the pressure drop across the preform reached 100 kPa. The second run combined the thermal gradient optimization of the first stage with the increased CH_3SiCl_3 concentration of the second stage. The first five hours of the run used a 1200 °C hot-side temperature, 950 °C initial cool-side temperature, 500 cm^3/min H_2, and 45 cm^3/min CH_3SiCl_3. After the first five hours, the cool-side temperature was decreased to 850 °C and the CH_3SiCl_3 was increased from 45 cm^3/min to 83 cm^3/min. This simulation ran until a back-pressure of 100 kPa was reached.

The two-step simulation predicted a processing time 25 % shorter than the one-step process, with more uniform final density (Figs. 5 and 6).

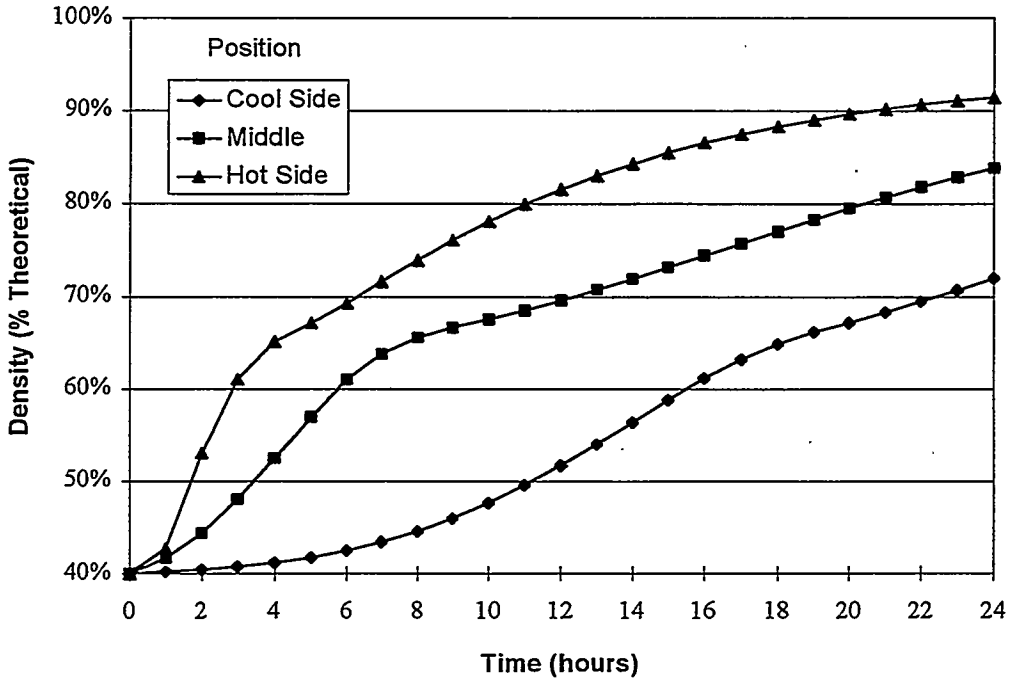

Figure 5. Density vs. time for 750 °C cool-side, one-step GTCVI simulation.

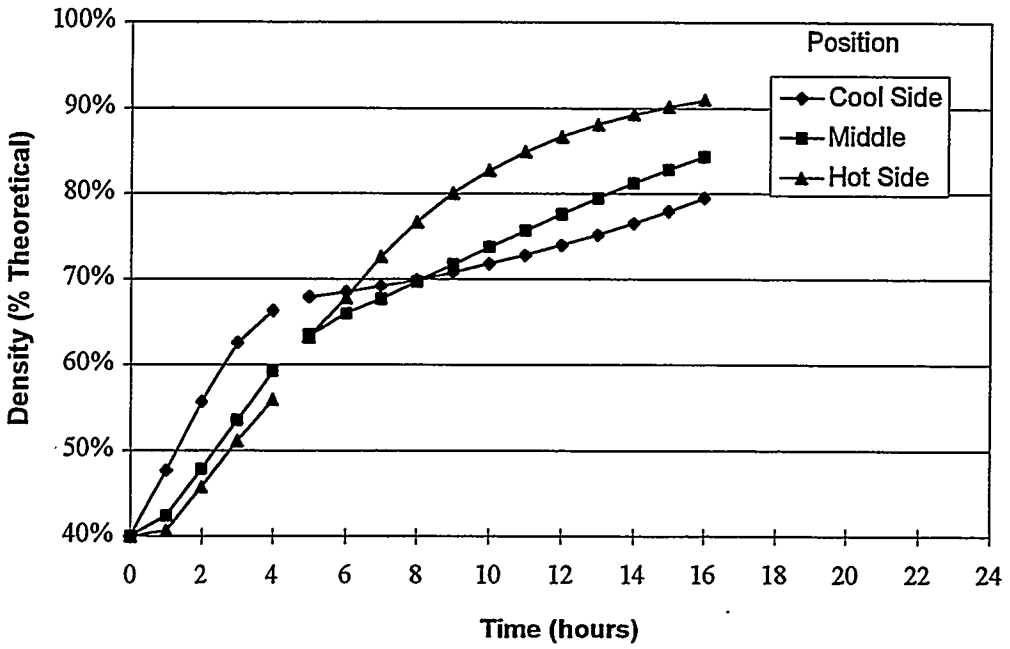

Figure 6. Density vs. time for 950 °C cool-side, two-step GTCVI simulation.

EXPERIMENTAL VERIFICATION

Two experimental runs were preformed and compared to the model predictions. In the first run (907) the preform was infiltrated for five hours using a 1200 °C hot-side temperature, 920 °C cool-side temperature, 500 cm^3/min H_2, and 45 cm^3/min CH_3SiCl_3. Process conditions were then changed to 1200 °C hot-side temperature, 825 °C cool-side temperature, 500 cm^3/min H_2, and 83 cm^3/min CH_3SiCl_3. The process automatically shutdown when a back-pressure of 170 kPa was reached.

The second preform (906) was infiltrated using standard conditions, i.e., 1200 °C hot-side temperature, 750 °C cool-side temperature, 500 cm^3/min H_2, and 45 cm^3/min CH_3SiCl_3. The process, again, automatically shutdown when a back-pressure of 170 kPa was reached.

The two step process required ten hours for infiltration and displayed a relatively uniform density averaging 89.8% (Table 2). In contrast, the run using standard conditions took 4.4 hours longer and had an average density 6.6% lower (Table 2). Additionally, the density gradients were significantly larger. Image analysis of the specimens was used to characterize the relative percentage of micro-porosity and macro-porosity. The sample fabricated using standard conditions had a total porosity of 15.4%, consisting of 8.7% macro porosity and 6.8% micro porosity (Table 3). The sample fabricated using the two-step process

had a total porosity of 14.5%, consisting of 9.4% macro porosity, and 5.1% micro porosity (Table 3).

Table 2. Experimental verification runs.

Process Number	Process Time (h)	Cool side Temp. (°C)	CH_3SiCl_3 Flow (cm^3/min)	Density (% Theoretical) Radial Position				
				Center				Edge
One-Step (906)	14.4	750	45	Hot side	89.8	89.7	89.5	88.9	86.6
				Middle	80.6	87.3	86.8	84.1	84.4
				Cool side	75.1	75.6	75.9	77	77.1
Two-Step (907)	5 + 5 = 10	920 + 750	45 + 83	Hot side	90.4	92.7	92	94.1	93.2
				Middle	92.8	92.2	92.5	92	91.6
				Cool side	85.6	86.2	86.3	85	80.9

Table 3. Porosity measurements using optical image analysis.

	One-Step (906)			Two-Step (907)		
	Macro Porosity	Micro Porosity	Total Porosity	Macro Porosity	Micro Porosity	Total Porosity
Hot Side	9.4%	6.7%	16.2%	15.5%	5.2%	20.7%
	6.7%	6.9%	13.7%	5.3%	5.3%	10.6%
	4.7%	7.1%	11.8%	5.6%	5.3%	10.9%
	5.4%	7.0%	12.5%	4.7%	5.3%	10.1%
	11.0%	6.6%	17.6%	8.2%	5.1%	13.3%
	7.4%	6.9%	14.3%	9.0%	5.1%	14.1%
	9.4%	6.7%	16.1%	12.1%	4.9%	17.0%
Cool Side	15.1%	6.3%	21.4%	14.6%	4.8%	19.4%
Average	8.7%	6.8%	15.4%	9.4%	5.1%	14.5%

SUMMARY

The two-step process significantly reduced processing time without reducing final density or uniformity. The key to this success was focusing on maintaining uniform infiltration rates, which prevent density gradients from forming within the preform. Gradients are caused by closure of macro-voids within one section of the preform while other sections remain relatively porous.

The utility of the GTCVI model was also demonstrated. Based on the accuracy of the GTCVI simulations for the 4.45 cm diameter furnace, GTCVI is expected to be instrumental in developing similarly optimized processing conditions for larger-scale furnaces [7].

REFERENCES

1. T. M. Besmann, B. W. Sheldon, R. A. Lowden, and D. P. Stinton, "Vapor phase fabrication and properties of continuous-filament ceramic composites", Science, Vol. 253, pp 1104-9 (1991).

2. Y.G. Roman, D. P. Stinton, "The preparation and economics of Silicon Carbide matrix composites by chemical vapor infiltration"; in Symposium Proceedings, Ceramic Matrix Composites (Boston, MA, 1994). Edited by R.L Lowden and J. R. Hellman, Materials Research Society, Pittsburg, PA, 1994 (in press).

3. H.C. Chang, T.F. Morse, B.W.Sheldon, "Minimizing infiltration times during the initial stage of isothermal chemical vapor infiltration", Journal of Materials Processing & Manufacturing Science, Vol. 2, pp 437-455 (1994).

4. B.W. Sheldon, H.C. Chang, "Minimizing densification times during the final stage of isothermal chemical vapor infiltration", Silicon-Based Structural Ceramics, B.W. Sheldon, S.C. Danforth (eds.), Ceramic Transactions, Vol. 42, American Ceramic Society, (1994).

5. R.A. Lowden, A.J. Caputo, D.P. Stinton, T.M. Besmann, and M.D. Morris, "Effect of infiltration conditions on the properties of SiC/Nicalon composites", Oak Ridge National Laboratory Report ORNL/TM-10403, (1987).

6. T.L. Starr, "Model for rapid CVI of ceramic composites" Proc. 10th Int. Conf. CVD, (The Electrochemical Society, Inc., Pennington, NJ, 1987), pp 1147-1155, (1987).

7. D. P. Stinton, O.J. Schwarz, and J. C. McLaughlin, "Fabrication of fiber-reinforced composites by chemical vapor infiltration", Proceedings of the Eight Annual Conference on Fossil Energy Materials, Oak Ridge National Laboratory Report ORNL/FMP-94/1, pp 1-9, (1994).

TRANSPORT PROPERTIES OF CERAMIC COMPOSITES

T.L. Starr

School of Materials Science and Engineering
Georgia Institute of Technology
Atlanta, Georgia 30332-0245

This project involves experimental and modeling investigation of the transport properties of chemical vapor infiltration (CVI) preforms and densified composites, with particular emphasis on gas permeability and mass diffusivity. The results of this work will be useful both for on-going CVI process development and for evaluation and optimization of composite materials for fossil energy applications.

With preforms made with 500 filaments/tow Nicalon at 40 vol% fiber loading, permeability values are similar for square-weave cloth layup and 3-D weave at low density. At greater densification the 3-D weave permeability is lower and approaches zero with significantly more closed porosity than the cloth layup. For filament wound preforms we were unable to make reliable measurements with the available materials.

A model for gas transport in these materials utilizes percolation theory concepts. The ultimate achievable density is related to the closing of a continuous gas path through the preform. As the density approaches this limit the gas permeability and diffusivity vanish exponentially. The value of this limit is controlled primarily by the preform fiber architecture. The observed difference between the cloth layup and 3-D weave materials is due to the larger pores at tow crossing points found in the 3-D weave.

INTRODUCTION

Of the various methods for fabricating ceramic matrix composites, chemical vapor infiltration (CVI) is strongly controlled by the transport properties of the preform and partially densified composite. These properties include gas permeability, mass diffusivity (effective diffusion coefficient) and thermal conductivity, and depend on the density and microstructure of the composite. For forced flow CVI, the gas permeability is the critical factor that determines the ultimate density that can be achieved. Mass diffusivity is a controlling property for isothermal CVI where it limits the densification rate and

density uniformity. For thermal gradient CVI the thermal conductivity of the composite controls the steepness of the thermal gradient and how this gradient changes with processing time.

This paper describes our ongoing investigation of the gas permeability of CVI preforms and densified composites, involving both experiment and modeling. The results of this work will be used both for CVI process development and for evaluation and optimization of composite materials for fossil energy applications.

GAS PERMEABILITY MEASUREMENTS

Our experimental apparatus for measuring gas permeability is shown schematically in Figure 1. Measurement consists of concurrent determination of gas flow rate and pressure difference across the specimen. While simple in principle accurate measurements with small specimens at low permeability require careful attention to detail. In particular we have added a second, downstream flowmeter to the apparatus to ensure there are no leaks in the gas lines and in the specimen mounting fixture.

A critical factor in these measurements is extraction and mounting of the test specimen. It must be large enough to encompass a number of unit cells of the composite architecture, but small enough to have uniform density throughout. Earlier measurements used very small, cube shaped specimens[1]. For recent measurements we have used two types of larger specimens.

One type of permeability specimen has the form of a right circular cylinder approximately 10 mm in diameter and 5-10 mm in length and is machined from a larger piece of composite. Recent results for composites made with 40 vol% Nicalon fiber are shown in Figure 2. Permeability values for 3-D weave and cloth layup materials are similar at low density, however, at high density the 3-D weave permeability is lower and approaches zero with significantly more closed porosity than the cloth layup. These results are analyzed below in the discussion of transport property modeling. Sections of filament wound composite also

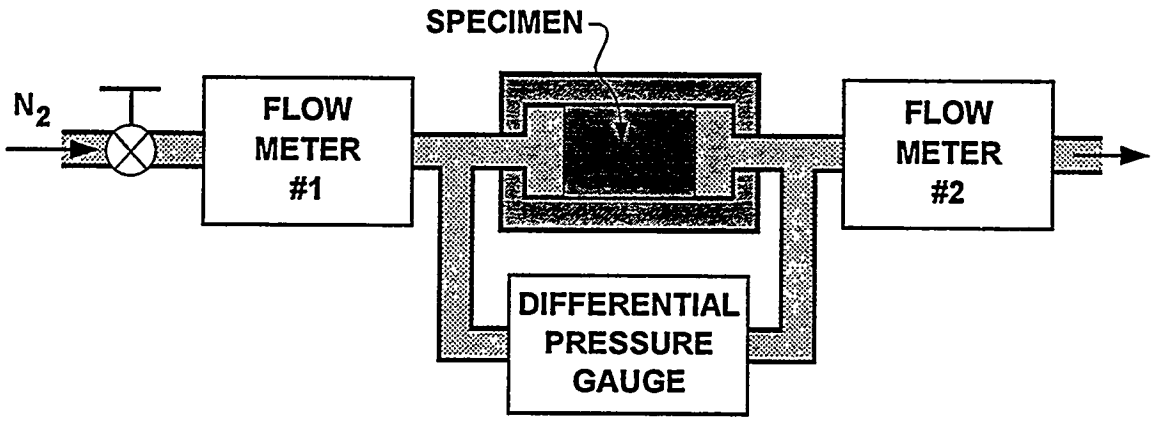

Figure 1. Apparatus for performing gas permeability measurements. Downstream meter provides redundant flow measurement as check for gas leaks in mounting fixture.

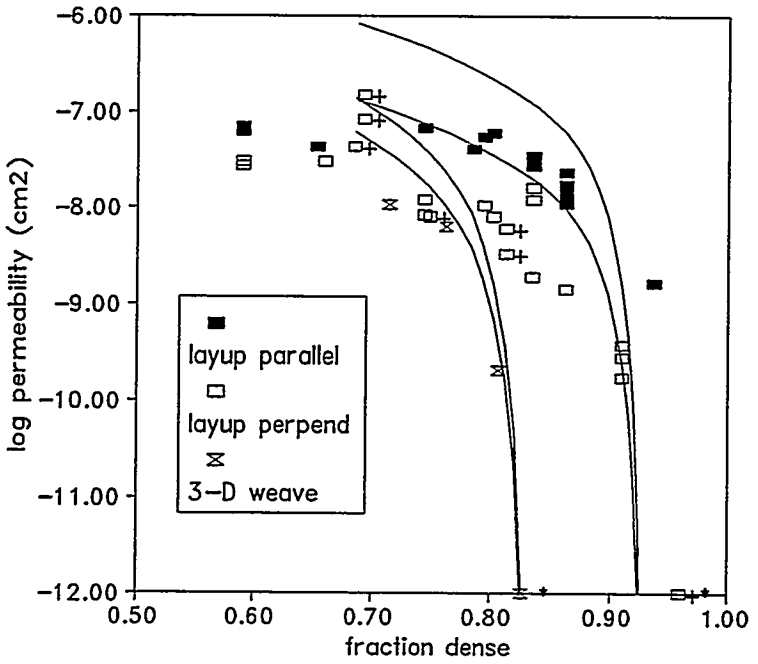

Figure 2. Gas permeability for cloth layup and 3D weave composites. Layup points with + are recent measurements. Points with * had no measurable permeability. Solid lines are model calculations discussed in text.

were available but due to their size and configuration we were unable to machine specimens suitable for reliable measurements.

An additional type of specimen is fabricated using a small, forced flow CVI apparatus, providing specimens 18 mm in diameter and up to 20 mm thick. This approach has the advantages that it allows us to measure permeability prior to densification and at different densities, and to fabricate various layup patterns. Permeability measurements with these specimens have not been completed at this time.

TRANSPORT PROPERTY MODEL

A general model has been proposed for the microstructure and gas permeability of woven fiber preforms and composites based on a node-bond model[2]. In this model the porosity is represented as a network of spherical "nodes" connected by cylindrical "bonds" (Figure 3). The network geometry is directly related to the regular structure of the woven preform. Nodes correspond to the large pores created at tow crossing points while bonds correspond to the smaller channels that connect neighboring nodes. The spatial arrangement of the nodes and their coordination number (number of nearest neighbors) is fixed by the weave architecture i.e. tow spacing and weave or braid pattern. The node and bond diameters exhibit a distribution of values around an average which is set to match the overall volume fraction of intertow porosity.

The gas permeability of this network is calculated assuming Poiseuille flow through the cylindrical bonds with the given distribution of diameters. Densification is simulated by incrementally reducing the bond and node dimensions and recalculating the network pore volume, surface area and permeability. As densification proceeds the smaller bonds close (Figure 4) and as the fraction of open bonds approaches the percolation limit the accessable pore fraction and the network permeability both vanish exponentially.

The model can be used to estimate the surface area and permeability of woven fiber preforms during CVI. A commonly used

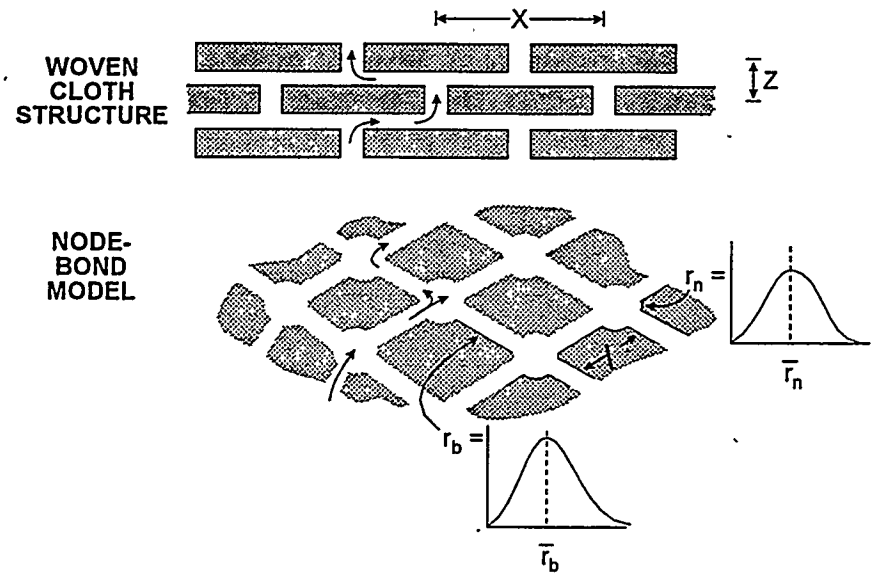

Figure 3. Node-bond model for gas transport through woven fiber preform relates to fiber architecture.

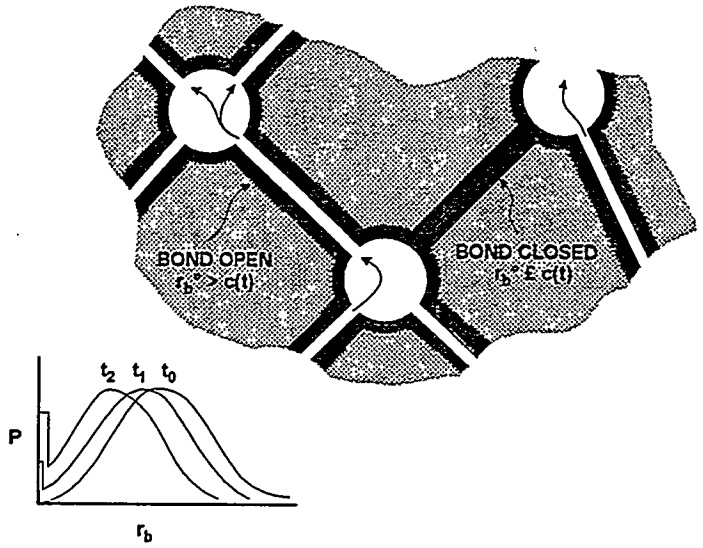

Figure 4. During densification bonds close at different times until no continuous gas path remains.

preform consists of several layers of square-weave cloth stacked to give 40% fiber by volume. A typical preform uses tows of 15 μm fibers with 500 filaments/tow, tow spacing of 0.150 cm in the cloth (X and Y directions) and a layer spacing of 0.030 cm. The 60% porosity in the preform is considered to be divided equally between fine porosity within the tows and coarse porosity between the tows. The coarse porosity consists of relatively large pores (nodes) in the plane of the cloth and smaller, tortuous pores (bonds) connecting these to eight similar nodes in adjoining cloth layers. A critical parameter in this model is the ratio of the node and bond radii, r_n/r_b. Model estimate of permeability is shown as the upper pair of curves in Figure 2 for $r_n/r_b = 3.0$. The match to experiment is reasonably good although the model values are systematically high.

Microscopic examination of the 3-D weave composite used for permeability measurements shows a tow spacing in two directions of 0.150 cm but only 0.100 cm in the third direction. This anisotropy is expected to yield a somewhat anisotropic permeability. However, all experimental measurements were made parallel to the small spacing direction. Also, compared to the cloth layup composite, the "nodes" constitute a larger fraction of the intertow porosity. Using these observations the model yields the lower pair of curves in Figure 2 for $r_n/r_b = 6.0$. Again, the match with experiment is reasonably good with a percolation limit significantly lower than that of the cloth layup. From the model we can see that this results from the relatively large pores found at the crossing points of the three orthogonal yarns.

SUMMARY

This experimental investigation of the transport properties of CVI preforms and densified composites aims to produce consistent data useful both for on-going CVI process development and for evaluation and optimization of composite materials for fossil energy applications. The ultimate goal is to understand the microstructure-transport property

relationship well enough to design fiber architectures for optimum processing behavior.

The node-bond percolation model for gas transport builds on a representation of the coarse porosity in woven fiber structures during CVI densification. While this structure is idealized, model parameters relate to real structural features such as filament size, number of fibers per tow and spacing of tows in the weave. Some uncertainty exists in the proper partition of the porosity between "node" and "bond" and between intra-tow and inter-tow, although the total is constrained by the known fiber loading.

Applied to cloth layup and 3-D weave preforms the model gives reasonably good agreement with experimental measurements although model predictions are systematically high. The observed higher amount of closed porosity for the 3-D weave is due to a larger fraction of intertow porosity deriving from the large pores at tow crossing points.

REFERENCES

1. G.B. Freeman, T.L. Starr and T.C. Elston, "Transport Properties of CVI Preforms and Composites," Mat. Res. Soc. Symp. Proc. 168, 49-54 (1990).

2. T.L. Starr, "Gas Transport Model for Chemical Vapor Infiltration," J. Mat. Sci., in press.

DEVELOPMENT OF MATERIALS FOR MICROWAVE-HEATED DIESEL PARTICULATE FILTER

Mark A. Janney and David P. Stinton
Oak Ridge National Laboratory
Oak Ridge, Tennessee 37831-6087

ABSTRACT

Ceramic fiber filters are being fabricated and tested for use as diesel particulate filters. The filters are to be heated by microwave energy to remove carbon and regenerate the filters.

INTRODUCTION

The purpose of this research is to help develop microwave-heated diesel engine particulate filter/burner devices. The goal is to develop materials that will perform both as filter and heater in such a device. A Cooperative Research and Development Agreement (CRADA No. ORNL93-0172) between Martin Marietta Energy Systems (MMES) and the Cummins Engine Company is in place that supports this work. The Department of Energy (DOE) CRADA monies come from both the Fossil Energy AR&TD Materials Program and the Energy Efficiency and Renewable Energy - Office of Transportation Technologies (EE-OTT), Heavy Duty Transport Program.

Diesel engines will soon be required (1998) to emit essentially no particulate exhaust into the environment. One of the approaches to prevent such emissions is to trap the particles in a filter, then burn the trapped particles on a regular cycle. An approach that has been proposed by Cummins Engine Co. is to build a system based on a ceramic filter that can be heated with microwaves. We will fabricate such filters

and determine how they interact with microwaves to heat and burn the carbon particulates trapped in the filter material.

We propose to develop a ceramic composite structure of SiC-coated ceramic fiber that can be used as a diesel engine particulate filter. For commercial usage a particulate filter must: 1) filter carbon particles from high temperature diesel exhaust gas at an acceptable (low) backpressure; 2) survive thousands of thermal transients caused by regeneration (cleaning) of the filter by oxidizing the collected carbon; (3) be durable and reliable over the life of the filter, which is in excess of 300,000 miles (10,000 hours of operation); and, (4) provide a low overall operating cost which is competitive with other filtering techniques.

SiC-coated ceramic fiber was selected as the filter material because it can be readily heated by microwave energy. Particulate traps must be regenerated by heating the carbon particles to approximately 600°C to oxidize the carbon. Heating by microwaves is expected to provide more uniform heating of the filter and result in a lower cost, more reliable regeneration system. Previous methods of regeneration used diesel-fired burners or electrical resistance heating for regeneration. Uneven heating and use of weak ceramic materials resulted in cracking of the trap and loss of filtration capability. Fiber composites have excellent thermal shock capability. Producing a filter by manufacturing a fiber-reinforced ceramic paper has inherent advantages since it is possible to tailor the filtration characteristics of the ceramic paper while maintaining a strain tolerant material.

The idea of using microwave heating combined with ceramic filters to trap and burn carbon particulate emissions from

diesel engines represents a large-scale, near term consumer and industrial application of two technologies, microwave heating and chemical vapor infiltration, developed under the AR&TD materials program. As such, it has the potential to be an excellent example of technology transfer and cooperative research and development between a national laboratory and U.S. industry. This approach represents the front runner in the thinking of one of the nation's foremost diesel manufacturers.

TECHNICAL PROGRESS

We are investigating the development of materials for diesel particulate filters. We have devoted our efforts to evaluating various candidate materials concerning: (1) how well they can be fabricated into filter elements; (2) how they interact with a microwave field - i.e., how they heat;; and, (3) how well they withstand a corrosive (oxidative) high temperature environment.

CVD Coating

Filter papers made from ceramic fibers were received from Fleetguard, a division of Cummins Engine Company. These papers were coated at ORNL with CVI SiC containing various levels of additives. It had been observed last year that CVD conditions that should have produced high-quality, stoichiometric SiC coatings instead produced poor coatings. It was hypothesized that excess carbon had formed in the filter papers during pyrolysis of the organic constituents used in the papermaking process. Excess silicon was added to some of the CVI runs to compensate for the residual carbon. Figure 1 shows micro-structures of the CVD-coated papers made under stoichiometric and excess silicon CVD conditions. Clearly, the coating made

with excess silicon is superior to that made under stoichiometric conditions.

Characterization of Filter Materials

The various filter materials made above were tested under long term oxidation conditions (500h, 800°C). Figure 2 shows that the samples with coatings containing excess silicon performed the best. They exhibited only a small change in weight, losing weight in the short term, and gaining slightly in the long term. This behavior is consistent with the fibers being coated by a dense, adherent silicon carbide coating.

Filter materials were also characterized in terms of their microwave absorption properties. Figure 3 shows the behavior of a typical sample that had been coated with CVD silicon carbide under "stoichiometric" conditions. The initial properties of the sample showed that it absorbed microwaves very strongly at ambient temperature. Its penetration depth (see below) was on the order of 1 cm. On heating the first time, the properties of the material changed dramatically. At about 600°C, the sample became much less absorptive and its penetration depth increased by a factor of 10, and then fell again as temperature was further increased. Upon a second heating, the sample behaved very differently. Its penetration depth at ambient temperature was about 1000 cm. This value decreased with increasing temperature and at 700°C matched the values obtained during the first heating. There were no additional changed in microwave properties with additional heatings (3,4, and 5).

The drastic changes in microwave absorption (penetration depth) during the first heating is consistent with burnout of

carbon in the sample. The semilog relationship of penetration depth with temperature during cycles 2 though 5 is consistent with the exponential increase in the electrical conductivity of silicon carbide with increasing temperature.

Penetration Depth and Applicator Design

Microwaves are absorbed in materials according to the Beer-Lambert Law:

$$P = P_o \exp(-\alpha X) \qquad (1)$$

where P is the power at any point, P_o is the incident power, α is the absorption coefficient, and X is the distance of penetration into the material. The absorption coefficient, α, is related to more fundamental properties:

$$\alpha = (\omega \sqrt{e'_r} \tan \delta) / c \qquad (2)$$

where ω = frequency, e'_r = relative dielectric constant, $\tan \delta$ = dielectric loss tangent, and c = speed of light. One may define a characteristic distance, called the penetration depth, which is related to the absorption coefficient. The penetration depth is defined as the distance into the material at which the incident energy has been reduced by a factor of 1/e (where e = 2.7183, the base of the natural logarithms). Figure 4 shows this relationship graphically.

The importance of penetration depth (absorption coefficient) as a design parameter is shown in Figure 5. This figure shows a simplified design for a microwave filter heater. For a material having a very large absorption coefficient (small penetration depth), $\alpha r >> 1$ and all of the microwave energy is deposited at the outer surface of the filter. For very small

absorption coefficients (large penetration depths), $\alpha r << 1$ and the microwave energy is absorbed very slowly by the filter material. Standing waves build up inside the applicator, which lead to "hot spots" and "cold spots" in the filter. For moderate absorption coefficients (moderate penetration depths), $\alpha r \approx 1$, most of the microwave energy is absorbed in one or two passes through the filter. This leads to the most uniform heating of the filter by the microwaves. The penetration depths of the materials being developed in this study range from 10 to 1000 cm for an individual layer of CVD coated filter material. The actual filters will contain multiple layers of filter material. This will produce a composite having a penetration depth that is of the order of the size of the microwave applicator, i.e., 10 to 20 cm.

System Testing

In February 1995, a prototype filter cartridge was tested at Cummins Engine Company in a developmental microwave applicator as a first proof-of-concept test for the microwave regenerated filter. The filter removed carbon particles from the exhaust of a test diesel engine and the microwave heater successfully regenerated the filter by burning out the carbon.

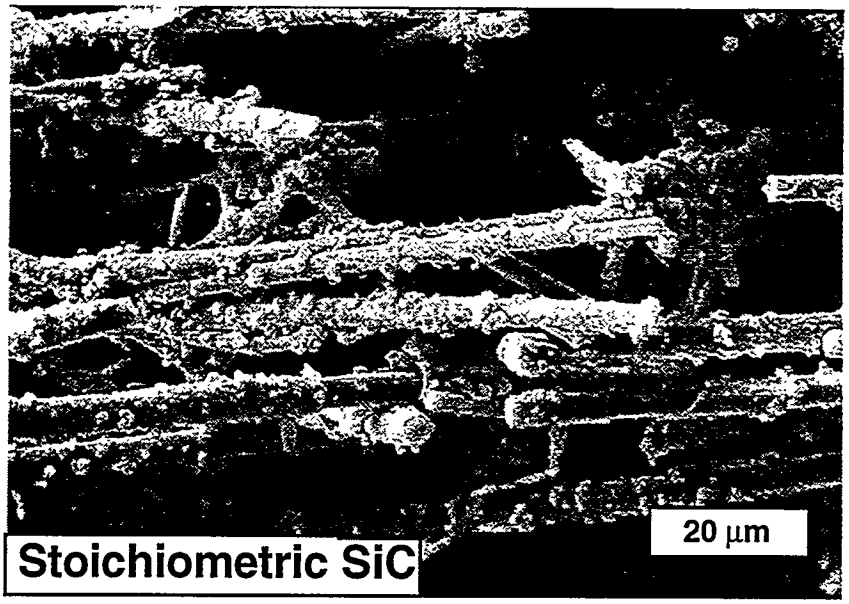

(a)

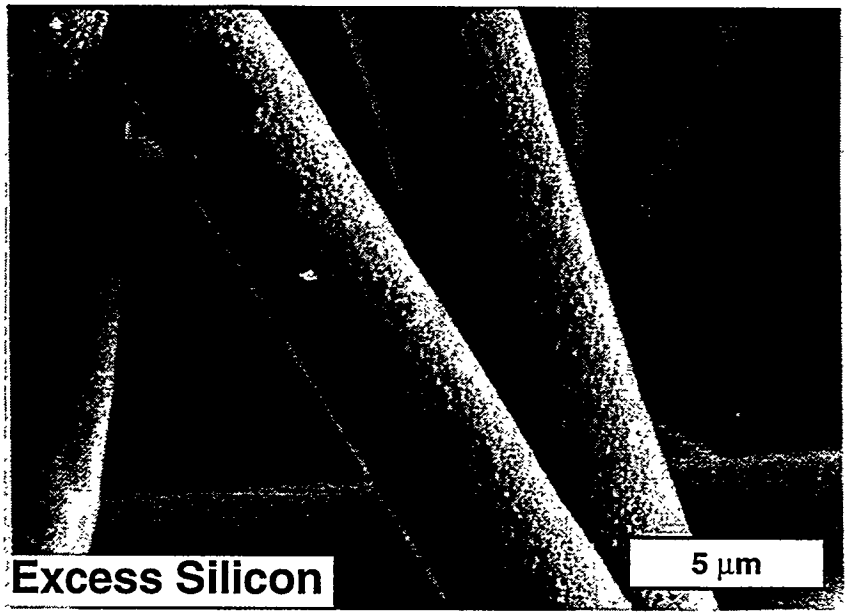

(b)

Figure 1. The addition of excess silicon to the CVI coating on the filter preforms produced a superior coating: (a) stoichiometric SiC; (b) excess silicon. SEM micrographs.

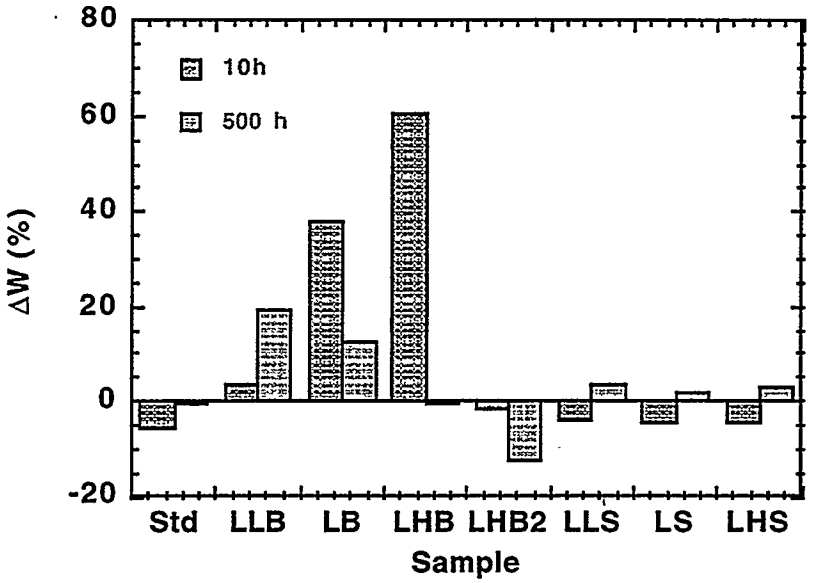

Figure 2. Samples containing excess silicon in the CVI coating were the most resistant to oxidation.

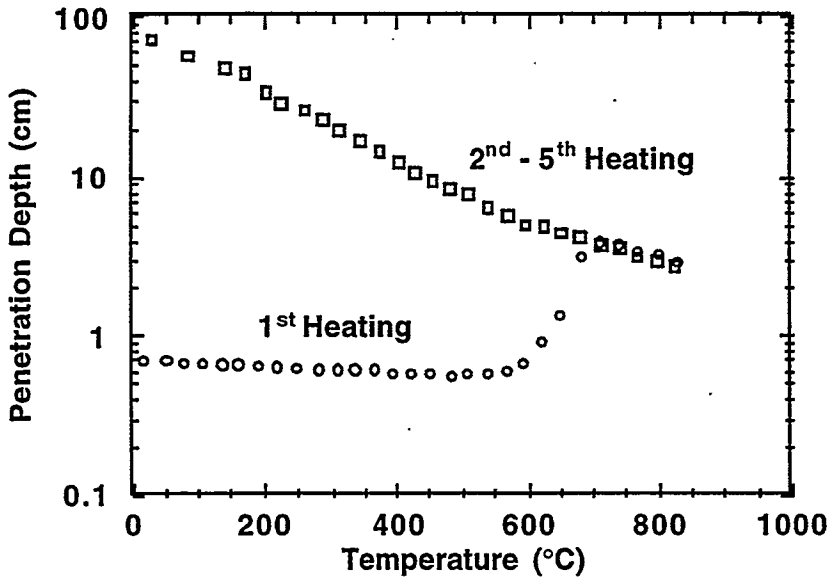

Figure 3. SiC coated alumina fiber filter materials "aged" on first heating. They were stable on subsequent heating. Filter coated with "stoichiometric" SiC CVI mixture.

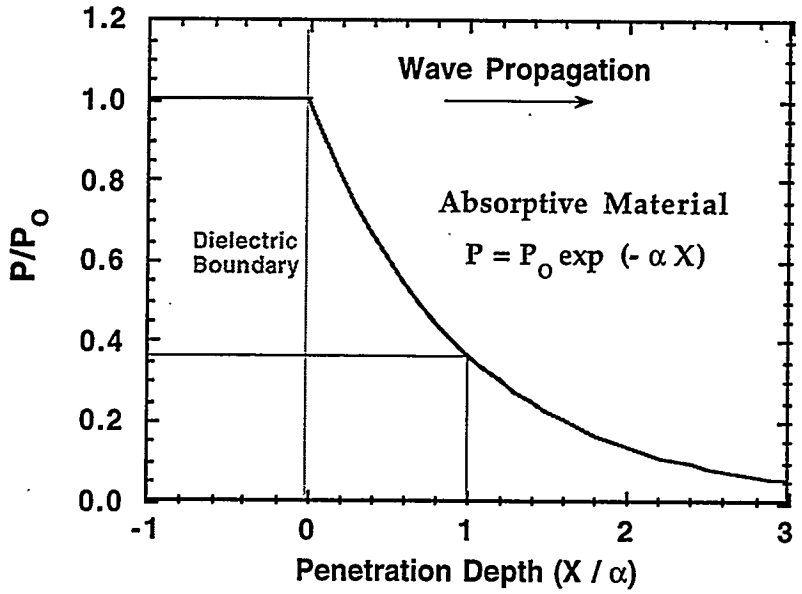

Figure 4. Most of the power in a microwave beam is lost in the first penetration depth.

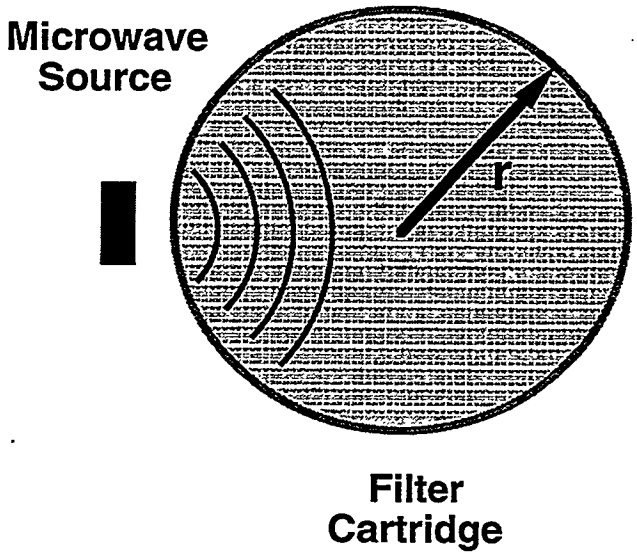

Figure 5. Penetration depth is an important factor in developing a microwave applicator the heats uniformly.

HIGH TEMPERATURE INORGANIC MEMBRANES FOR SEPARATING HYDROGEN

D. E. Fain and G. E. Roettger

Oak Ridge K-25 Site*
P. O. Box 2003
Oak Ridge, Tennessee 37831-7271

ABSTRACT

Effort has continued to accumulate data on the transport of gases over the temperature range from room temperature to 275°C with inorganic membranes having a range of pore radii from approximately 0.25 nm to 3 nm. An experimental alumina membrane having an estimated mean pore radius of 0.25 nm has been fabricated and tested. Extensive testing of this membrane indicated that the separation factor for helium and carbon tetrafluoride at 250°C was 59 and the extrapolated high temperature separation factor was 1,193. For safety reasons, earlier flow measurements concentrated on helium, carbon dioxide, and carbon tetrafluoride. New data have been acquired with hydrogen to verify the agreement with the other gases. During the measurements with hydrogen, it was noted that a considerable amount of moisture was present in the test gas. The source of this moisture and its effect on permeance was examined. Improvements were implemented to the flow test system to minimize the water content of the hydrogen test gas, and subsequent flow measurements have shown excellent results with hydrogen. The extrapolation of separation factors as a function of temperature continues to show promise as a means of using the hard sphere model to determine the pore size of membranes. The temperature dependence of helium transport through membranes appears to be considerably greater than other gases for the smallest pore sizes. The effort to extend temperature dependence to the hard sphere model continues to be delayed, primarily because of a lack of adequate adsorption data.

INTRODUCTION

The goal of this project is to develop methods for fabricating ceramic membranes that will separate hydrogen efficiently from gasified coal at temperatures of 1,000°F or higher. To be economically useful, the membranes must have a high separation factor. Very high separation factors can be achieved with ceramic membranes if the pores are small enough to separate gas molecules by molecular sieving. A molecular sieve membrane ideally would have pores that are slightly smaller than the larger gas molecule but larger than the smaller gas molecule. Such a membrane permits only the

---

*The Oak Ridge K-5 Site is managed by Martin Marietta Energy Systems, Inc. For the U.S. Department of Energy under contract No. DE-AC05-84OR21400.

smaller gas molecule (such as hydrogen) to pass through the pores, as shown conceptually in Fig. 1, providing an infinite separation factor. Actual membranes always have a distribution of pore sizes with some pores considerably larger than ideal; hence, there is some limit on the separation factor actually achievable. The hard sphere diffusion model, discussed earlier, shows how the separation factor changes from square root of molecular weight ratio for Knudsen flow to infinite for a molecular sieve as the pore radius decreases.[1] Membranes having a tubular geometry, such as those being fabricated for this project, could be assembled into a useful separation module of the tube and shell type. A simplified module containing a single membrane tube is shown conceptually in Fig. 2. A single stage of membrane separation, using molecular sieve membranes having a high separation factor, could be adequate for many gas separation applications.

The primary objective of this project during the past year has been to develop and demonstrate through testing a ceramic membrane having sufficiently small pores to achieve a separation factor of 50 or higher. Another important objective was to upgrade the high temperature flow test system to permit hydrogen to be used as an additional test gas for measuring the permeance and separation factors of membranes. Key results and data pertaining to these objectives are summarized below.

DISCUSSION OF CURRENT ACTIVITIES

Alumina Membrane Having 0.25 nm Mean Pore Radius

An experimental alumina membrane has been produced and tested that has an estimated mean pore radius of about 0.25 nm (2.5Å). The membrane was tested in our high temperature flow test system using helium and carbon tetrafluoride as test gases. Flow measurements were made on the membrane over a range of pressures at room temperature, 100°C, and 250°C. Since the pore size of this membrane was considerably smaller than any previously available, the membrane was extensively tested to verify separation factors and to study the transport properties. Separation factors calculated from the ratios of specific flows were determined for the He/CF_4 gas pair. Repeat cycles of testing resulted in twelve separation factors being determined. One of these values proved to be a statistical outlayer and was omitted. A total of four He/CF_4 separation factors were determined at 250°C and their mean value was 59, which met the separation factor target of 50. An Arrhenius-type plot (ln separation factor plotted against the reciprocal of the absolute temperature) for the eleven separation

ORNL-DWG 95M-5199

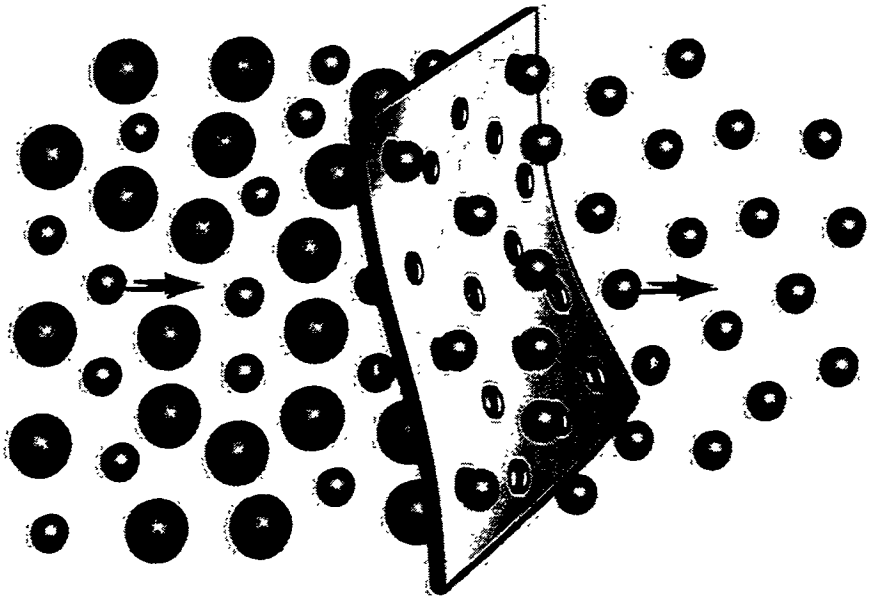

Fig. 1. Molecular sieve membrane for separating gas molecules.

ORNL-DWG 95M-5211

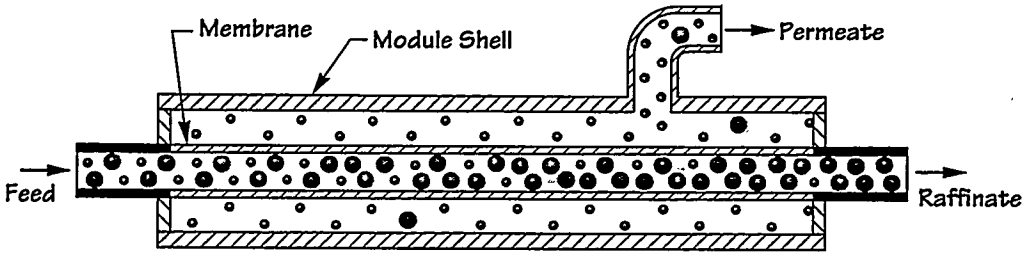

Fig. 2. Separation module using molecular sieve membrane to separate gases.

factors is shown in Fig. 3. A least squares fit of the data is extrapolated to a zero value of 1/T (infinite temperature) to estimate the separation factor at the high temperature limit where pure diffusive flow should exist. The high temperature extrapolated separation factor determined for the membrane was 1,193. This high temperature separation factor can be interpreted by the hard sphere model to provide an estimate of the membrane pore size. This calculation indicates that a mean pore radius of 0.25 nm is required to provide a He/CF_4 separation factor of 1,193 at the high temperature limit. Using the least squares fit of the data, a separation factor of 336 is calculated for 1,000°C and 164 is calculated for 1,000°F.

A typical example of the flow data measured on this membrane with carbon tetrafluoride at room temperature, 100°C, and 250°C is shown in Fig. 4. The flow data are plotted as a permeance (sccm/sq cm/cm Hg) versus average pressure (average of the forepressure and backpressure). The CF_4 permeance is highest at room temperature and declines as the temperature is increased to 250°C. This trend toward lower permeance at higher temperature has been observed with other small pore size membranes and appears to result from decreasing surface flow of adsorbed molecules as temperature is increased.

A typical example of the helium flow data measured on the membrane at the same three temperatures is shown in Fig. 5. The measurements show much higher helium permeance at 250°C than at the lower temperatures. This phenomenon, which was observed in several repeat cycles of testing of the membrane, has not been observed with previous membranes and is not yet understood.

The permeance data shown in Figs. 4 and 5 may be converted to transport probabilities and extrapolated to zero pressure, as described earlier, to provide a zero pressure transport probability for each gas at each temperature.[1] For free molecule or Knudsen flow, the zero pressure transport probability should be a function of the properties of the membrane and independent of the type of gas molecule and temperature. The zero pressure transport probabilities determined for He and CF_4 at the three temperatures are shown in Fig. 6. The trends noted earlier in permeance values with temperature are very prominent in the plotted transport probabilities and indicate large deviations of the actual gas transport from free molecule or Knudsen flow.

High Temperature Flow Test System Upgraded to Use Hydrogen

The high temperature flow test system is used routinely to evaluate the separation factors of membranes using inert gases such as helium and carbon tetrafluoride as discussed above. Since

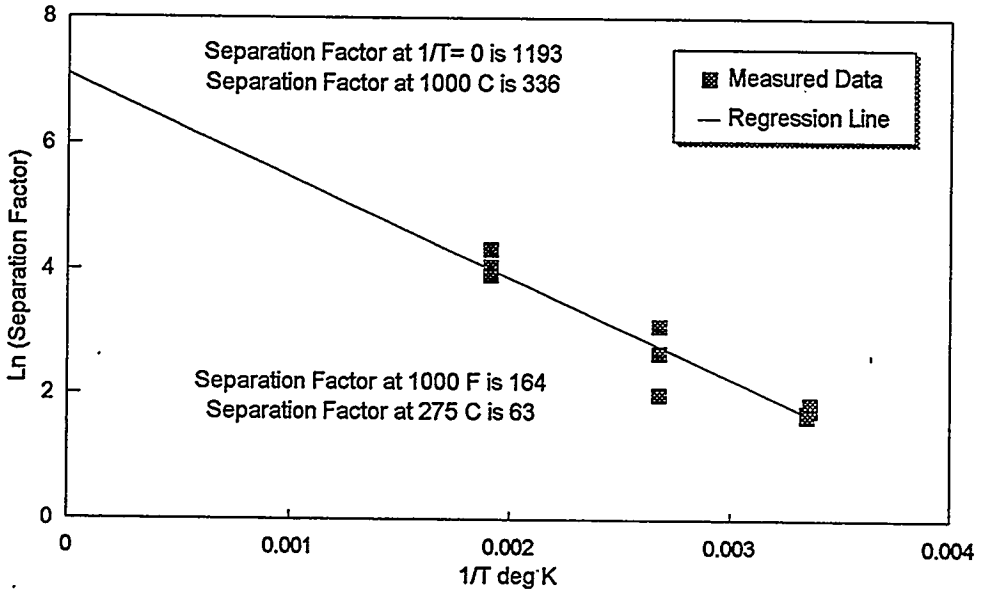

Fig. 3. He/CF_4 separation factors measured on alumina membrane having mean pore radius of 0.25 nm.

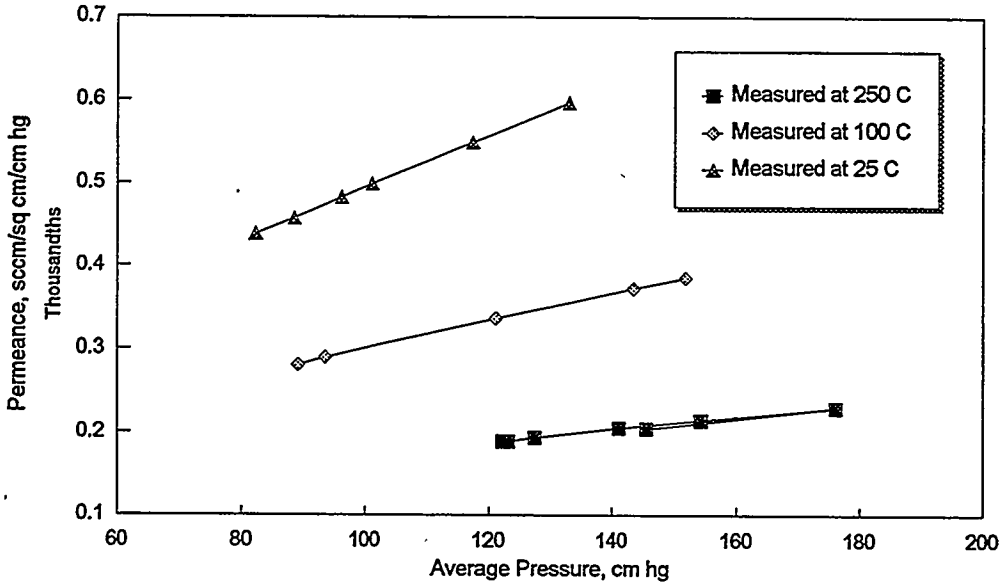

Fig. 4. Carbon tetrafluoride flow data measured at three temperatures through alumina membrane having mean pore radius of 0.25 nm.

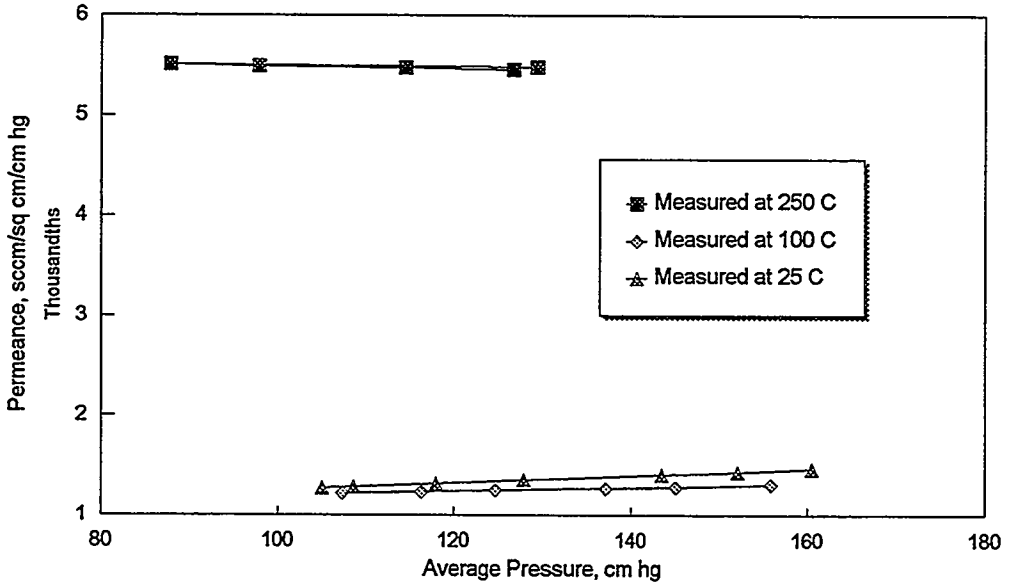

Fig. 5. Helium flow data measured at three temperatures through alumina membrane having mean pore radius of 0.25 nm.

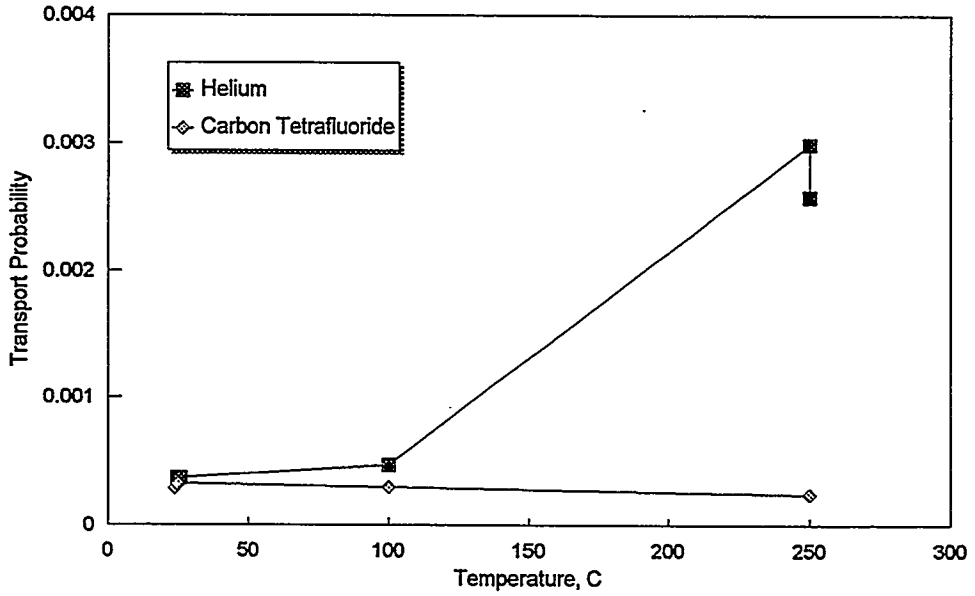

Fig. 6. Zero pressure transport probability measured at three temperatures on alumina membrane having mean pore radius of 0.25 nm.

hydrogen separation is a primary goal of this task, the test system has been upgraded to permit hydrogen to be used as an additional test gas. Several modifications of equipment and procedures were made to assure safe operation with hydrogen at elevated temperatures.

During initial operations with hydrogen in the test system, it was found that the hydrogen test gas contained a high concentration of moisture. A moisture analyzer (with sensor designed for use in hydrogen) was used to analyze the test gas. Analyses showed that the water content of the hydrogen exiting the test system was greater than 1,000 ppm, and the water content of the research grade hydrogen fed to the system was about 85 ppm. These surprisingly high water contents were of concern because water in the test gas can adsorb on the walls of the small pores and affect the flow data, and the magnitude of such effects would differ with temperature.

Several improvements were made to the test system to minimize the water content of the hydrogen. These improvements included the replacement of some copper tubing in the system with stainless steel since hydrogen can react with copper oxide to produce water vapor, particularly at elevated temperatures. In addition, a molecular sieve dryer was installed in the feed gas stream to dry the hydrogen entering the test system. Other minor modifications were made to minimize opportunities for ambient moisture to enter the system. These improvements reduced the water content of the hydrogen test gas by nearly two orders of magnitude. For example, moisture analyses indicated that the water content of hydrogen entering the test system was being limited to a satisfactory level of approximately 1 ppm. Subsequent flow measurements made over a range of temperatures have shown excellent results with hydrogen. Hydrogen flow data measured on a recent membrane are discussed below and compared to helium flow data.

Hydrogen Flow Data on 0.75 nm Mean Pore Radius Membrane

An alumina membrane, having a mean pore radius of 0.75 nm, was tested recently in the high temperature flow test system at several temperatures up to 275 °C using helium, carbon tetrafluoride, and hydrogen as test gases. These data were the first measured with hydrogen after implementing several improvements (described above) to minimize the water content of the hydrogen test gas. From the flow data, separation factors were determined for He/CF_4 and for H_2/CF_4 at each of the

temperatures and are plotted in Fig. 7. The separation factors for H_2/CF_4 were higher than values for He/CF_4 at each of the five temperatures. The extrapolated high temperature separation factor for H_2/CF_4 was 10.5 compared to 8.3 for He/CF_4. The hard sphere model was used to calculate the membrane pore size from these high temperature separation factors. The membrane mean pore radius calculated from the H_2/CF_4 data was 0.75 nm, and the value calculated from the He/CF_4 data was 0.74 nm. The excellent agreement of these results supports the hard sphere diffusion model and indicates that the hydrogen flow data are of high quality. Similar measurements with hydrogen will be made using membranes having smaller pores.

Separation factors for He/CF_4 and for H_2/CF_4 at the high temperature limit can be calculated from the hard sphere model. These model calculations are plotted in Fig. 8 as a function of the membrane pore size. The calculations indicate that the H_2/CF_4 separation factors should be moderately higher than the He/CF_4 separation factors for pore radii down to about 0.3 nm. For pore radii of 0.3 nm and smaller, the He/CF_4 separation factors should be higher.

REFERENCES

1. D. E. Fain and G. E. Roettger, "Hydrogen Production Using Inorganic Membranes" in Proceedings of the Eighth Annual Conference on Fossil Energy Materials, Oak Ridge, Tennessee, May 10-12, 1994, p. 51-61.

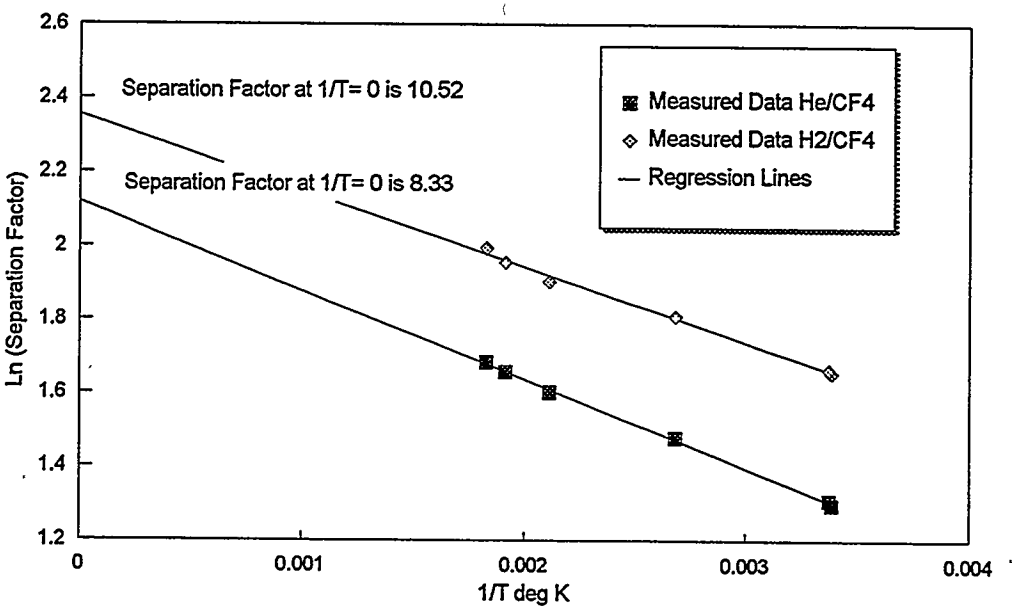

Fig. 7. Separation factors for He/CF_4 and H_2/CF_4 measured on alumina membrane having mean pore radius of 7.5Å.

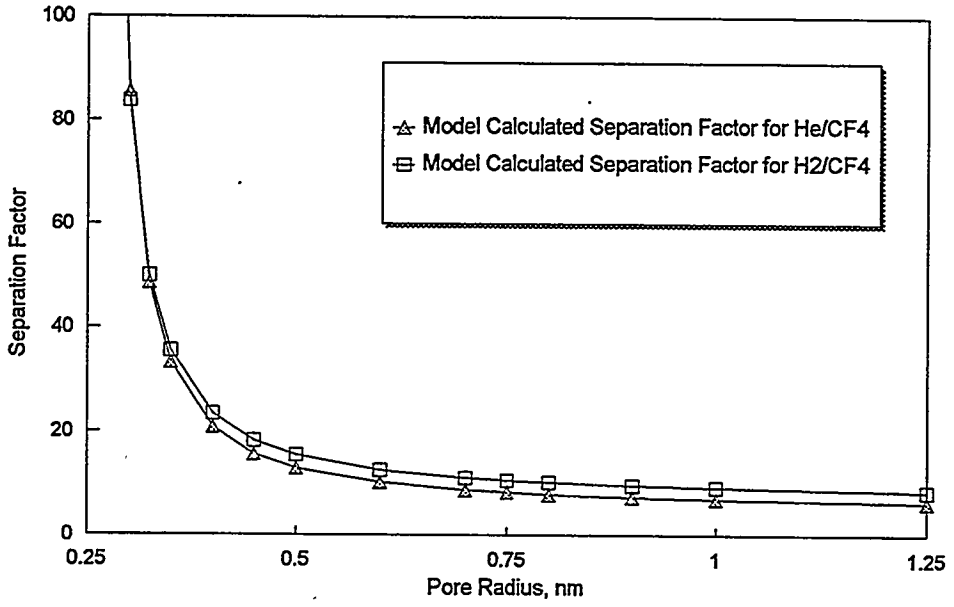

Fig. 8. Separation factors calculated from transport model for He/CF_4 and H_2/CF_4 at high temperature limit.

MIXED OXYGEN ION/ELECTRON-CONDUCTING CERAMICS FOR OXYGEN SEPARATION

J.W. Stevenson, B.L. Armstrong, T.R. Armstrong,
J.L. Bates, L.R. Pederson, and W.J. Weber

Pacific Northwest Laboratory†
P.O. Box 999
Richland, WA 99352

ABSTRACT

Solid mixed-conducting electrolytes in the series $La_{1-x}A_xCo_{1-y}Fe_yO_{3-\delta}$ (A=Sr,Ca,Ba) are potentially useful as passive membranes to separate high purity oxygen from air and as cathodes in fuel cells. All of the compositions studied exhibited very high electrical conductivities. At lower temperatures, conductivities increased with increasing temperature, characterized by activation energies of 0.05 to 0.16 eV that are consistent with a small polaron (localized electronic carrier) conduction mechanism. At higher temperatures, electronic conductivities tended to decrease with increasing temperature, which is attributed to decreased electronic carrier populations associated with lattice oxygen loss. Oxygen ion conductivities were higher than that of yttria stabilized zirconia and increased with the cobalt content and also increased with the extent of divalent A-site substitution. Thermogravimetric studies were conducted to establish the extent of oxygen vacancy formation as a function of temperature, oxygen partial pressure, and composition. These vacancy populations strongly depend on the extent of A-site substitution. Passive oxygen permeation rates were established for each of the compositions as a function of temperature and oxygen partial pressure gradient. For 2.5 mm thick membranes in an oxygen vs nitrogen partial pressure gradient, oxygen fluxes at 900°C ranged from approximately 0.3 sccm/cm^2 for compositions high in iron and with low amounts of strontium A-site substitution to approximately 0.8 sccm/cm^2 for compositions high in cobalt and strontium. A-site substitution with calcium instead of strontium resulted in substantially lower fluxes.

INTRODUCTION

Perovskite compositions in the $(La,Sr)(Co,Fe)O_{3-\delta}$ system have been studied as candidate materials for applications such as solid oxide fuel cell cathodes, oxygen separation membranes, and membrane reactors.[1-10] At elevated temperatures, these compositions exhibit substantial mixed (anionic and electronic) conductivity. The oxygen

† Operated by Battelle Memorial Institute for the US Department of Energy under contract DE-AC06-76RLO 1830

anion conductivity in these materials can be quite large relative to other oxygen conductors, such as yttria-stabilized zirconia (YSZ). The mixed conducting behavior results in a spontaneous flux of oxygen through dense sintered materials in an oxygen partial pressure ($P(O_2)$) gradient. Under these conditions, gaseous oxygen on the high $P(O_2)$ side of the material is reduced to anionic oxygen at the surface, transported ionically through the material to the low $P(O_2)$ side, and re-oxidized to O_2. The ionic current due to the flux of oxygen ions is offset internally by an electronic current, eliminating the need for electrodes and external circuitry.

Teraoka et al[1-3] investigated several $(La,Sr)(Co,Fe)O_{3-\delta}$ compositions using oxygen permeation and four-probe dc techniques. At 800°C, ionic conductivities were on the order of 0.01-1 S/cm, while electronic conductivities exceeded 100 S/cm. The ionic conductivity increased sharply with increasing Sr content and decreased slightly with increasing Fe content. The increasing ionic conductivity with increasing Sr content was attributed to an increase in the oxygen vacancy concentration as trivalent La cations were replaced by divalent (acceptor) Sr cations. While compositions highest in Sr and Co tend to offer the highest oxygen fluxes, other factors must also be considered. For example, $SrCo_{0.8}Fe_{0.2}O_{3-\delta}$ provides very high oxygen permeability but exhibits very limited chemical and structural stability in reduced $P(O_2)$ environments.[4] Kruidhof et al[7] observed that, at lower temperatures (e.g., 750°C), the oxygen flux through several compositions high in Sr and/or Co (e.g., $La_{0.6}Sr_{0.4}CoO_{3-\delta}$ and $SrCo_{0.8}Fe_{0.2}O_{3-\delta}$) decreased substantially with time. This degradation in behavior was attributed to an order-disorder transition which caused the oxygen vacancies to become immobile below a composition-dependent transition temperature. The purpose of the present study is to increase the understanding of the synthesis and electrochemical properties of materials within the $La_{1-x}(Sr,Ca,Ba)_xCo_{1-y}Fe_yO_{3-\delta}$ system, in order to assist their successful utilization in electrode and oxygen membrane applications.

DISCUSSION OF CURRENT ACTIVITIES

A simple code is used to refer to the compositions under study. Compositions in the system $La_{1-x}Sr_xCo_{1-y}Fe_yO_{3-\delta}$ are designated by LSCF followed by numerals indicating the relative proportions of each cation. For example, $La_{0.6}Sr_{0.4}Co_{.2}Fe_{0.8}O_{3-\delta}$

is designated LSCF-6428, $La_{0.2}Sr_{0.8}Co_{.8}Fe_{0.2}O_{3-\delta}$ is designated LSCF-2882. $La_{1-x}Ba_xCo_{1-y}Fe_yO_{3-\delta}$ compositions and $La_{1-x}Ca_xCo_{1-y}Fe_yO_{3-\delta}$ compositions are designated by LBCF and LCCF, respectively. The required compositions were prepared using the glycine-nitrate combustion synthesis technique.[11] The LSCF compositions were essentially single phase perovskites after calcination at 850°C, while the LCCF and LBCF compositions tended to require higher temperature treatment before yielding a high proportion (>95 wt.%) of the desired perovskite phase.

Thermogravimetric analysis was performed on calcined powder specimens using a heating rate of 5°C/min and a cooling rate of 2°C/min. The TGA measurements were performed in several different atmospheres (air; 10,000 ppm O_2 in Ar; 1,000 ppm O_2 in Ar; 100 ppm O_2 in Ar). TGA results for the LSCF compositions when heated and cooled in air are shown in Figure 1. Substantial reversible weight loss was observed at elevated temperatures. This weight loss was due to a partial loss of lattice oxygen, so that the oxygen deficiency, δ, increased with increasing temperature. The temperature at which oxygen loss began to occur decreased as the Sr content increased. The magnitude of the oxygen loss increased with increasing Sr content. This behavior is consistent with previously reported results for two of these compositions (LSCF-6428,4628).[5] The effect of ambient $P(O_2)$ on weight loss behavior was examined by performing TGA measurements in various atmospheres. The magnitude of the oxygen loss upon heating increased only slightly as the ambient $P(O_2)$ was reduced. In 10,000 ppm O_2, full re-oxidation was observed in high Co materials upon cooling (as in air), but re-oxidation did not occur in atmospheres of 1,000 and 100 ppm O_2 (Figure 2). Compositions containing less cobalt did not experience full re-oxidation in the 10,000 ppm O_2 environment. For a given Sr content (e.g., $x = 0.6, 0.8$), the degree of re-oxidation during cooling in the 10,000 ppm O_2 atmosphere decreased with increasing substitution of Fe for Co.

The ionic transport number in these compositions is less than 1%, so that bulk electrical conductivities obtained by 4-probe pulsed dc measurements on sintered specimens provided a measure of the electronic conductivities of the materials. Typical sintering temperatures were 1150-1250°C with dwell times of 2-4 hours. Plots of log σT vs. 1000/T (σ is conductivity (in S/cm) and T is absolute temperature) for the LSCF compositions are shown in Figure 3. At lower temperatures, conductivities increased

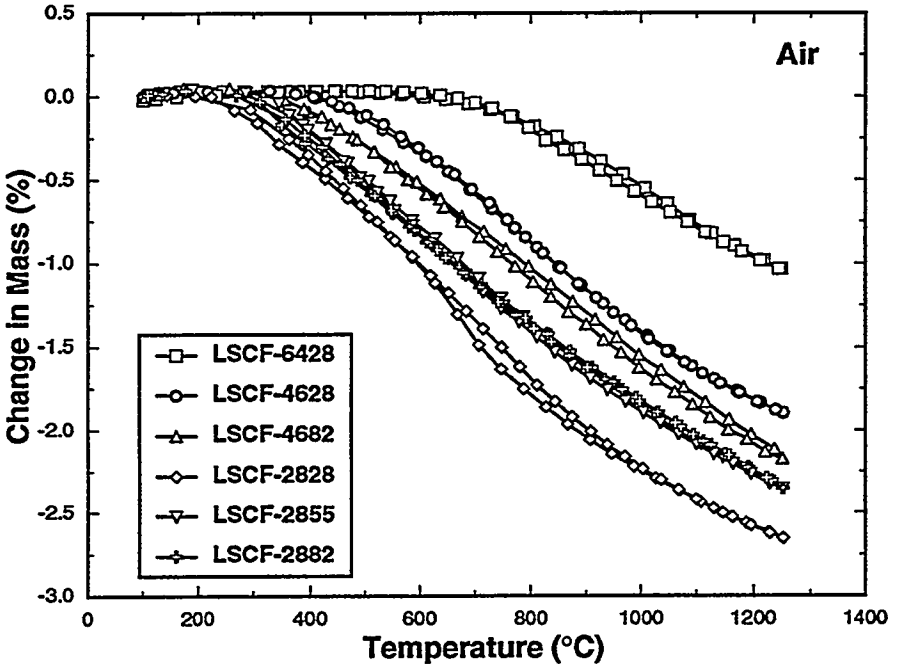

Fig. 1. Thermogravimetric measurements on LSCF compositions in air.

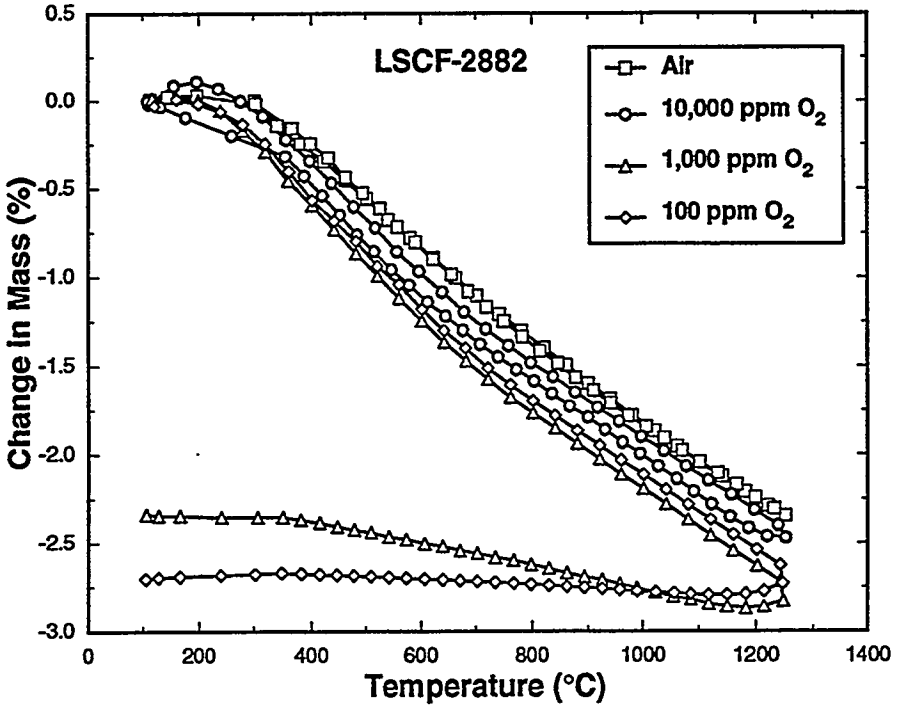

Fig. 2. Thermogravimetric measurements on LSCF-2882 in various atmospheres.

linearly with increasing temperature, with activation energies on the order of 0.05-0.16 eV. This behavior is consistent with a small polaron conduction mechanism (i.e., localized electronic carriers with a thermally activated mobility).[12] At higher temperatures, conductivity was observed to decrease substantially with increasing temperature. This exaggerated decrease at high temperatures is attributed to a decreasing concentration of electronic charge carriers (electron holes, $h^{\bullet}$) as the oxygen content of the material decreases. This process can be represented (Kroger-Vink notation)[13] as:

$$2h^{\bullet} + O_O^{x} \Rightarrow V_O^{\bullet\bullet} + \tfrac{1}{2}O_2 \qquad [1]$$

Thus, two electron holes are eliminated for each oxygen ion leaving the lattice. While this decrease in oxygen stoichiometry with increasing temperature reduces the electronic carrier concentration, it simultaneously increases the concentration of the ionic charge carriers (oxygen vacancies). Plots of σT vs. 1000/T for the LCCF compositions tended to remain relatively linear at temperatures where the LSCF composition exhibited the pronounced decline in conductivity, suggesting that the electronic carrier concentrations in these materials remain essentially constant over a wider temperature range than is the case for the LSCF materials.

Passive oxygen permeation was measured using sintered disc specimens sealed in an alumina test cell with gold gaskets. Air and oxygen were used as source gases with nitrogen as the carrier gas. Oxygen flux was measured as a function of temperature using heating and cooling rates of 0.65°C/min and gas flow rates of 25-30 sccm. Temperature-dependent oxygen permeation rates (in oxygen vs. nitrogen) through sintered specimens of several LSCF, LBCF and LCCF compositions (2.3 - 3.1 mm thick) are shown in Figure 4. For the LSCF compositions, increased Sr content resulted in a substantial increase in flux. This was consistent with the TGA results which showed that the degree of oxygen deficiency increased with increasing Sr content. The increase in oxygen flux with increasing temperature can thus be attributed to two factors: increasing mobility of the lattice oxygen ions, and increasing concentration of lattice oxygen vacancies. Fluxes for the LCCF compositions were significantly lower than for the LSCF compositions.

Ionic conductivities were calculated from the flux rates using the relation:[14]

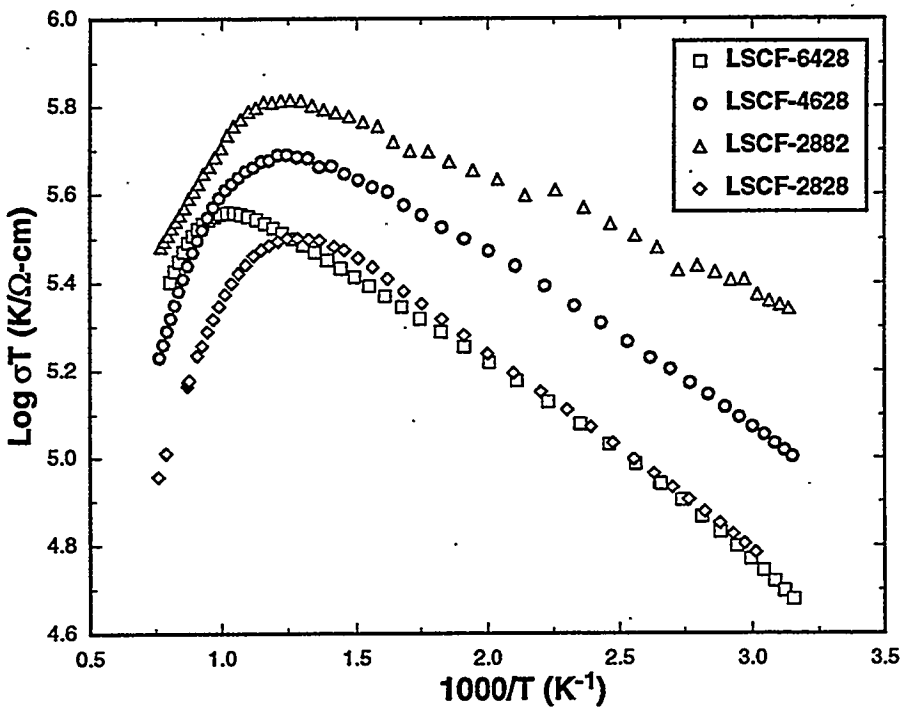

Fig. 3. 4-probe dc conductivity data for the indicated LSCF compositions.

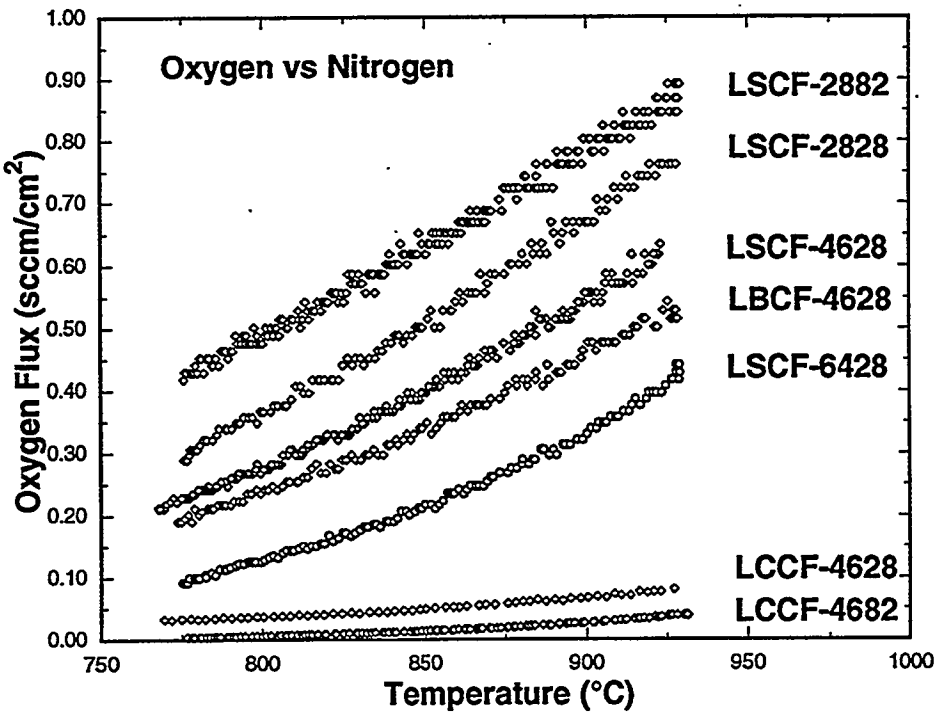

Fig. 4. Oxygen permeation as a function of temperature for the indicated compositions.

$$\sigma_i = \frac{4 F J t}{R T \ln\left[P(O_2^I)/P(O_2^{II})\right]} \qquad [2]$$

where F is Faraday's constant, J is flux (in A/cm2), t is specimen thickness, R is the gas constant, T is absolute temperature, and $P(O_2^I)$ and $P(O_2^{II})$ are the oxygen partial pressures on each side of the specimen. The calculated ionic conductivities at 900°C are shown in Table I. The LSCF compositions exhibited significantly higher conductivities than YSZ (also shown in Table I). These values are similar to conductivities obtained with a 4-probe dc technique by Teraoka et al.[2] Ionic transport numbers were calculated by dividing the ionic conductivity by the total conductivity.

Table I. Ionic and Electronic Conductivities at 900°C

Composition	Ionic Conductivity (S/cm)	Electronic Conductivity (S/cm)	Ionic Transport Number
LSCF-6428	0.23	252	9.1×10^{-4}
LSCF-4628	0.40	219	1.8×10^{-3}
LSCF-2828	0.62	120	5.2×10^{-3}
LSCF-2882	0.87	310	2.8×10^{-3}
LCCF-4628	0.03	52	5.8×10^{-4}
LCCF-4682	0.01	296	3.4×10^{-5}
YSZ	0.10	--	1

Aging effects on oxygen flux behavior are being studied through long term permeation measurements. Kruidhof et al[7] reported that, for some compositions in the LSCF system, substantial degradation of flux occurred at temperatures below a composition-dependent order-disorder transition temperature as the oxygen vacancies within the structure became ordered and, therefore, immobile. Figure 5 shows their data

for $La_{0.6}Sr_{0.4}CoO_{3-\delta}$ at 750°C. In the present study, flux through a different LSCF composition (LSCF-2882) was measured at 775°C (Figure 5). Only a slight decrease (approx. 4%) in flux was observed after operation for 340 hours. This behavior indicates that LSCF compositions remain viable candidate materials for oxygen permeation applications at intermediate temperatures (e.g., 750-800°C).

The removal of lattice oxygen from the perovskite structure results in a volumetric expansion in the material. This phenonenon is being investigated using controlled atmosphere dilatometry on sintered bars to measure linear expansion as a function of ambient $P(O_2)$. Results for LSCF-6428 at three temperatures are shown in Figure 6. It is apparent that even mildly reducing conditions altered the oxygen stoichiometry sufficiently to cause significant linear expansion. The magnitude of the expansion was similar to that observed in lanthanum chromite materials, but the expansion occurred in much higher oxygen partial pressures due to the lower enthalpy of oxygen vacancy formation in cobaltite-ferrite perovskites.

Ease of fabrication is an important factor in the successful utilization of these materials; a tubular geometry is desirable for oxygen separation applications. Open end tubes have been fabricated from LSCF-6428 powders using rubber bag tooling and 22 ksi cold isostatic pressure. Sintered densities (after heat treatment at 1250°C for 4 hours in air) were 95% of theoretical. Final inner and outer diameters were approximately 0.28 and 0.40", respectively.

REFERENCES

1. Y. Teraoka, H. Zhang, S. Furukawa, and N. Yamazoe, "Oxygen Permeation through Perovskite-Type Oxides," Chemistry Letters, 1743-1746 (1985).

2. Y. Teraoka, H. Zhang, K. Okamoto, and N. Yamazoe, "Mixed Ionic-Electronic Conductivity of $La_{1-x}Sr_xCo_{1-y}Fe_yO_{3-\delta}$ Perovskite-Type Oxides," Mat. Res. Bull., **23**, 51-58 (1988).

3. Y. Teraoka, T. Nobunaga, K. Okamoto, N. Miura, and N. Yamazoe, "Influence of Constituent Metal Cations in Substituted $LaCoO_3$ on Mixed Conductivity and Oxygen Permeability," Solid State Ionics, **48**, 207-212 (1991).

4. U. Balachandran, S. Morissette, J. Picciolo, J. Dusek, and R. Peoppel,"Fabrication of Ceramic Membrane Tubes for Direct Conversion of Natural Gas," Proc. International Gas Research Conference, Ed. H. Thompson, Government Institutes, Rockville, MD, pp. 565-573 (1992).

5. L. Tai, M. Nasrallah, and H. Anderson, "$(La_{1-x}Sr_x)(Co_{1-y}Fe_y)O_3$, A Potential Cathode for Intermediate Temperature SOFC Applications," Proc. 3rd Int. Symp. on SOFC, Electrochem. Soc., Vol. 93-4, 241-251 (1993).

6. H. Anderson, C. Chen, L. Tai, and M. Nasrallah, "Electrical Conductivity and Defect Structure of (La,Sr)(Co,Fe)O_3," Proc. 2nd Int. Symp on Ionic and Mixed Conducting Ceramics, Ed. T. Ramanarayanan, W. Worrell, and H. Tuller, Electrochem. Soc., Vol. 94-12, 376-387 (1994).

7. H. Kruidhof, H. Bouwmeester, R. v. Doorn, and A. Burggraaf, "Influence of Order-Disorder Transitions on Oxygen Permeability through Selected Nonstoichiometric Perovskite-Type Oxides," Solid State Ionics, **63-65**, 816-822 (1993).

8. H. Bouwmeester, H. Kruidhof, and A. Burggraaf, "Importance of the Surface Exchange Kinetics as Rate Limiting Step in Oxygen Permeation through Mixed-Conducting Oxides," Solid State Ionics, **72**, 185-194 (1994).

9. U. Balachandran, J. Dusek, S. Sweeney, R. Peoppel, R. Mieville, P. Maiya, M. Kleefisch, S. Pei, T. Kobylinski, C. Udovich, and A. Bose,"Methane to Syngas via Ceramic Membranes," Am. Cer. Soc. Bulletin, **74**, 71-75 (1995).

10. C.C. Chen, M.M. Nasrallah, H.U. Anderson, and M.A. Alim, "Immittance Response of $La_{0.6}Sr_{0.4}Co_{0.2}Fe_{0.8}O_3$," J. Electrochem. Soc., **142**, 491-496 (1995).

11. L.A. Chick, L.R. Pederson, G.D. Maupin, J.L. Bates, L.E. Thomas, and G.J. Exarhos, "Glycine-Nitrate Combustion Synthesis of Oxide Ceramic Powders," Materials Letters, **10**, 6-12 (1990).

12. D. P. Karim and A.T. Aldred, "Localized Level Hopping Transport in La(Sr)CrO_3," Phys. Rev. B, **20**, 2255-2263 (1979).

13. F.A. Kroger, The Chemistry of Imperfect Crystals, North-Holland, Amsterdam (1964).

14. M. Liu and A. Joshi, "Characterization of Mixed Ionic-Electronic Conductors," Proc. First Int. Symp. Ionic and Mixed Conducting Ceramics, Eds. T.A. Ramanarayanan and H.L. Tuller, Electrochem. Soc, Proc. Vol. 91-12, 231-246 (1991).

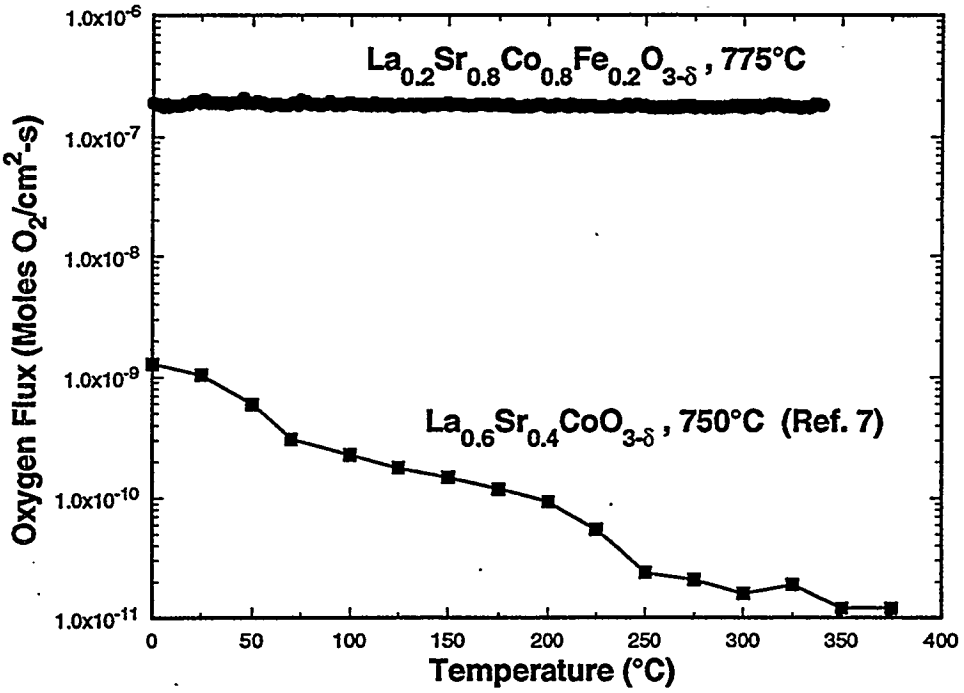

Fig. 5. Oxygen permeation as a function of time for the indicated compositions.

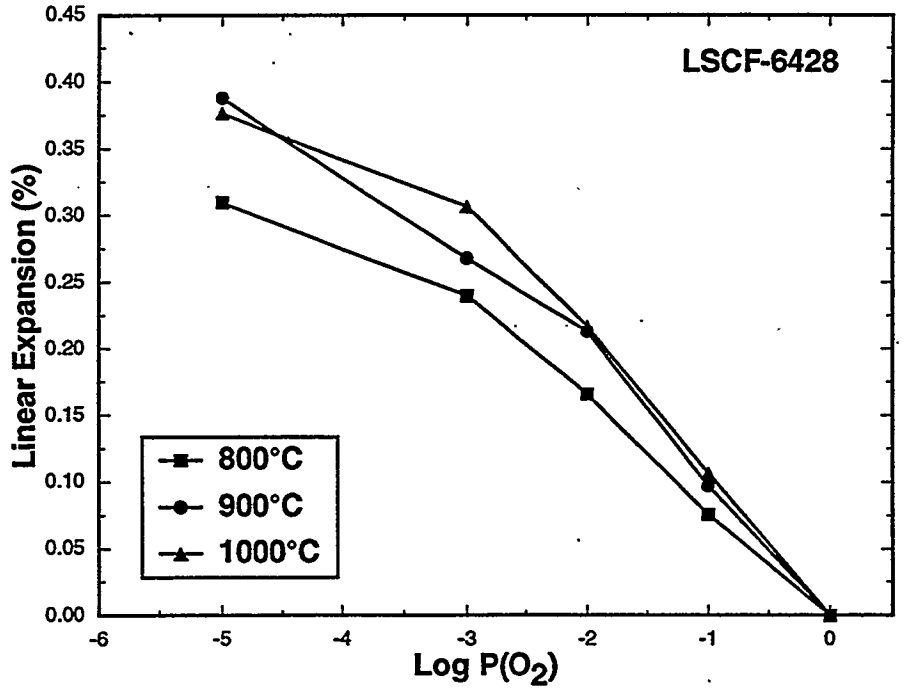

Fig. 6. Linear expansion of LSCF-6428 as a function of ambient $P(O_2)$.